DISSERTATION

DEVICE PHYSICS OF $Cu(In,Ga)Se_2$ THIN-FILM SOLAR CELLS

Submitted by

Markus Gloeckler

Department of Physics

In partial fulfillment of the requirements

For the Degree of Doctor of Philosophy

Colorado State University

Fort Collins, Colorado

Summer 2005

Reproduced with permission of the copyright owner. Further reproduction prohibited without permission.

UMI Number: 3185505

INFORMATION TO USERS

The quality of this reproduction is dependent upon the quality of the copy submitted. Broken or indistinct print, colored or poor quality illustrations and photographs, print bleed-through, substandard margins, and improper alignment can adversely affect reproduction.

In the unlikely event that the author did not send a complete manuscript and there are missing pages, these will be noted. Also, if unauthorized copyright material had to be removed, a note will indicate the deletion.

UMI®

UMI Microform 3185505

Copyright 2005 by ProQuest Information and Learning Company.

All rights reserved. This microform edition is protected against unauthorized copying under Title 17, United States Code.

ProQuest Information and Learning Company
300 North Zeeb Road
P.O. Box 1346
Ann Arbor, MI 48106-1346

Reproduced with permission of the copyright owner. Further reproduction prohibited without permission.

COLORADO STATE UNIVERSITY

June 1, 2005

WE HEREBY RECOMMEND THAT THE DISSERTATION PREPARED UNDER OUR SUPERVISION BY MARKUS GLOECKLER ENTITLED DEVICE PHYSICS OF $Cu(In,Ga)Se_2$ THIN-FILM SOLAR CELLS BE ACCEPTED AS FULFILLING IN PART REQUIREMENTS FOR THE DEGREE OF DOCTOR OF PHILOSOPHY.

Committee on Graduate Work

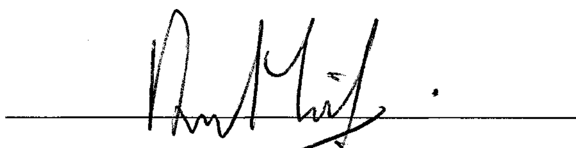

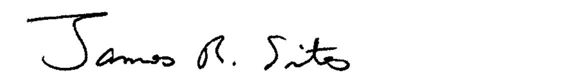

Adviser

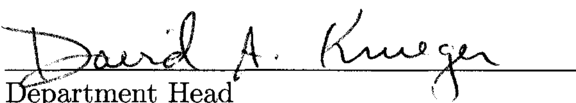

Department Head

Reproduced with permission of the copyright owner. Further reproduction prohibited without permission.

ABSTRACT OF DISSERTATION

DEVICE PHYSICS OF $Cu(In,Ga)Se_2$ THIN-FILM SOLAR CELLS

Thin-film solar cells have the potential to be an important contributor to the global energy demand by the mid-21st-century. $Cu(In,Ga)Se_2$ (CIGS) solar cells, which have achieved laboratory efficiencies close to 20%, are highly attractive, because their band gap is near the optimal value, their polycrystallinity is not significantly detrimental to their performance, and the broad choice of heterojunction partners available allows additional degrees of freedom for optimizing their performance. Although steady progress has been made for CIGS solar cells, this progress has largely been driven by empirical optimization rather than by in-depth understanding of appropriate physical models. This thesis is intended to fill some of the gaps that exist between state-of-the-art experimental solar cells and their device physics. The level of complexity involved is largely prohibitive to analytical treatment and, hence, numerical approaches are primarily utilized.

The dominant topics for CIGS solar cells covered in this dissertation are (1) variation in the Ga/(Ga+In) stoichiometry ("grading"), (2) the formation of "good" heterojunctions, (3) photoconductive effects in window or buffer materials, (4) the apparently benign or even beneficial presence of grain-boundaries (GBs), including a discussion of charged GBs and the effects of Cu-depletion near GBs. This work establishes a baseline model for CIGS solar cells and, from this starting point, the device physics relating to these questions is discussed and principles are identified that apply to a broad range of devices.

CIGS grading is shown to have only small potential to improve device performance. This conclusion conflicts with earlier studies, and it is shown that the difference arises in the evaluation of the grading benefit, in particular, the proper choice of the reference performance. Band-gap increases toward the front of the device are most likely detrimental, while band-gap increases toward the back can be modestly beneficial. The popular "double grading" approach achieves only very small additional gains over the simple back grading approach. Very thin-absorber cells can benefit substantially from back grading, because in this case, grading can mitigate detrimental back-contact surface recombination.

Reproduced with permission of the copyright owner. Further reproduction prohibited without permission.

The window/absorber interface is studied and, in good agreement with experiments, a limitation of the open-circuit voltage is observed for wide-band-gap CdS/CIGS solar cells. This limitation can be circumvented by a change in window or buffer material to establish a positive conduction band-offset, a down-shift of the valence-band at the interface by Cu-depletion, or appropriate pinning of the Fermi level at the interface. All these mechanisms deplete the interface of hole carriers and lead to lower interface recombination.

Photoconductivity in CdS buffer layers has been thoroughly studied in the past, but approaches were mostly phenomenological and a quantified description of the transport mechanisms involved has been missing. This topic is revisited, a model that reproduces experimental results is established, and the details of carrier transport are discussed.

Grain boundaries (GBs) in CIGS solar cells have not previously been investigated with respect to their influence on device performance. In particular, charging of GBs and a possible depletion of Cu at grain surfaces may be critically important for high performance polycrystalline CIGS cells. Based on first-principles calculations and experiments, Cu depletion shifts the valence-band edge downward, enlarging the band-gap energy. A two-dimensional model allows the study of recombination at GBs, charged defects at GBs, and valence-band offsets at GBs. It is found that (1) the GB recombination velocity would need to be less than 10^4 cm/s to allow for the observed record-level efficiencies, (2) small electron-attractive GB potentials lower both photocurrent and photovoltage, (3) large electron-attractive GB potentials increase photocurrent, but lower photovoltage with a net decrease in device efficiency, (4) small hole-attractive GB potentials are somewhat beneficial, (5) valence-band offsets reduce GB recombination and result in performances comparable to GB-free cells. Analytical approaches are used to solidify the understanding of the obtained results. It is concluded that GBs in CIGS solar cells are unlikely to be strongly charged and that record-level efficiencies require the inherent absence of GB recombination centers or an effective passivation such as that established by a valence-band offset at GBs. Limits and approximations of the GB models are discussed.

Markus Gloeckler
Physics Department
Colorado State University
Fort Collins, CO 80523
Summer 2005

Reproduced with permission of the copyright owner. Further reproduction prohibited without permission.

ACKNOWLEDGMENTS

My deepest gratitude goes to my parents, Alois and Zenta Glöckler, thank you for supporting me in whatever I do. I know, in particular, the great distance between us has been hard for you at times. My sister Martina and her family, Bernhard, Julia, Tobias, and Jasmin, for always giving their best to stay in touch and who make our breaks from work so enjoyable. Alex and Leif for being such good friends, and for the great many hours we traveled the worlds. Rainer and Michi (and Hanna) and Stephanie who were always supportive of my plans and also thanks for the enjoyable hours over Glühwein and Bier.

The underwater hockey team at Colorado State University with its many volatile and few permanent members. Thank you so much for not breaking my nose or any other bone (yet). Particularly, thanks to Jorge's urging nature that can't take a "no" for an answer and made me try. Very warm thanks go to my friend Betty, who in her generosity has taken me in when I came here the first time, and her place has served as a home away from home ever since my first days in Fort Collins. There are few better ways to spent a couple of hours, than over tea, cookies, and gossip at her always open house.

My adviser Jim, who offered me work as an intern at Colorado State University. Work that I gladly accepted and returned to for this lengthy task. Thanks for supporting my research ideas, for giving me the leeway to do independent work, for letting me travel and present my work, and of, course, for teaching me. Most of all, thanks for being a good friend and mentor.

Thank you Jill for dealing with me at all times. Having you makes it all worthwhile.

Reproduced with permission of the copyright owner. Further reproduction prohibited without permission.

Thanks to...

my committee members for reviewing this manuscript; Tim Nagle, Alan Davies, and Ana Kanevce for proofreading; many colleagues in the thin-film community that have stimulated a lot of this work with engaged discussions and their good work; Prof. Marc Burgelman for providing SCAPS-1D and continuous support, even to 'onverbeterlijke' users as myself; Pennsylvania State University for providing the software package AMPS-1D, which was developed with funding from the Electric Power Research Institute.

The author gratefully acknowledges the collaboration with the National Renewable Energy Laboratory that provided the software for the 2D studies of grain boundaries. Funding through the NREL thin-film partnership program and the New Energy Development Organization is gratefully acknowledged.

Reproduced with permission of the copyright owner. Further reproduction prohibited without permission.

Contents

1 Motivation 1

2 Background 7

2.1 Solar-cell basics 7

2.1.1 Important semiconductor concepts 7

2.1.2 Homojunctions 9

2.1.3 Heterojunctions 11

2.1.4 Thin-film solar cells 12

2.2 Electrical characterization methods 15

2.2.1 Current-density vs. voltage 16

2.2.2 Quantum efficiency 19

3 Basics of numerical simulations 22

3.1 Governing equations 22

3.1.1 Transport 23

3.1.2 Generation 24

3.1.3 Recombination 25

3.2 Baseline parameters 27

3.2.1 $ZnO/CdS/Cu(In,Ga)Se_2$ solar cells 30

3.2.2 $SnO_2/CdS/CdTe$ solar cells 31

3.3 Software 35

3.3.1 AMPS-1D 35

3.3.2 SCAPS-1D 36

Reproduced with permission of the copyright owner. Further reproduction prohibited without permission.

3.3.3 ISE-TCAD (DESSIS) 37

4 One-dimensional simulations: absorber grading, heterojunction interface, and photoconductive buffer layer 39

4.1 Compositional Ga/(Ga+In) grading in Cu(In,Ga)Se_2 40

4.1.1 Review 40

4.1.2 Model 42

4.1.3 Identifying the true grading benefit 43

4.1.4 Results 44

4.1.5 Summary 52

4.2 Band alignment at the CdS/CIGS heterojunction 53

4.2.1 Review 54

4.2.2 Model 54

4.2.3 Bulk vs. interface recombination 56

4.2.4 Alternative windows — efficiency limits 59

4.2.5 Surface modifications 61

4.2.6 Fermi-level pinning 62

4.2.7 Summary 63

4.3 Photoconductive window and buffer layers 64

4.3.1 Review 64

4.3.2 *J-V cross-over* 66

4.3.3 "Red kink" 70

4.3.4 Summary 73

5 Advanced two-dimensional simulations: grain boundaries 74

5.1 Review 75

5.1.1 Analytical and numerical models 75

5.1.2 Micro- and macro-characterization of GBs 77

5.2 Model description 78

5.3 Neutral grain boundaries 80

5.3.1 Horizontal grain boundaries 81

Reproduced with permission of the copyright owner. Further reproduction prohibited without permission.

5.3.2 Columnar grain boundaries 83
5.3.3 Comparison of bulk and grain-boundary recombination 89
5.3.4 Analytical model 91
5.3.5 Summary 97
5.4 Charged grain boundaries 98
5.4.1 Results 102
5.4.2 Discussion of hole-repulsive band-bending 104
5.4.3 Discussion of electron-repulsive band-bending 107
5.4.4 Analytical model 108
5.4.5 Summary 111
5.5 Band-discontinuities at grain boundaries 111
5.5.1 Valence-band offsets 114
5.5.2 Combination of valence-band offsets and charged grain boundaries . 118
5.5.3 Summary 120
5.6 Short-comings of the GB models 120
5.7 Summary 123

6 Conclusions **126**

A Tabulated spectral input for the CIGS baseline **130**

B Tabulated spectral input for the CdTe baseline **132**

Reproduced with permission of the copyright owner. Further reproduction prohibited without permission.

List of Figures

1.1 Learning curve of photovoltaics. 2
1.2 Building integrated PV installation on a farm house in the author's hometown. 4

2.1 Formation of a p-n junction in the Schottky approximation. 10
2.2 Conduction and valence band for a heterojunction solar cell; the case of ZnO/CdS/CIGS. 12
2.3 Schematic of a grid/ZnO/CdS/CIGS/Mo/glass solar cell. 13
2.4 SEM image of a CIGS solar cell at 20000x magnification. 15
2.5 Current-voltage curve for an (a) ideal and (b) non-ideal solar cell. 17
2.6 Four step analysis of J-V curves. 18
2.7 Software implementation of the four-step J-V analysis. 19
2.8 Example of a quantum-efficiency curve and involved loss mechanisms. . . . 20

3.1 Calculated total generation in a ZnO/CdS/CIGS solar cell. 25
3.2 The four allowed transitions in the Shockley-Read-Hall model. 26
3.3 Simulation results for the CIGS and CdTe baseline cases. 33
3.4 Bands, carrier concentrations, and recombination profile for the CIGS baseline case at zero and forward bias. 34

4.1 Typical grading approaches. 41
4.2 Reported maximum efficiency gains for CIS or low-Ga CIGS solar cells from simulation or experimental studies. 42
4.3 Efficiency and open-circuit voltage for uniform band-gap absorbers with thicknesses of 3 μm and 0.5 μm. 43
4.4 Objective evaluation of grading benefits by comparison to common V_{oc}. . . 44
4.5 Performance evaluated for back gradings with ΔE_{Ba} = 0–0.6 eV. 45
4.6 Back grading with ΔE_{Ba} = 0.5 eV and d_{min} = 1 μm. Conduction and valence bands and quasi-Fermi levels under one-sun illumination and zero bias. . . . 46
4.7 Performance evaluated for front gradings with ΔE_{Fr} = 0–0.3 eV. 48
4.8 Conduction band at zero bias and forward bias for front gradings. 49
4.9 Performance evaluated for double gradings with ΔE_{Fr} = 0–0.3 eV and ΔE_{Ba} = 0–0.6 eV. 50
4.10 Solar-cell efficiency with varying back/front grading ratio. 51
4.11 Performance evaluated for thin CIGS solar cells with back gradings. 52
4.12 Conduction and valence band for (a) a small and (b) a large band-gap ZnO/CdS/CIGS solar cell. 55
4.13 Simulated J-V parameters with increasing density of bulk recombination centers. 57

Reproduced with permission of the copyright owner. Further reproduction prohibited without permission.

4.14 Effects of interface recombination on V_{oc} and η. 58
4.15 Comparison of the V_{oc}-limitation ($S \sim 10^5$ cm/s) and experimental results. 58
4.16 V_{oc} and η with different band alignments. 60
4.17 Band gap widening in the (a) conduction band or (b) valence band. 61
4.18 Pinning of the Fermi level by donor interface states. The defects are located at a fixed distance above the valence band or below the conduction band. . 63
4.19 Conduction-band lowering due to the "photo-doping" in CdS. 66
4.20 Comparison of J-V curves from experiment and simulation at three temperatures. 67
4.21 Conduction band and quasi-Fermi level for the device model in the dark and under illumination. 69
4.22 Current-voltage curves calculated in the dark and under red and white light illumination with increasing conduction-band offset. 70
4.23 J-V curves for $\Delta E_C = 0.45$ eV under white and red light illumination. The voltage loss, ΔV_{oc}, is positive or negative depending on the net current flow. 72
4.24 Bands for the case of $\Delta E_C = 0.45$ eV. 72

5.1 Schematic model configuration (not so scale) for (a) columnar GBs and (b) horizontal GBs. 78
5.2 Examples of mesh configuration; black lines correspond to mesh lines. In the simulations, a solution is found for all points where the mesh lines intercept (node points). 80
5.3 J-V performance with horizontal GBs at a distance z_{gb} from the CdS/CIGS interface. 82
5.4 Conduction band, valence band, and electron and hole quasi-Fermi level (top). Recombination rate and electron and hole density (bottom). 83
5.5 J-V and QE curves with columnar GBs for selected values of S_{gb}. 84
5.6 J-V parameters for columnar GBs with $S_{gb} = 10^2$–10^7 cm/s. 84
5.7 p/n and R for neutral columnar GBs 86
5.8 GB and bulk recombination with increasing S_{gb}. 87
5.9 Schematic of grain boundaries that either (a) expand or (b) shift through the device along the z-axis. 88
5.10 J-V results for partial grain boundaries. 88
5.11 Comparison of bulk and grain-boundary recombination. 89
5.12 J-V parameters with varying grain size for columnar GBs. 91
5.13 Illustration of the photocurrent calculation. 93
5.14 Short-circuit current density for different analytical models. 96
5.15 Comparison of numerical vs. analytical and 2D vs. 3D model. 97
5.16 Charge distribution, electric field, and potential at GBs. 98
5.17 Two-dimensional model with charged grain-boundaries. 100
5.18 Bands and carrier concentration for ϕ_{gb} = -0.05 eV, +0.2 eV and +0.6 eV. . 101
5.19 J-V parameters V_{oc}, J_{sc}, FF, and η for ϕ_{gb} = -0.05 eV (electron repulsion), 0.2 eV (weak hole repulsion), and 0.6 eV (strong hole repulsion). 103
5.20 J-V parameters with positive and negative electrostatic potential ϕ_{gb}. . . . 104
5.21 p/n and R for small hole-repulsive band-bending. 105
5.22 p/n and R for large hole-repulsive band-bending. 106
5.23 Band-bending in the absorber at $z = 1$ μm under forward bias. 107
5.24 p/n and R for small electron-repulsive band-bending. 108

Reproduced with permission of the copyright owner. Further reproduction prohibited without permission.

5.25 Effect of charge-induced band-bending on current. 109
5.26 Electron and hole current flows with ϕ_{gb} =0.4 eV. 110
5.27 Schematic of the valence-band offset model. 112
5.28 Bands and carrier concentration for $\Delta E_V = 0.2$ eV, +0.4 eV, and $\phi_{gb} = \Delta E_V$ = 0.2 eV models. 113
5.29 J-V parameters vs. S_{gb} in the presence of ΔE_V. 115
5.30 J-V parameters vs. ΔE_V. 116
5.31 p/n and R for large shifts of the valence-band energy at the GB. 117
5.32 J-V results for combinations of ϕ_{gb} and ΔE_V, $S_{gb} = 10^5$ cm/s. 118
5.33 J-V results for combinations of ϕ_{gb} and ΔE_V, $S_{gb} = 10^7$ cm/s. 119
5.34 Device performance with variation of the donor characteristic energy. 122
5.35 Tunneling through a rectangular barrier. 123
5.36 Typical current-voltage curves for all GB models considered. 124

Reproduced with permission of the copyright owner. Further reproduction prohibited without permission.

List of Tables

2.1 Basic J-V performance parameters. 16

3.1 Parameters describing photogeneration in a ZnO/CdS/CIGS solar cell. . . . 24
3.2 CIGS baseline case input parameters. 31
3.3 CdTe baseline case input parameters. 32
3.4 Performance parameters of the baseline cases. 34

4.1 Summary of the grading benefits. 53

5.1 Simulation grain-boundary parameters. 79
5.2 "Bulk equivalent" and grain boundary models. 90
5.3 Parameters for ϕ_{gb} = -0.05 eV, +0.2 eV, and +0.6 eV models. 100
5.4 Parameters for ΔE_V = 0.2 eV, +0.4 eV, and $\phi_{gb} = \Delta E_V$ = 0.2 eV models. 112

A.1 Illumination and absorption spectra 130

B.1 Illumination and absorption spectra 132

Reproduced with permission of the copyright owner. Further reproduction prohibited without permission.

Symbols

A	diode quality factor	
α	absorption coefficient	[cm^{-1}]
ΔE_C, ΔE_V	conduction- and valence-band offset	[eV]
ΔE_{Ba}, ΔE_{Fr}	band-gap increase toward the back or front	[eV]
d_g	distance between two columnar GBs = "grain size"	[cm]
$\mathcal{E}$	electric field	[V/cm]
ϵ	electric permittivity; ϵ/ϵ_0 = dielectric constant	[F/m]
E_C, E_V	conduction-band minimum and valence-band maximum	[eV]
E_f	equilibrium Fermi level	[eV]
E_{fn}, E_{fp}	electron and hole quasi-Fermi level	[eV]
E_g	band-gap energy of the semiconductor	[eV]
FF	fill factor	[%]
Φ	photon flux density	[#/cm^{2}s]
ϕ_{gb}	electrostatic grain-boundary potential	[eV]
G	generation rate	[cm^{-3}s^{-1}]
η	solar-cell efficiency under one-sun illumination	[%]
J_0	diode saturation current density	[mA/cm^2]
J_{sc}	short-circuit current density	[mA/cm^2]
k	Boltzmann constant	[J/K]
m_e^*, m_h^*	electron and hole effective mass	[kg]
μ_e, μ_h	electron and hole mobility	[cm^2/Vs]
n	free electron density	[cm^{-3}]
N_C, N_V	effective density of states in the conduction and valence band	[cm^{-3}]
n_i	intrinsic carrier density	[cm^{-3}]
N_A	bulk absorber doping	[cm^{-3}]
N_{gb}	density of grain-boundary states	[cm^{-2}]
p	free hole density	[cm^{-3}]
q	elementary charge	[C]
R_{bulk}	bulk recombination rate	[cm^{-3}s^{-1}]
R_F	front reflection	
R_{gb}	GB recombination rate	[cm^{-2}s^{-1}]
S_{gb}	GB recombination velocity	[cm/s]
T	absolute temperature	[K]
τ_e, τ_h	electron and hole lifetime	[s]
V_{oc}	open-circuit voltage	[V]
W_{SCR}, W_{QNR}	width of the space-charge and quasi-neutral region	[cm]

Reproduced with permission of the copyright owner. Further reproduction prohibited without permission.

Abbreviations

AM1.5	standard terrestrial solar spectrum 'Air Mass 1.5'
BL	baseline [model]
CBO	conduction-band offset
CE	collection efficiency
CGS	$CuGaSe_2$
CIGS	$Cu(In,Ga)Se_2$
CIS	$CuInSe_2$
$F(E)$	Fermi distribution
GB	grain boundary
J-V	current-density vs. voltage [curve]
one-sun	used as a synonym for AM1.5 illumination
PV	photovoltaic
PX	polycrystalline
QE	quantum efficiency
QNR	quasi-neutral region
SCR	space-charge region
SEM	scanning electron microscopy
SRH	Shockley-Read-Hall [recombination]
WKB	Wentzel-Kramers-Brillouin [approximation]

Reproduced with permission of the copyright owner. Further reproduction prohibited without permission.

Chapter 1

Motivation

From the dictionary [1]:

solar cell:	*a photovoltaic cell that converts sunlight directly into electricity.*
thin film:	*a film of material only a few microns thick, deposited on a substrate, as in the technology for making integrated circuits.*

Why bother?

Only after having worked on thin-film solar cells for some time, and after I had exposure to the thin-film photovoltaic (PV) community and the political aspects that come with it, did I ask the question, why we should bother about photovoltaics, myself. Before that time, solar cells were simply inherently "cool," as they are obviously something "very green," produce a high form of energy out of nowhere, and do this with virtually no effort. There are a few inaccuracies in this early perception that need to be addressed: First, energy is not produced by solar cells, but, of course, merely converted. On the other hand, conversion of something that is naturally lost, e.g., sunlight incident on earth, appears very much as a net gain (or "production"). Further and more important questions are: (1) Is PV really "green," and is it "green enough" that we need to care about it? (2) Can PV really make an impact? (3) And if it does, will it be for economic, ecological, or political reasons?

Reproduced with permission of the copyright owner. Further reproduction prohibited without permission.

Photovoltaics today

The PV industry has grown into a multi-billion dollar business and production of PV modules, large area conglomerates of solar cells, surpassed the 1 GW for the first time in 2004 and is expected to reach 3 GW by 2010 [2]. The market has been growing at double digit rates over recent years (20–40% annually) [2, 3] and prices, usually referred to in dollars per peak watt ($/Wp), are continuously falling, roughly with a "learning curve" of 80% (Figure 1.1 after Ref. [4]). A further increase of the cumulative production by a factor of 100 will lead to cost equality with fossil fuels. This can be expected to occur in roughly 15 years, if the technology continues to follow the 80% learning curve. Unfortunately, learning curves tend to experience a "change in slope" once a technology is sufficiently matured and prices stabilize, as it was seen for gas and wind turbines in the early 1960's and 1990's, respectively [4]. Photovoltaic crystalline-silicon technology is likely to also hit a lower price limit, because of the expensive processing involved. Cheaply deposited thin-film solar cells are the more promising candidate for super-large-scale production.

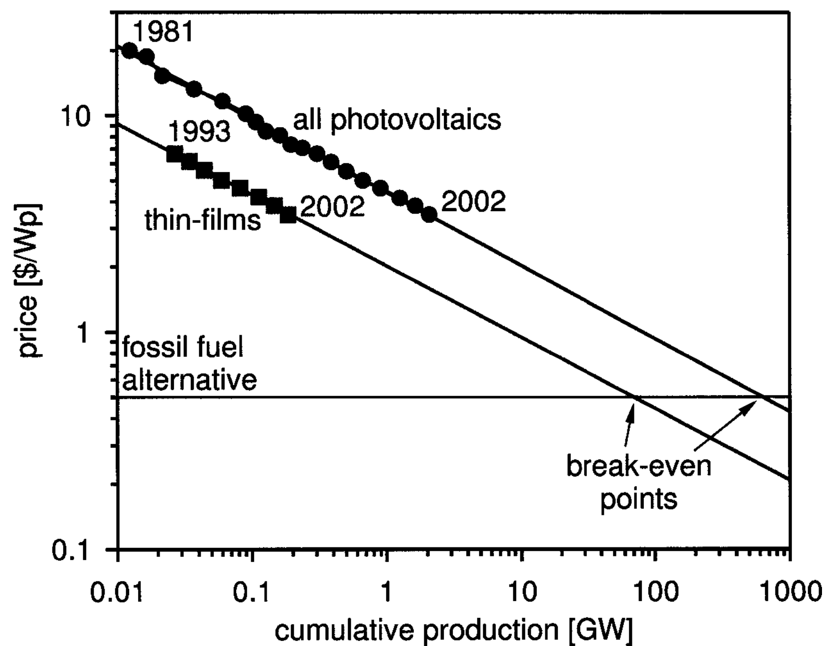

Figure 1.1: Learning curve of photovoltaics. Thin-films have a significant cost advantage, because the learning curves starts from a lower base. Compared to Si technology, thin-films have achieved similar total costs at substantially lower production volumes. Data reproduced from Green [4].

Reproduced with permission of the copyright owner. Further reproduction prohibited without permission.

Today's economic success of PV is important as it fosters future developments, but it crucially depends on political incentives such as "feed-in tariffs," as they have been established in several European countries (e.g., Ref. [5]), installation subsidies, or high electricity costs in general. *Thin-film* solar cells have currently less than 10% market share in PV module shipments, which are dominated by crystalline Si technology. The overall electricity production from solar installations is still negligible in comparison to the world energy demand. However, taking the incentives as granted or under consideration of the high electricity costs in parts of the world, e.g., Japan, photovoltaic energy is a highly competitive and lucrative market today. This demand has caused a major shortage in the solar module market and a great rush toward increasing the production capacity in 2004.

Returning to the green aspect of photovoltaic energy conversion, PV is an inherently clean form of energy once it is installed in the field. Solar modules convert the incident solar radiation directly into electricity, require no fuel, and produce no exhausts or other bi-products. However, in order to be a sustainable clean form of energy, one also needs to consider what is necessary to produce a solar module. Other frequent objections to solar power are that they require huge land areas and that we may not have enough rare materials to produce substantial quantities of solar cells.

The question of sustainability requires that solar modules "generate" substantially more energy during their estimated 30-year lifespan than what is necessary in the manufacturing process of the solar module. For current Si technologies this "payback" time is estimated roughly at 3–4 years, for thin-films 3 years or less. Both numbers include the total system cost [6]. These numbers are anticipated to further decrease to as low as 2 years for Si and 1 year or less for thin-films. Silicon and most other materials are readily available for any amount of solar-cell production that one could foresee, but some materials, such as indium in $Cu(In,Ga)Se_2$ solar cells, could become a bottleneck, if the production would eventually reach TW levels [7]. The land area necessary to produce solar power is in general grossly overestimated. Roughly 0.25 TW of electricity could be generated by building integrated PV, i.e., mostly on roofs (Fig. 1.2). 1.7% of the US land area would generate as much as 3.3 TW, which corresponds approximately to the *total* energy consumption (3.3 TW $\times$ 1 year) in the US in 2000. This land area is similar to what is used for interstate highways,

Reproduced with permission of the copyright owner. Further reproduction prohibited without permission.

Figure 1.2: Building integrated PV installation on a farm house in the author's hometown. After the passage of the Renewable Energy Law in Germany, many private investors use this opportunity to invest in solar energy with practically guaranteed return and profits on investments.

which proves that if the necessity is established, a project of this size can be accomplished.

To summarize the current situation, the solar-cell market is highly lucrative at the moment due to guaranteed feed-in tariffs and high electricity prices in parts of the world. The learning curves predict further substantial price reductions as the market grows at rates of 20–40%. Other than economic considerations, there are no constraints in sight that will limit the success of solar energy. The current situation of thin-film technology and state-of-the-art solar cells have been recently reviewed [8, 9].

Photovoltaics 2050

With our ever increasing industrialization and growth in world population, we, as in "humanity" may face major challenges in the future energy demand. Only the tip of the iceberg is presented here, and for in-depth discussion the reader is referred to recent publications of the National Renewable Energy Laboratory [10], the World Energy Assessment [11], and discussions by Hoffert et al. [12] and Lewis [13]. By 2050, the average power demand is expected to increase, mostly due to the increase in world population and development in countries such as China and India, from 13 TW (2000) to roughly 30 TW. Our current energy mix is heavily focused on fossil fuels and there is no change in sight, since reserves

Reproduced with permission of the copyright owner. Further reproduction prohibited without permission.

for fossil fuels, particularly coal, are sufficient to meet this future demand.

The driving factor for renewable energies will become the increased level of greenhouse gas emissions, particularly CO_2, that accumulate in our atmosphere. The atmospheric CO_2 concentration has raised from roughly 280 parts per million (ppm) to 360 ppm [11] since the late 19th century. Increases to 450–550 ppm are predicted to cause major climatic changes. At the current rate of fossil-fuel consumption, and assuming the increased global energy demand will also use fossil fuels, the CO_2 concentration is predicted to raise as high as 750 ppm by 2050, tripling the pre-industrial concentration [13]. In this scenario, the planet earth could very quickly become a less habitable place to live. Quoting David Stipp on his article in FORTUNE magazine [14]: *Global warming, rather than causing gradual, centuries-spanning change, may be pushing the climate to a tipping point. ... Though triggered by warming, such change would probably cause cooling in the Northern Hemisphere, leading to longer, harsher winters in much of the U.S. and Europe. Worse, it would cause massive droughts, turning farmland to dust bowls and forests to ashes.*

The alternative to the "business as usual" approach requires that we reduce the CO_2 emissions as soon as possible, and that we are ready to supply a good portion of the demand (10–30 TW) by 2050 with renewable, emission-free energy sources. Lewis [13] reviews possible candidates for clean energy production, including nuclear fission, hydro-power, biomass, wind, geothermal, and solar energy and he concludes that solar power is the only source that has the potential to face this demand. While hydro, biomass, geothermal, and wind power can sustain fractions of this demand, for practical reasons the maximum power supplied by these techniques will be limited. Nuclear fission, has the potential to supply CO_2-free power, but it would require to built one nuclear 1 GW reactor every other day to meet the 10 TW demand in 2050, and even if this could be accomplished, we might run out of uranium on a rather short time scale. Solar power is incident on earth at a rate of $\sim 10^5$ TW and offers great potential to meet this increased demand in CO_2-free energy. The high costs associated with PV, however, require that political driving forces are established to enable the necessary growth of the technology. The realization of this global goal will require a concerted effort throughout the world and across borders.

The question at hand is not whether humanity should or will use solar power, but

Reproduced with permission of the copyright owner. Further reproduction prohibited without permission.

rather what alternatives are available for our energy future. Solar power offers a great clean opportunity at hand and unless other energy sources become available, it might be the only one that can prevent climatic catastrophes before the end of this century.

Reproduced with permission of the copyright owner. Further reproduction prohibited without permission.

Chapter 2

Background

Important principles and properties of semiconductors and solar cells are briefly reviewed as far as these are helpful for the understanding of this work. This section includes a brief description of state-of-the-art $Cu(In,Ga)Se_2$ (CIGS) solar cells. Although this dissertation is focused on numerical simulations of solar cells, it is essential to review basic measurement principles as well, because it is exactly the results of these measurements that are calculated in the numerical simulations. The discussion is limited to current density vs. voltage (J-V) and quantum efficiency (QE) measurements.

2.1 Solar-cell basics

2.1.1 Important semiconductor concepts

Semiconductors are a family of solids in which there exists a moderate gap (up to a few electron volts) in the distribution of allowed energy states. At $T = 0$ K in a pure material, this gap separates one entirely filled band (valence band) from one that is entirely empty (conduction band). For $T > 0$ K, a finite number of electronic states are occupied in the conduction band ("free electrons") and a finite number of states are unoccupied in the valence-band ("free holes"). These free electrons and holes can gain kinetic energy since a quasi-continuum of higher or lower states are available to them, respectively, and they are therefore able to respond to electric fields and concentration gradients that allow for macroscopic current flow.

Reproduced with permission of the copyright owner. Further reproduction prohibited without permission.

The equilibrium concentrations of electrons and holes can be modified by extrinsic dopants, but also by defect levels (additional states within the band gap) that are intrinsic to the semiconductor. The occupation of conduction- and valence-band states is governed by Fermi-Dirac statistics,

$$F(E) = \frac{1}{1 + exp\left(\frac{E-E_f}{kT}\right)} \tag{2.1}$$

where k is the Boltzmann constant and T the absolute temperature. Equation 2.1 describes the probability of electron occupation in the conduction band and, similarly, 1-$F(E)$ describes the probability for holes in the valence band. If the Fermi-level E_f is not very close to either band edge, $E_C - E_f \gg kT$ and $E_f - E_V \gg kT$, $F(E)$ and 1-$F(E)$ can for many practical purposes be replaced by the Boltzmann factors

$$exp\left(-\frac{E-E_f}{kT}\right) \quad \text{and} \quad exp\left(-\frac{E_f - E}{kT}\right) \tag{2.2}$$

for electrons in the conduction band and holes in the valence band, respectively.

Semiconductors are classified as n- or p-type depending on whether electrons or holes are the majority carriers. The Fermi level can be calculated by the following relations:

$$n = N_C \cdot exp\left(-\frac{E_C - E_F}{kT}\right) \tag{2.3}$$

and

$$p = N_V \cdot exp\left(-\frac{E_F - E_V}{kT}\right) \tag{2.4}$$

where

$$N_C = 2\left(\frac{2\pi m_e^* kT}{h^2}\right)^{3/2} \quad \text{and} \quad N_V = 2\left(\frac{2\pi m_h^* kT}{h^2}\right)^{3/2} \tag{2.5}$$

are the effective densities of states in the conduction and valence band. For semiconductors doped either with shallow donor or acceptor levels, n is similar to the donor density and p is similar to the acceptor density. All parameters in Eq. 2.5 have their usual meaning, m_e^* and m_h^* are the electron and hole effective masses. In equilibrium, the product of n and p is constant and depends only upon the temperature, effective masses, and band gap of the semiconductor,

$$np = n_i^2 = N_C \cdot N_V \cdot exp\left(-E_g/kT\right). \tag{2.6}$$

Reproduced with permission of the copyright owner. Further reproduction prohibited without permission.

Non-equilibrium

In non-equilibrium conditions, such as under illumination or under carrier injection due to externally applied electric bias, no uniform Fermi level exists. In steady-state, however, quasi-Fermi levels, E_{fn} and E_{fp}, can be introduced, which are useful in the analysis and interpretation of semiconductors. These quasi-Fermi levels are defined by

$$n = N_C \cdot exp\left(-\frac{E_C - E_{fn}}{kT}\right) \tag{2.7}$$

and

$$p = N_V \cdot exp\left(-\frac{E_{fp} - E_V}{kT}\right). \tag{2.8}$$

Assuming that E_{fn} and E_{fp} in the n- and p-type region of a p-n junction diode are in equilibrium with the respective electrical contact, the difference between the quasi-Fermi levels in the proximity of a diode's space-charge region is given by the applied voltage V, and it follows that the np product is voltage dependent:

$$np = n_i^2 \cdot exp\,(qV/kT)\,. \tag{2.9}$$

Numerical solution of the p-n junction problem, including generation, recombination, and transport, is discussed in Sect. 3.1. Further information on the properties of semiconductors can be found in many semiconductor [15] or solar-cell textbooks [16–18].

2.1.2 Homojunctions

Intimate contact between n- and p-type semiconductors allows for exchange of electrons and holes until an equilibrium situation is achieved. Electrons diffuse into the p-type material, leaving behind ionized shallow donor levels, and holes diffuse into the n-type material, leaving behind ionized shallow acceptor levels. Adjacent to the p-n interface, both semiconductors deplete of free carriers and a space-charge region (SCR) is established. This is shown in Fig. 2.1(a) for a p-n homojunction assuming a n and p doping of 10^{16} cm^{-3}. The diffusion process stops once the drift current established by the electric field, Fig. 2.1(b), exactly cancels the diffusion current, and a flat Fermi level is established throughout the device. It is conventional to draw the conduction and valence-band edges in terms of the

Reproduced with permission of the copyright owner. Further reproduction prohibited without permission.

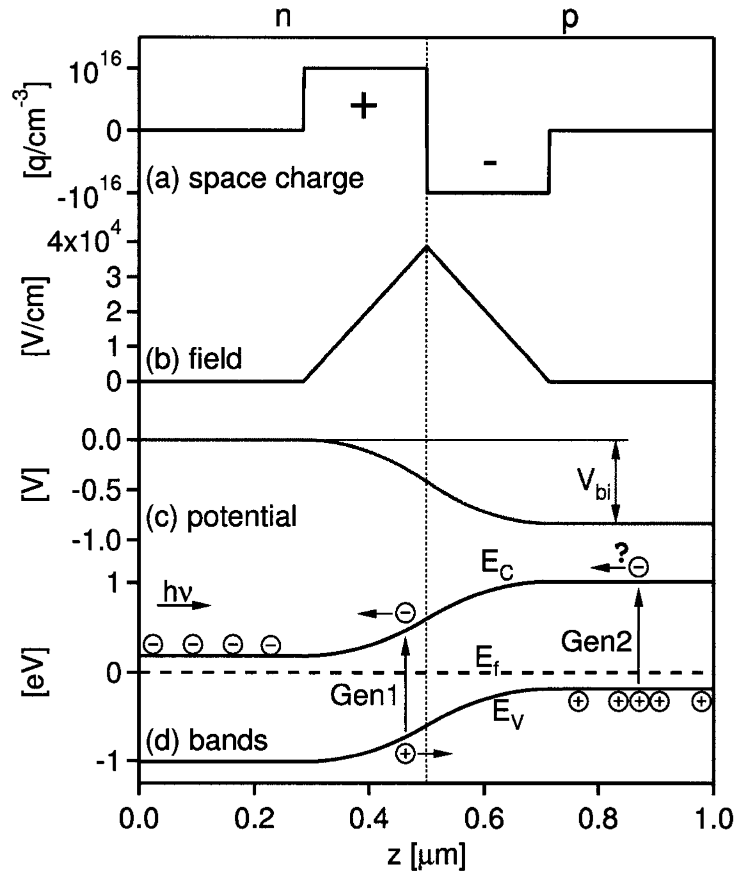

Figure 2.1: Formation of a *p*-*n* junction in the Schottky approximation. (a) space-charge distribution due to fixed ionized dopants; (b) electric field obtained by integration of the Poisson equation; (c) a second integration step results in the electrostatic potential. The built-in potential V_{bi} describes the potential difference between the *n* and *p* side of the junction in equilibrium. Collection of photo-carriers requires that the applied voltage $V < V_{bi}$ and, therefore, V_{bi} is an upper limit to the open-circuit voltage of a solar cell (Sect. 2.2.1); (d) conduction-band minimum E_C, valence-band maximum E_V, and the Fermi level in equilibrium. Schematically, the generation of an electron-hole pair within (Gen1) and outside (Gen2) the SCR is shown.

electron energy and, hence, the electrostatic potential $\phi = -E_C +$ (constant) (Fig. 2.1[c] and [d]).

Figure 2.1(d) further illustrates the principle of a *p*-*n* junction solar cell. Incident light (e.g., from the left) generates additional electron-hole pairs in the solar cell. If the generation occurs within the SCR, both carriers are readily swept out by the electric field (process "Gen1" in Fig. 2.1[d]). The hole quickly reaches the *p*-type region and the electron the *n*-type region; once both carriers are majority carriers, they can then safely traverse the quasi-neutral region (QNR) and be collected at external electrical contacts. In case of

Reproduced with permission of the copyright owner. Further reproduction prohibited without permission.

generation outside of the SCR, either in the n- or p-type bulk material (illustrated in "Gen2" in Fig. 2.1[d]), one of the two generated carriers is a minority carrier (electron in Fig. 2.1[d]) and must traverse to the SCR before it recombines; the success of this diffusion transport depends on the quality of the material and is often expressed in terms of a carrier lifetime τ or a diffusion length L.

2.1.3 Heterojunctions

The situation of a p-n homojunction solar cell depicted in Fig. 2.1(d) is far from ideal. Light generation of carriers decreases exponentially with the penetration depth (Sect. 3.1.3) and, therefore, assuming the light is incident from the n-type side of the solar cell, most of the generation would occur in the n-type QNR region and not within the SCR where good collection would be ensured.

There are two effective approaches to improve upon this situation: (1) thinning of the n-type material, an approach often taken in Si based solar cells, or (2) using a n-type material with an enlarged band-gap energy. The latter shifts the generation profile directly into the junction, since the larger band-gap energy prevents absorption in the n-type layer, and such configuration can form a very efficient solar cell. This is the concept of heterojunction solar cells such as ZnO/CdS/CIGS, which will be discussed in this work. CIGS is a short-hand for $Cu(In,Ga)Se_2$. The n-type layers are often referred to as "window" layers, due to their intended photon transparency.

The band diagram for a ZnO/CdS/CIGS solar cell is shown in Fig. 2.2. Photons with energy $E_{ph} < 3.3$ eV will pass through the ZnO window layer. Some photons with energy 2.4 eV $< E_{ph} < 3.3$ eV will be absorbed in the CdS buffer layer, which was introduced into these devices for technological reasons, but most will reach the CIGS layer and be strongly absorbed in the SCR. CIGS, as well as CdTe, are direct-gap semiconductors with very strong absorption, such that the absorption length is very short, $\alpha^{-1} \ll 1$ μm. The detrimental CdS absorption is minimized by thinning this layer or alloying it with other elements to increase its band-gap energy [19]. Several important aspects of this band diagram will be discussed in Chapter 4.

Reproduced with permission of the copyright owner. Further reproduction prohibited without permission.

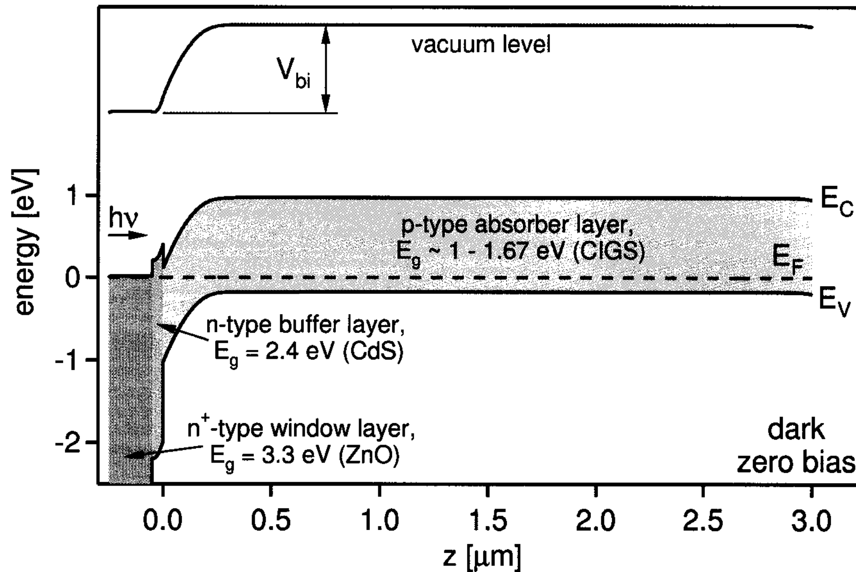

Figure 2.2: Conduction and valence band for a heterojunction solar cell; the case of ZnO/CdS/CIGS.

2.1.4 Thin-film solar cells

Sunlight is incident on earth (at sea level) with a power density of ~1000 W/m^2 and, hence, to run a standard 100 W light bulb by solar power, an area of roughly 1 m^2 is required (even more if the light bulb runs 24 hours or adverse weather is considered). For significant energy production, large-area solar-cell installations are necessary. In comparison to wafer based Si technology, thin-film solar cells can be cheaply deposited on large areas of (soda-lime) glass [20], stainless steel [21], or even on polyimide substrates, which would make these solar cells truly lightweight [22, 23]. An additional problem with traditional Si solar cells is that the required energy payback time is on the scale of 2-3 years and, therefore, 10% of the lifetime of a Si solar module is lost; thin-film solar cells are less demanding and have the potential to achieve payback times of one year [6]. Because of these arguments, but also due to many other contributing factors, thin-film solar cells have the potential to be significantly cheaper in large-scale production. Recent studies have shown that the application of *today's technologies* in "super-large scale" manufacturing of thin-film solar cells would lead to solar electricity prices that are competitive with conventional energy sources [24].

Reproduced with permission of the copyright owner. Further reproduction prohibited without permission.

Typical $Cu(In,Ga)Se_2$ solar cells

Despite their polycrystalline nature, thin-film solar cells based on the chalcopyrite compounds of $Cu(In,Ga)Se_2$ (CIGS) achieve surprisingly high conversion efficiencies approaching 20% [25–27]. Besides the presence of grain boundaries (GBs), CIGS thin-films capable of achieving high efficiency substantially differ from single-crystals, particularly elemental semiconductors such as Si, in that they are always non-stoichiometric (Cu-poor) [25, 28], often non-uniform in Ga/(Ga+In) composition throughout the film-thickness [25], can form defect complexes that are benign to device performance [29], and in most cases require the presence of sodium during growth or sodium introduced by post-deposition treatments [30].

A typical device structure [20, 28] is shown in Fig. 2.3. CIGS solar cells are almost always designed in a substrate configuration starting from soda-lime glass, stainless steel, or polyimide material. The back contact is typically sputtered Mo and forms a non-blocking contact with CIGS. In contrast, for example, in CdTe solar cells, the back contact forms Schottky barriers and represents a major hindrance to commercialization due to stability issues [31].

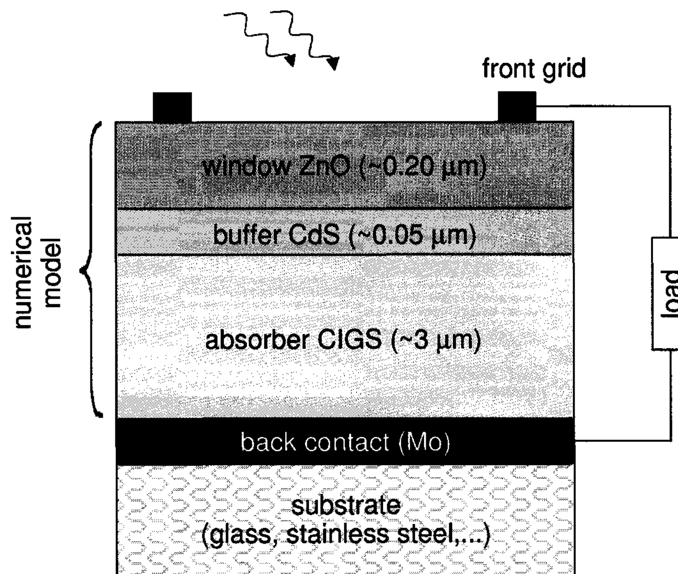

Figure 2.3: Schematic of a grid/ZnO/CdS/CIGS/Mo/glass solar cell. Only the semiconductor layers are reproduced in numerical models. The metallic contacts at the top and bottom are defined by their work function and surface recombination velocity. An external load is connected between negative (grid) and positive (Mo) electrode.

Reproduced with permission of the copyright owner. Further reproduction prohibited without permission.

The CIGS absorber material with typical thicknesses of 2–3 μm is deposited by a great variety of processes that can be roughly categorized [20, 28] into vacuum co-evaporation and two-step selenization processes. Co-evaporation deposits all elements simultaneously on a heated substrate. Intentionally or un-intentionally, gradients in the composition can be created, and Sect. 4.1 investigates whether such gradients can be beneficial to device performance. Selenization processes deposit all metals onto a film and react them in Se atmosphere to form the intended compound. The patented "three-stage" process, which makes the best CIGS solar cells to date [27], is a variation on the standard co-evaporation. The metal elemental fluxes are varied during deposition in a Se-rich atmosphere such that a favorable crystal growth under Cu-rich conditions can be combined with an overall Cu-poor composition of the finished film [25].

CdS buffer and ZnO window layers are typically deposited on top of the CIGS absorber by chemical bath deposition and RF-sputtering, respectively. A buffer layer, such as CdS, although not necessary in the concept of a heterojunction solar cell, has proven beneficial to device performance. ZnO layers are often realized in a bi-layer configuration of intrinsic and Al-doped material. A review of buffer and window layers, including an evaluation of possible alternatives, was recently conducted by Pudov [32]. The effects of the band-alignment at the CdS/CIGS interface on solar cell performance, are discussed in Sects. 4.2 and 4.3.

A cross-sectional scanning electron microscopy (SEM) image of a ZnO/CdS/CIGS solar cell is shown in Fig. 2.4. This image was taken on a sample made at the National Renewable Energy Laboratory that achieved 19.3% conversion efficiency [26]. From bottom to top: soda-lime glass, a double layer of Mo, roughly 2 μm of CIGS, 50 nm CdS (hardly visible in Fig. 2.4), and a double layer of intrinsic and doped ZnO. Noticeably, the grain sizes are comparable to the film thickness, leading to a columnar film structure. In the top part of the CIGS layer, where the electronic junction is located, the material appears nearly free of macroscopic defects, except for the columnar grain boundaries. At the beginning of the growth, at the Mo/CIGS interface, some additional GBs develop during crystallization. The effects of such horizontal and columnar grain boundaries on device performance are investigated using two-dimensional models in Chapter 5.

Broad reviews of the state-of-the-art thin-film solar cells were given in a recent special

Reproduced with permission of the copyright owner. Further reproduction prohibited without permission.

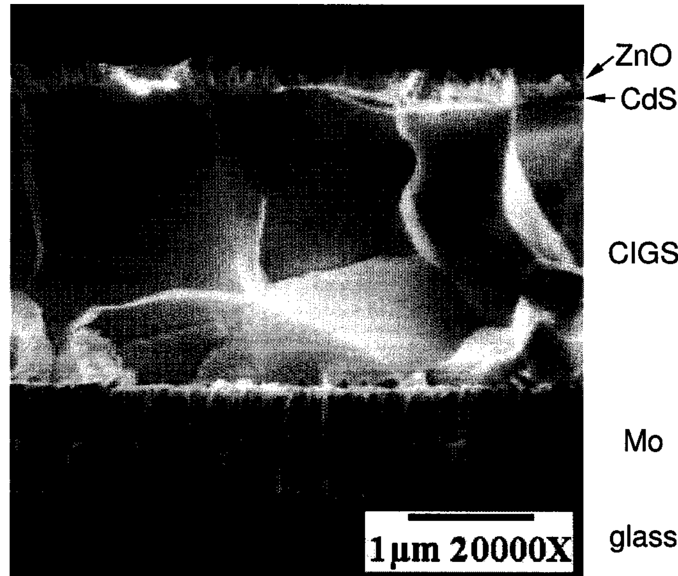

Figure 2.4: SEM image of a CIGS solar cell at 20000x magnification. In high quality material, grains extend throughout the film thickness. Image courtesy of K. Ramanathan, NREL.

edition of *Progress in Photovoltaics* [33, 34], several articles in *Photon* magazine [8, 9], and in earlier work [28]. Several chapters in Ref. [18] are devoted to the discussion of a-Si, CdTe, and CIGS thin-film solar cells.

2.2 Electrical characterization methods

In the wide range of characterization methods available for thin-film solar cells, the measurement of current-density vs. voltage (J-V) curves is of great importance, since it determines the efficiency at which the solar cell converts the sun's power into electricity. However, besides the basic characteristic of conversion efficiency, a J-V curve tells little else about the actual device. One extension of a regular J-V measurement is the measurement of the wavelength-dependent current response, typically performed at zero bias. This is referred to as the "quantum efficiency" (QE) as it, after proper normalization, represents the fraction of photons of wavelength λ that are converted into electron-hole pairs and collected as current. QE measurements under light or voltage bias, can also be misleading and careful analysis is necessary [35, 36].

Reproduced with permission of the copyright owner. Further reproduction prohibited without permission.

Numerical simulations of solar cells have the advantage that all device and material properties are well controlled as they are input parameters of the model and, therefore, evaluation of trends and quantified changes in J-V or QE measurements are possible. Although some software tools also allow the simulation of capacitance related techniques [37, 38], these characterization methods will not be addressed in this work.

2.2.1 Current-density vs. voltage

The standard J-V measurement is performed at room temperature and under a standardized "one-sun" illumination [39]. Experimentally, it is necessary to cool the solar cell during illumination, as otherwise the intense light will increase the cell's temperature. For details of the set-up used in the Photovoltaic Laboratory at Colorado State University see Refs. [40] and [32]. In short, the solar cell is subjected to a calibrated light source, two contacts are used to apply a voltage bias, and two additional contacts are used to determine the resulting cell current.

An example of a J-V curve is shown in Fig. 2.5(a) and from such a curve, the basic performance parameters can be extracted as listed in Table 2.1. Assuming that the curve follows an exponential behavior, there is redundancy in these parameters and only three (e.g., V_{oc}, J_{sc}, and η) are necessary to specify them all.

Ideally, a solar-cell J-V curve equals that of a p-n junction diode shifted by the light-generated current $J_L \simeq J_{sc}$:

$$J(V) = J_0 \left[exp\left(\frac{qV}{kT}\right) - 1\right] - J_L. \tag{2.10}$$

Table 2.1: Basic J-V performance parameters.

Parameter	Symbol	Unit	Determined by
open-circuit voltage	V_{oc}	V	$J = 0$
short-circuit current density	J_{sc}	mA/cm^2	$V = 0$
maximum-power voltage	V_{max}	V	V at $(JV)_{max}$
maximum-power current	J_{max}	mA/cm^2	J at $(JV)_{max}$
fill factor	FF	%	$(JV)_{max}/(V_{oc}J_{sc})$
efficiency	η	%	$(JV)_{max}/P_{incident}$

Reproduced with permission of the copyright owner. Further reproduction prohibited without permission.

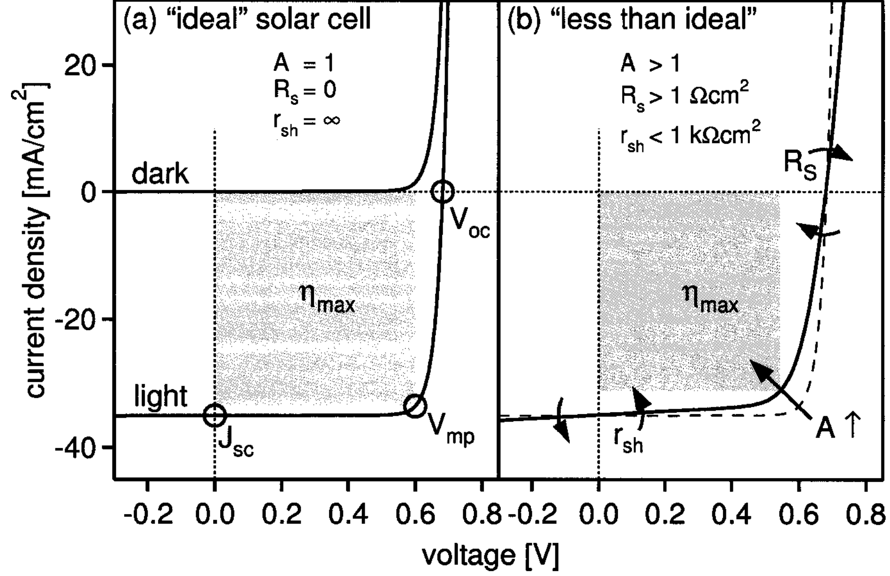

Figure 2.5: (a) Light and dark J-V curves for an ideal solar cell; standard J-V parameters that describe performance are indicated. (b) Non-ideal behavior includes parasitic resistances and a diode quality factor greater unity.

However, application of this equation to thin-film solar cells requires that parasitic losses are included [41]:

$$J(V) = J_0 \left[exp\left(\frac{q(V - R_S J)}{AkT} \right) - 1 \right] + \frac{V - R_S J}{r_{sh}} - J_L. \tag{2.11}$$

Series resistance R_S, shunt-resistance r_{sh}, and diode quality factor A describe these non-idealities. The effect of each of these parameters on the J-V curve is indicated in Fig. 2.5(b). In record-efficiency CIGS cells [27], R_S and r_{sh} effects are negligible and the best diode quality factors achieved are around 1.3. More typical values for these parameters are $R_S \sim 1$ Ωcm^2, $r_{sh} > 500$ Ωcm^2, and $A \sim 1.5$. The J-V curve analysis used in this work follows the procedure outlined by Hegedus and Shafarman [41], which includes the improved determination of the diode quality factor and series resistance suggested by Sites and Mauk [42]. The analysis process is illustrated in Fig. 2.6(a)-(d).

(a) Regular J-V plot results in V_{oc}, J_{sc}, FF, and η as given in Table 2.1.

(b) Plot of dJ/dV determines the shunt conductance, $G = 1/r_{sh}$, as shown in Fig.2.6(b).

(c) A plot of $dV/dJ = R_S + \frac{AkT}{q}(J + J_L)^{-1}$ versus $(J + J_L)^{-1}$ intercepts the y axis at a

Reproduced with permission of the copyright owner. Further reproduction prohibited without permission.

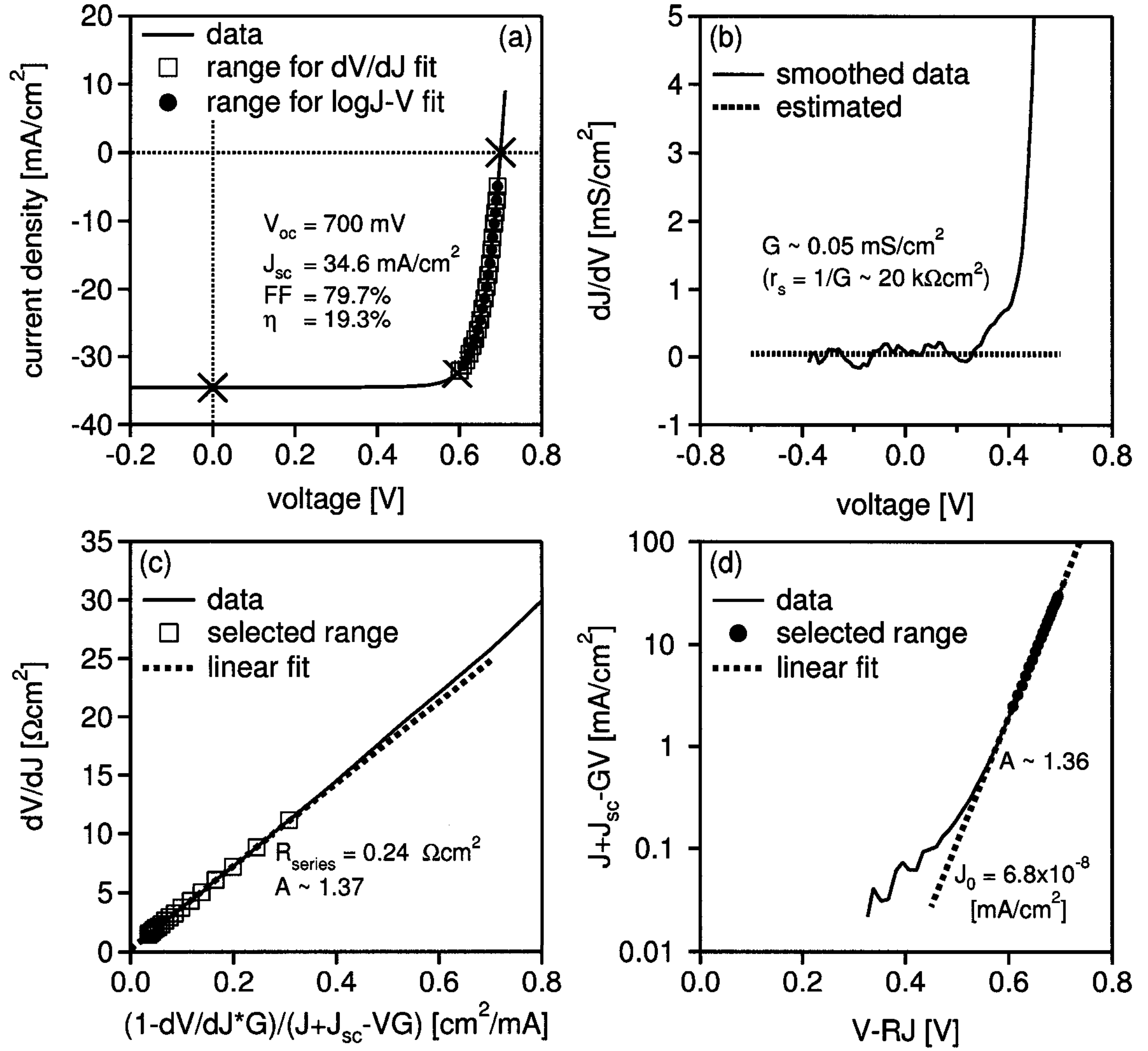

Figure 2.6: Four step analysis of J-V curves. The details of these four steps are given in the text. Data courtesy of K. Ramanathan.

value of R_S and the slope of the linear region allows identification of A.

(d) J-V plotted on a logarithmic scale, after correction for R_S and r_{sh}, allows identification of A by an alternative method. For well-behaved devices this A agrees well with the A found in step (c).

The results of the numerical simulations presented in Chapters 4 and 5 were subjected to this analysis procedure. A software application, named **Cur**rent-**V**oltage **A**nalysis (CurVA), was written that allows interactive analysis, following the above outlined steps with ease. A screen shot of this application is shown in Fig. 2.7. This program also replaced

Reproduced with permission of the copyright owner. Further reproduction prohibited without permission.

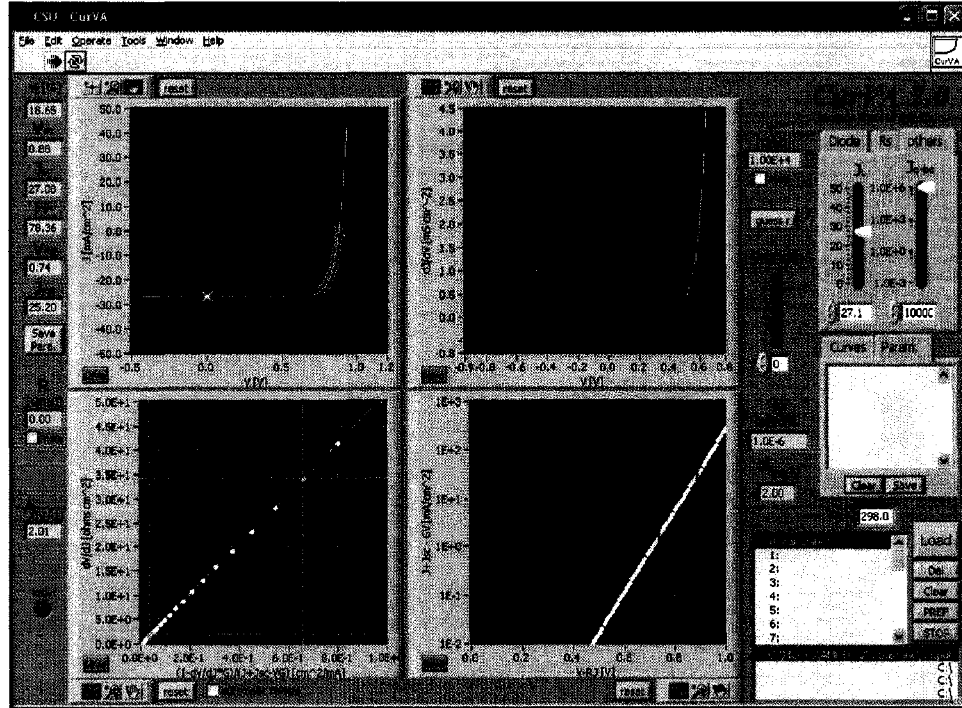

Figure 2.7: Software implementation of the four-step J-V analysis. The layout and implementation follows the discussion and figure in Ref. [41]. The analysis is performed in the four steps described above (from top left to bottom right). The evaluation ranges for the linear fits can be chosen by dragging the cursor lines in the displayed graphs, with immediate response. CurVA 2.0 includes import filters for seven different file formats and an automatic capturing of the analysis ranges. As an additional feature, CurVA can calculate arbitrary J-V curves based on the paramters J_0, A, J_L, R_S, and r_{sh}.

a previous program used in the Photovoltaic Laboratory at Colorado State University and is now in use by a number of other groups in the photovoltaic community working on CdTe, CIGS, and organic solar cells [27, 43].

2.2.2 Quantum efficiency

Measurement of the current response at zero voltage and normalization of this current to the flux density of the incoming light allows calculation of the quantum efficiency:

$$QE(\lambda) = \frac{\Delta J/q}{\Phi} = \frac{\#\text{collected electron-hole pairs}}{\#\text{incident photons}}. \tag{2.12}$$

The optical beam of total flux density Φ (units of $[\#/\text{cm}^2\text{s}]$) is monochromatic, but its peak wavelength varies over the spectral range that is relevant to the solar cell application.

Reproduced with permission of the copyright owner. Further reproduction prohibited without permission.

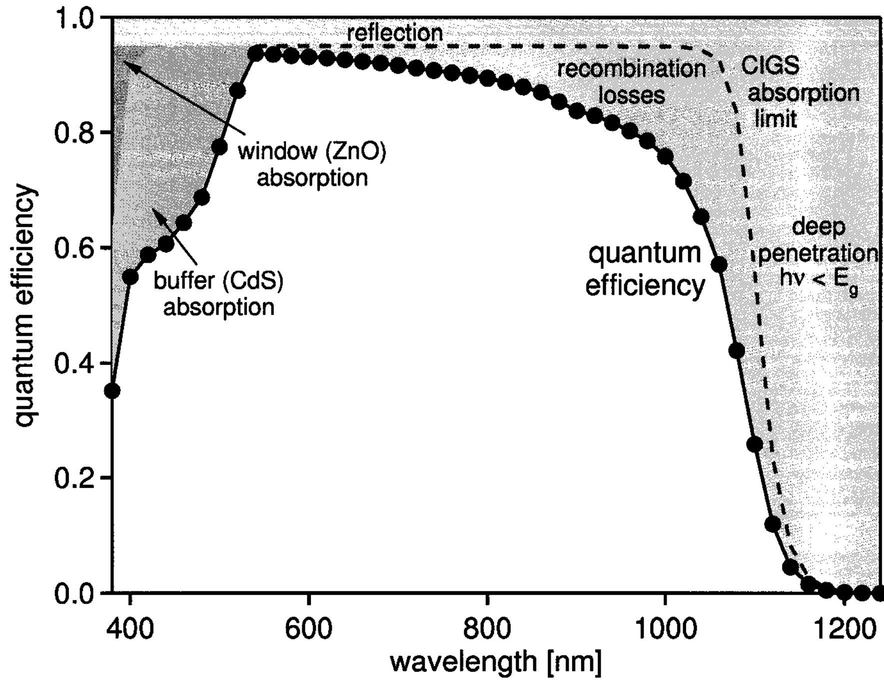

Figure 2.8: Example of a quantum-efficiency curve and involved loss mechanisms.

Experimentally, the beam intensity also varies as it scans through all wavelengths; typically, in numerical simulations $\Phi = 10^{15}$ cm^{-2}s^{-1} is used. More details on the experimental set-up are given elsewhere [32, 40]. Eq. 2.12 can be integrated to express the relation between the short-circuit current density and QE,

$$J_{sc} = q \int_{\lambda} F(\lambda) \cdot QE(\lambda) \mathrm{d}\lambda, \tag{2.13}$$

where F is the flux density per unit wavelength (units of [#/cm^{2}nm·s]).

An example QE curve is shown in Fig. 2.8. This is the result of a simulation, and, hence, a somewhat idealized case, but the differences from experimental QE curves will be addressed in the following:

- "Reflection" losses are introduced by partial coverage of the front surface by non-transparent contacts (i.e., metal contact fingers) or by reflection at material interfaces. Experimentally, these losses are minimized by the application of anti-reflective coatings.

Reproduced with permission of the copyright owner. Further reproduction prohibited without permission.

- "Window" absorption in the short-wavelength region is negligible due to the high band-gap energy of this material. Free electron absorption in the ZnO layer can lower the quantum efficiency in the high wavelength region, but this effect is typically small and neglected in the numerical simulations.

- "Buffer" absorption represents one of the major losses in today's CIGS and CdTe thin-film solar cells. Thinning of the CdS or replacing it with a higher band-gap material are possible alternatives.

- "Recombination" losses are introduced by less-than-ideal collection efficiencies of photo-generated carriers. The longer the wavelength, the deeper the generation of carriers, and the higher the likelihood of recombination. This will be investigated in some detail in Sect. 5.3.4.

- "Deep penetration" of carriers. These losses are inherent to every semiconductor as light with photon energy of $h\nu < E_g$ is not absorbed.

The resulting QE curve in Fig. 2.8 is similar to QE curves observed in CIGS solar cells of good efficiency [41].

Reproduced with permission of the copyright owner. Further reproduction prohibited without permission.

Chapter 3

Basics of numerical simulations

This chapter introduces the concept of numerical simulations of semiconductors, particularly in solar-cell applications, and discusses the relevant physical models for transport, recombination, and generation. Subsequently, baseline parameter sets are presented that describe CIGS and CdTe thin-film solar cells; their characteristics are chosen to be similar to CIGS and CdTe record cells. These baselines are used as a starting point for more complex models. Although this work only discusses CIGS solar cells, the CdTe baseline case has also been applied in a number of studies [36, 44]. The chapter ends with a brief description of the software packages used in this work.

3.1 Governing equations

The device physics problem is presented in the form of the Poisson and the electron- and hole-continuity equations [15]:

$$\nabla \cdot \epsilon \nabla \phi = -q\,(p - n + N_{D^+} - N_{A^-})\,, \tag{3.1}$$

$$\nabla \cdot \vec{J}_n = q\,(R - G) + q\frac{\partial n}{\partial t}, \tag{3.2}$$

and

$$-\nabla \cdot \vec{J}_p = q\,(R - G) + q\frac{\partial p}{\partial t}, \tag{3.3}$$

Reproduced with permission of the copyright owner. Further reproduction prohibited without permission.

where ϵ is the dielectric constant, ϕ is the electrostatic potential, n and p are the free carrier concentrations, N_{D^+} and N_{A^-} are the density of ionized donor and acceptor levels, J_n and J_p are the electron and hole current density, R is the recombination rate, and G is the generation rate. In this work, only steady state solutions are investigated and, hence,

$$\frac{\partial n}{\partial t} = 0 \quad \text{and} \quad \frac{\partial p}{\partial t} = 0. \tag{3.4}$$

The recombination terms in Eqn. 3.2 and 3.3 have non-linear dependencies on the carrier concentrations n and p. Hence, Eqn. 3.1–3.3 represent a set of coupled non-linear differential equations, which will be solved by numerical methods with the typical approach: (1) discretization ("meshing") of the device, (2) discretization of Eqn. 3.1–3.3, (3) application of boundary conditions (contacts), and (4) solution of the resulting matrix equation by iteration. The solution consists of the three state variables ϕ, E_{fn}, and E_{fp}, which are sufficient to deduce all other characteristics in steady state conditions. All simulations utilize Fermi-Dirac statistics.

3.1.1 Transport

In the absence of magnetic fields and temperature gradients, carrier transport in semiconductors occurs by drift and diffusion only and can be expressed by the equations

$$J_n = q\mu_n n\mathcal{E} + qD_n \nabla n \tag{3.5}$$

and

$$J_p = q\mu_p p\mathcal{E} - qD_p \nabla p, \tag{3.6}$$

where the μ's are the carrier mobilities, the D's are the carrier diffusion constants, and $\mathcal{E}$ is the electrostatic field [15]. With the definition of quasi-Fermi levels, E_{fn} and E_{fp} (Eq. 2.7), and quasi-Fermi potentials, $\phi_{fn} = -(E_{fn}/q)$ and $\phi_{fp} = (E_{fp}/q)$, this can be simplified to

$$J_n = -q\mu_n n \nabla \phi_{fn} \tag{3.7}$$

and

$$J_p = -q\mu_p p \nabla \phi_{fp}. \tag{3.8}$$

Reproduced with permission of the copyright owner. Further reproduction prohibited without permission.

These equations applied to the solution found based on Eqn. 3.1–3.3 describe transport due to electric fields, diffusion, and effective fields (e.g., band-gap gradings or variations in N_C and N_V).

3.1.2 Generation

Optical generation in this work assumes wavelength-independent reflection at front, R_F, and back surfaces, R_B. The photon flux density, Φ, decays exponentially vs. depth, $\Phi(z) = \Phi(z_0) \cdot exp\,(-\alpha_x(z - z_0))$, where Φ is the flux density in units of (#photons/cm^{2}s), and α_x is the absorption constant, and the subscript x stands for ZnO, CdS, or CIGS. Hence, the generation rate $G(z)$ equals:

$$G(z) = -\frac{\mathrm{d}\Phi}{\mathrm{d}z} = \alpha_x \cdot \Phi(z_0) \cdot exp\,(-\alpha_x(z - z_0))\,. \tag{3.9}$$

This equation applies in all layers under consideration of the appropriate $\Phi(z_0)$ and z_0, given in Table 3.1. The situation becomes more complex if the band-gap energy, and therefore the absorption spectra, is spatially non-uniform as it will be discussed in Sect. 4.1. Back reflection implies that a fraction of the light that reaches the back contact, $R_B < 1$, reverses its propagation direction at the back contact and is then incident on the device "from the back." If W_{CIGS} is the CIGS absorber thickness, the intensity of the reflected light is $\Phi_{reflected} = R_B \cdot \Phi(W_{CIGS})$.

Equation 3.9 describes generation due to a monochromatic light source. In practice, a spectrum of light is incident and the simulation assumes a standard "one-sun" illumination, also referred to by "AM1.5" [39]. The total generation profile is the sum of

Table 3.1: Parameters describing photogeneration in a ZnO/CdS/CIGS solar cell. Throughout this work, $z = -0.25$ μm is the front-contact surface, $z = -0.05$ μm the ZnO/CdS interface, and $z = 0$ the CdS/CIGS interface, hence, points in the window and buffer layers have $z < 0$ and the absorber is at $z > 0$.

layer	$\Phi(z_0)$	z_0
ZnO	$\Phi_0(1 - R_F)$	-0.25 μm
CdS	$\Phi_0(1 - R_F) \cdot exp\,(-\alpha_{ZnO} \cdot 0.2\ \mu\text{m})$	-0.05 μm
CIGS	$\Phi_0(1 - R_F) \cdot exp\,(-\alpha_{ZnO} \cdot 0.2\ \mu\text{m}) \cdot exp\,(-\alpha_{CdS} \cdot 0.05\ \mu\text{m})$	0 μm

Reproduced with permission of the copyright owner. Further reproduction prohibited without permission.

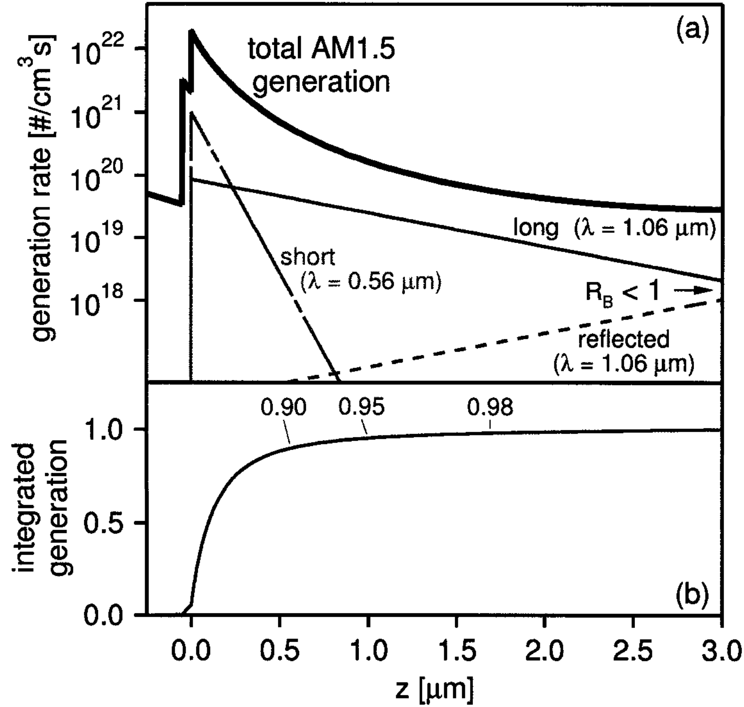

Figure 3.1: (a) Calculated total generation in a ZnO/CdS/CIGS solar cell. Shorter wavelengths experience stronger absorption. For photon energies approaching the CIGS bandgap energy, the generation is lower and more uniform in the device. Only weakly absorbed light experiences back reflection. (b) Integrated and normalized generation.

the single-wavelength generations. Figure 3.1(a) illustrates generation by long and short wavelength light, as well as the total generation due to the one-sun illumination (spectral data is tabulated in Appendix A). Short wavelength light ($\lambda = 0.56$ μm) is strongly absorbed and, hence, there is no significant generation deeper 0.5 μm. Long wavelength light ($\lambda = 1.06$ μm), which has a significantly smaller α, shows absorption deeper in the device, and some non-negligible fraction can be reflected from the back surface (also in Fig. 3.1[a]). This becomes increasingly more interesting as devices are made thinner to reduce processing times and material usage. The integrated generation, Fig. 3.1(b), shows that 95% of the sunlight's absorption occurs within the first micrometer of the CIGS material.

3.1.3 Recombination

Defect related recombination is typically described by the model developed and verified by Shockley, Read, and Hall (SRH) [45, 46]. This model resulted from statistical considerations

Reproduced with permission of the copyright owner. Further reproduction prohibited without permission.

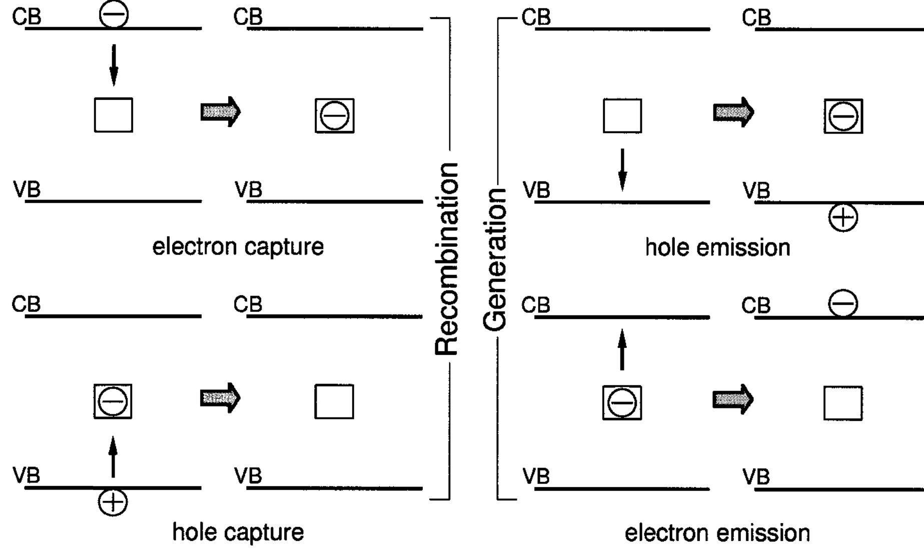

Figure 3.2: The four allowed transitions in the Shockley-Read-Hall model. Capture processes depend on the free carrier concentration and the concentration of available trap levels. Emission processes only depend on the trap occupancy and not on the free carrier concentration.

of transition rates and required only one assumption, namely that a defect level has only two states of existence, i.e., an acceptor level is either neutral or negatively charged. With this restriction, four transitions are possible for each defect, shown for the case of acceptor traps in Fig. 3.2 (similar diagrams apply to donor traps). Electron capture followed by hole capture leads to a recombination process, whereas, hole emission followed by electron emission leads to generation of an electron-hole pair. In equilibrium, both these processes occur at equal rates. Under optical or electrical injection, however, the capture rates increase linearly with the free carrier concentrations and, therefore, additional recombination occurs. Carrier emission rates are unaffected by the free carrier concentrations unless the material is degenerate [45, 47].

The rate of recombination can be written as

$$R = \frac{\sigma_e \sigma_h v_{th} N_t \left(np - n_i^2\right)}{\sigma_n \left(n + n_i exp\left[\left(E_t - E_i\right)/kT\right]\right) + \sigma_p \left(p + n_i exp\left[\left(E_i - E_t\right)/kT\right]\right)} \tag{3.10}$$

which is often simplified by the definition of lifetime parameters, $\tau_e = \left(N_t v_{th} \sigma_e\right)^{-1}$ and $\tau_h = \left(N_t v_{th} \sigma_h\right)^{-1}$, and $p_1 = n_i exp\left[\left(E_i - E_t\right)/kT\right]$ and $n_1 = n_i exp\left[\left(E_t - E_i\right)/kT\right]$ to the

Reproduced with permission of the copyright owner. Further reproduction prohibited without permission.

more traditional form [15, 17, 47]

$$R = \frac{(np - n_i^2)}{\tau_h (n + n_1) + \tau_e (p + p_1)}. \tag{3.11}$$

This equation further simplifies in the quasi-neutral region of a doped semiconductor where either $n \gg p, n_1, p_1$ or $p \gg n, n_1, p_1$. Under these conditions, the minority carrier recombination rate in n- or p-type material becomes

$$R_{n-type} = \frac{\Delta p}{\tau_h} \quad \text{and} \quad R_{p-type} = \frac{\Delta n}{\tau_e}, \tag{3.12}$$

where Δn and Δp are the excess minority carrier concentrations.

Similarly, recombination at interfaces, such as the front or back contact of the solar cell, at material interfaces, or at grain boundaries, may be described by

$$R_s = \frac{(np - n_i^2)}{(n + n_1)/S_h + (p + p_1)/S_e}, \tag{3.13}$$

where $S_h = N_t v_{th} \sigma_h$ and $S_e = N_t v_{th} \sigma_e$ are the interface or grain-boundary recombination velocities for holes and electrons in units of (cm/s).

Other recombination processes such as band-to-band recombination or Auger recombination can also be considered [48, 49], but they are insignificant compared to SRH recombination in polycrystalline material.

3.2 Baseline parameters

Numerical modeling of polycrystalline thin-film solar cells is an important strategy to test the viability of proposed physical explanations and to predict the effects of physical changes on cell performance. In general, this must be done with only partial knowledge of input parameters. Guidelines that should be considered when assigning input parameters for numerical models are discussed below, and subsequently, specific baseline parameters for CIGS and CdTe are proposed. All work reported in Chapter 4 and 5 have the CIGS baseline case as a common starting point, although the calculations in the different sections were

Reproduced with permission of the copyright owner. Further reproduction prohibited without permission.

performed on different platforms and with different aspects in mind. The CdTe case is not discussed any further in this work, but was used for studies reported in Refs. [36] and [44].

Simulations vs. data fitting

Input parameter sets used to fit experimental J-V data are in general not unique. Fitting of experimental data is only conclusive, if a wider set of data, e.g., J-V at different temperatures or QE at different biases, is used. Input parameters that are well-known should not be changed at any time (not be abused as a "fitting parameter"), whereas parameters that have only marginal effects on the output can be tested and then not changed. After excluding these parameters, the remaining parameters are available for fitting purposes. Only results reported in Sect. 4.3 attempted to match experimental data, whereas all other results reported here were used to identify general principles and to evaluate their effects on device performance, independent of particular experimental results.

Front and back contacts

In general, contacts can be assumed ohmic or, depending on the focus of the modeling, assigned a Schottky barrier height consistent with experimental observations. The reflection at the back surface has only minor influence on the achievable short-circuit current density (J_{sc}) and this influence only becomes noticeable if the absorber is chosen to be fairly thin. Typical simulation tools support a constant multiplicative reflection factor for the front surface (i.e., $R_F = 0.1$, 10% reflection), which reduces the quantum efficiency by this fraction. Neglecting interference effects, QE curves show a fairly flat response of $\sim(1 - R_F)$ at intermediate wavelengths.

Surface recombination velocities at the front and back contact are chosen to be equal to the thermal velocity. This effectively recombines every minority carrier that reaches the contacts and establishes either a perfect ohmic or a Schottky contact depending on the barrier height parameter [15, 49].

Reproduced with permission of the copyright owner. Further reproduction prohibited without permission.

Material parameters

Carrier mobilities for polycrystalline material are chosen lower than the values reported for crystalline material. Effective masses of $m_e^* = 0.2m_0$ for electrons and $m_h^* = 0.8m_0$ for holes, which are numbers typical for direct-band-gap material, are used unless more specific data is available. The ratio of the carrier mobilities, μ_e/μ_h, should be approximately inversely proportional to the ratio of the effective masses, m_e^*/m_h^*. The effective densities of states, N_C and N_V, can be calculated using Eq. 2.5. The direct temperature dependence in N_C and N_V is taken into account for temperature-dependent modeling.

Carrier concentrations can be experimentally determined from capacitance-voltage analysis; recent work, however, suggests that such measurements may overestimate the free carrier concentrations [37]. Typical concentrations are the order of 10^{16} cm^{-3} for CIGS and 10^{14} cm^{-3} for CdTe. The band-gap energies of the semiconductors are known as determined from quantum-efficiency (QE) or absorption measurements. The choice of band offsets at interfaces is discussed in the specific material sections below.

Defects

Unless details can be generally assumed for an entire class of materials or device specific simulations are intended, it is recommended that recombination defect states be assigned to a narrow distribution close to the middle of the band gap (generic mid-gap states). In the SRH formalism (Sect. 3.1.3), a defect state can change its state of charge only by one elementary charge. Therefore, one can always make the following distinction: A donor-like (acceptor-like) defect state is able to donate (accept) one electron. The two possible charge states for donors (acceptors) are positive and neutral (negative and neutral). It follows that free electrons (holes) will be coulomb-attracted to ionized donor-like (acceptor-like) defect states, whereas holes (electrons) will have no strong interaction with the donor-like (acceptor-like) defects, giving very small hole (electron) cross-sections. Attractive cross-sections are assigned corresponding to a radius at which the coulomb potential energy of

Reproduced with permission of the copyright owner. Further reproduction prohibited without permission.

the carrier in the field of the charged trap equals kT [17]:

$$\sigma_{attractive} = \frac{q^4}{16\pi\epsilon^2 k^2 T^2} \approx 10^{-13} - 10^{-12}\ \text{cm}^2. \tag{3.14}$$

Neutral cross-sections are estimated to be between 10^{-18} and 10^{-15} cm^2. The latter number corresponds to the physical size of an atom and is often referred to as "geometric" cross-section. Smaller values may be reasonable if transitions are unlikely, or to compensate for strong field effects in the region of interest.

3.2.1 ZnO/CdS/Cu(In,Ga)Se_2 solar cells

Three layers: n-ZnO transparent contact, n-CdS window, and p-CIGS absorber. This configuration resembles the most common CIGS devices (see discussion in Sect. 2.1.4). Baseline case parameters are listed in Table 3.2.

The band alignment at the interface of CdS and 1.15 eV-CIGS is chosen to be Type I ($|\Delta E_C|$ and $|\Delta E_V|$ are both smaller than the band-gap difference) with ΔE_C = +0.3 eV, which was guided by experimental [50, 51] and theoretical studies [52]. The ZnO-CdS interface is assumed as Type II with ΔE_C = -0.2 eV, which is in the mid-range of experimental results [50, 53] and close to the predictions from first-principles calculations [54].

A single deep acceptor (donor) trap is used for the CdS (CIGS) layer. The high defect density in the CdS layer, similar to the density of shallow donors, is necessary to generate the often observed photoconductivity, which is discussed in Sect. 4.3. The mobilities assigned are approximately a factor of 2–3 below crystalline material values [55, 56]; the hole mobility is at the high end of what has been recently measured in thin-film CIGS at low T, μ_h = 3–22 cm^2/Vs [57]. Default values of $0.2m_0$ and $0.8m_0$ are used for the electron and hole effective masses in all layers, which is similar to what is generally reported in the literature for CIS [20]. Dielectric constants are assigned mid-range values of what has been reported [20, 55]. Absorption is defined based on measurements on polycrystalline CdS [58] and CIGS [59] material. The tabulated spectral data used in the simulations is listed in Appendix A.

Except for the band alignments, device performance is essentially independent of ZnO and only weakly dependent on CdS parameters. Changes in the CIGS parameters are

Reproduced with permission of the copyright owner. Further reproduction prohibited without permission.

Table 3.2: CIGS baseline case input parameters. Barrier heights $\Phi_{bn} = E_C - E_f$ and $\Phi_{bp} = E_f - E_V$; surface recombination velocity S; layer width W; dielectric constant ϵ; mobility μ; shallow dopant density N_D and N_A; band-gap energy E_g; effective density of states N_C and N_V; conduction-band offset between two adjacent layers ΔE_C; acceptor or donor defect density N_{DG} and N_{AG}; defect peak energy E_A and E_D; defect distribution width W_G; and capture cross section σ. The subscript e/h refers to electron/hole properties.

A. General device properties		Front	Back
Φ_b (eV)		$\Phi_{bn} = 0$	$\Phi_{bp} = 0.2$
S_e (cm/s)		10^7	10^7
S_h (cm/s)		10^7	10^7
Reflectivity		0.05	0.8
B. Layer properties	**ZnO**	**CdS**	**CIGS**
W (nm)	200	50	3000
ϵ/ϵ_0	9	10	13.6
μ_e (cm^2/Vs)	100	100	100
μ_h (cm^2/Vs)	25	25	25
$N_{D/A}$ (cm^{-3})	N_D: 10^{18}	N_D: 1.1×10^{18}	N_A: 2×10^{16}
E_g (eV)	3.3	2.4	1.15
N_C (cm^{-3})	2.2×10^{18}	2.2×10^{18}	2.2×10^{18}
N_V (cm^{-3})	1.8×10^{19}	1.8×10^{19}	1.8×10^{19}
ΔE_C (eV)	-0.2 (ZnO/CdS)	+0.3 (CdS/CIGS)	
C. Gaussian-distributed defect states	**ZnO**	**CdS**	**CIGS**
N_{DG}, N_{AG} (cm^{-3})	D: 10^{17}	A: 10^{18}	D: 10^{14}
E_A, E_D (eV)	mid-gap	mid-gap	mid-gap
W_G (eV)	0.1	0.1	0.1
σ_e (cm^2)	10^{-12}	10^{-17}	5×10^{-13}
σ_h (cm^2)	10^{-15}	10^{-12}	10^{-15}

observed to correlate well with a basic diode model. These dependences have been investigated in Ref. [60].

3.2.2 SnO_2/CdS/CdTe solar cells

Three layers: n-SnO_2 transparent conducting oxide, n-CdS window, and p-CdTe absorber. Baseline case parameters are listed in Table 3.3.

The conduction bands at the SnO_2/CdS interface are aligned in agreement with experiments [53, 61]. The offset at the CdS/CdTe interface is assumed to be Type II with $\Delta E_C =$ –0.1 eV, which was calculated from first-principles [54, 62] and confirmed by photo-electron

Reproduced with permission of the copyright owner. Further reproduction prohibited without permission.

Table 3.3: CdTe baseline case input parameters. Description of symbols is given in the caption to Table 3.2.

A. General device properties		Front	Back
Φ_b (eV)		$\Phi_{bn} = 0.1$	$\Phi_{bp} = 0.4$
S_e (cm/s)		10^7	10^7
S_h (cm/s)		10^7	10^7
Reflectivity		0.1	0.8
B. Layer properties	**SnO_2**	**CdS**	**CdTe**
W (nm)	500	25	4000
ϵ/ϵ_0	9	10	9.4
μ_e (cm^2/Vs)	100	100	320
μ_h (cm^2/Vs)	25	25	40
$N_{D/A}$ (cm^{-3})	N_D: 10^{17}	N_D: 1.1×10^{18}	N_A: 2×10^{14}
E_g (eV)	3.6	2.4	1.5
N_C (cm^{-3})	2.2×10^{18}	2.2×10^{18}	8×10^{17}
N_V (cm^{-3})	1.8×10^{19}	1.8×10^{19}	1.8×10^{19}
ΔE_C (eV)		0	-0.1
C. Gaussian-distributed defect states	**SnO_2**	**CdS**	**CdTe**
N_{DG}, N_{AG} (cm^{-3})	D: 10^{15}	A: 10^{18}	D: 2×10^{14}
E_A, E_D (eV)	mid-gap	mid-gap	mid-gap
W_G (eV)	0.1	0.1	0.1
σ_e (cm^2)	10^{-12}	10^{-17}	10^{-12}
σ_h (cm^2)	10^{-15}	10^{-12}	10^{-15}

spectroscopy results [63]. The back-contact is chosen as a moderate Schottky barrier, which is the standard interpretation of the frequently observed "roll-over" effect in CdTe solar cells [64, 65].

For SnO_2 and CdS, default values of effective masses, $0.2m_0$ and $0.8m_0$, are used. The model shows only weak dependences on CdS parameters, except for layer thickness. The absorption curves used were measured on polycrystalline CdS and CdTe material [58]. CdTe mobilities are assumed approximately half of the crystalline values [55] and the effective masses are estimated as an average from several published sources [66–68]. A single deep acceptor (donor) trap is used for the CdS (CdTe) layer. Due to the low carrier concentration in the CdTe, the device is relatively depleted at zero bias and this causes a noticeable change in the band diagram by photogenerated carriers. This type of band deformation can lead to non-superposition of light and dark J-V curves [69]. Another possible contribution to

Reproduced with permission of the copyright owner. Further reproduction prohibited without permission.

non-superposition is the field-aided collection of photogenerated carriers [41]. Hence, in CdTe non-superposition is likely caused within the absorber layer, whereas in CIGS devices it is dominantly created in the CdS layer (Sect. 4.3).

Results of the baseline cases

The models described above were established in several different simulation environments, and although there are minor differences in the way parameters are defined in different software packages, the solutions to the baseline problems agree very well. Other researchers have had similar experiences [70]. The *J*-*V* and QE results for the CIGS and CdTe baselines are shown in Fig. 3.3.

The higher band-gap in CdTe solar cells allows for higher open-circuit voltage, but also results in lower current. Both quantum efficiency curves show some losses due to CdS absorption in the low wavelength region, $\lambda < 520$ nm. CdTe solar cells with their low doping and, hence, wide space-charge region achieve generally better collection than CIGS devices. In CIGS, the longer wavelength generation occurs far from the SCR edge, and the QE is lowered for these wavelengths. The baseline cases are very similar in their

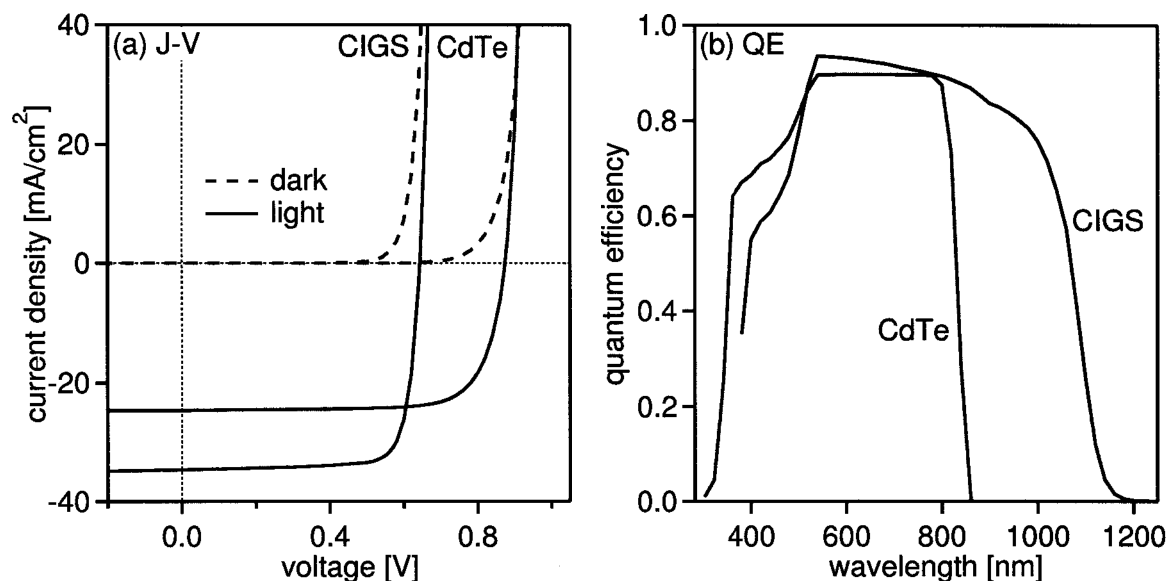

Figure 3.3: Simulation results for the CIGS and CdTe baseline cases. (a) *J*-*V* in the dark and under one-sun illumination. (b) The QE was calculated under standard illumination.

Reproduced with permission of the copyright owner. Further reproduction prohibited without permission.

Table 3.4: Performance parameters of the simulated baseline cases and the experimental CIGS and CdTe record cells after Refs. [27] and [19].

Sample	V_{oc} (V)	J_{sc} (mA/cm^2)	FF (%)	η (%)
CIGS baseline	0.64	34.6	79.5	17.7
CIGS record	0.69	35.2	79.9	19.5
CdTe baseline	0.87	24.6	76	16.4
CdTe record	0.85	25.9	75.5	16.5

layer structure and performance to record solar-cell devices; this is shown in Table 3.4, which lists J-V parameters for these cases. The baselines were intentionally "aligned" in performance to record levels. This allows to establish a well-behaved baseline case in comparison to a well-studied record device and then add other detrimental effects, such as additional recombination or grain boundaries. The experimental CIGS efficiency exceeds the simulated baseline case and some of the difference can be attributed to a "graded" band-gap absorber, Sect. 4.1 will discuss this in detail.

A band picture of the ZnO/CdS/CIGS baseline is shown in Fig. 3.4 at zero bias and under forward bias. The one-sun illumination introduces a splitting of the quasi-Fermi

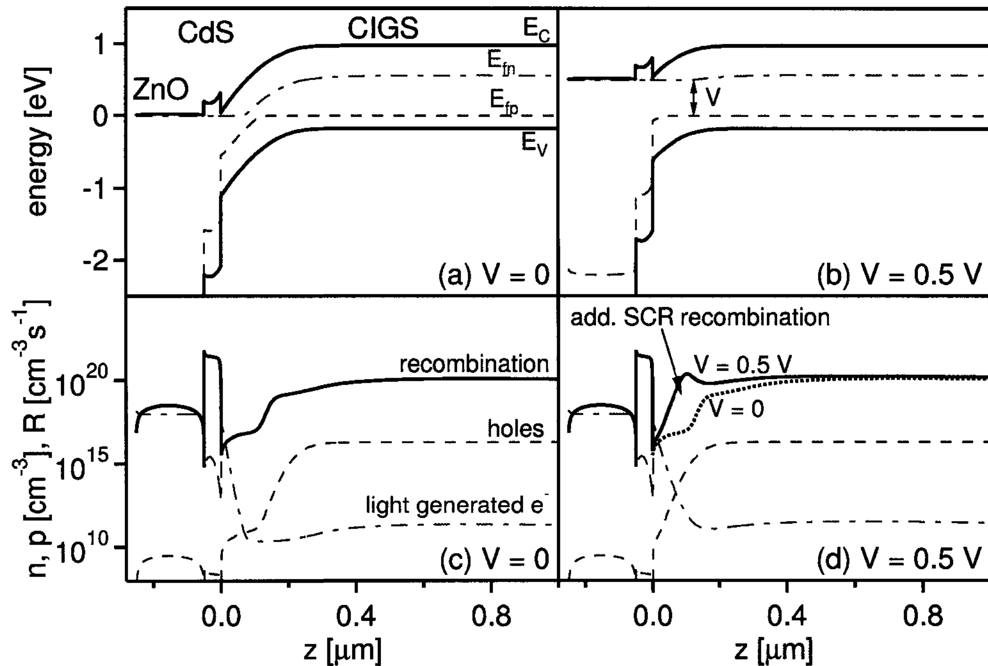

Figure 3.4: Bands (top) and carrier concentrations and recombination profile (bottom) for the CIGS baseline case at zero (left) and forward bias (right). One-sun illumination.

Reproduced with permission of the copyright owner. Further reproduction prohibited without permission.

levels in the bulk of the CIGS absorber of approximately 0.56 eV, slightly less in magnitude than the observed open-circuit voltage (Fig. 3.4[a]). The density of light-generated excess minority electrons is the order of 10^{11} cm^{-3}. Under forward bias (Fig. 3.4[b]), the quasi-Fermi levels close to and within the SCR are split by the applied bias V, and this increased density of free electrons and holes, and the fact that they are present in similar concentration, maximizes recombination in this area. The dotted line in Fig. 3.4[d] shows the recombination at zero bias in comparison.

3.3 Software

Simulations of thin-film solar cells have become increasingly mature and complex over the last two decades. A number of simulation packages have been developed at universities or research institutes, and these are typically available at no cost and without support. This group of programs includes AMPS-1D, SCAPS-1D, SimWindows, PC-1D, ADEPT-F, ASA, ASPIN, or AFORS-HET. All of these are one-dimensional and can be used to directly or indirectly evaluate solar-cell performance. Some also incorporate other experiments such as capacitance related characterization (SCAPS-1D, ASA, AFORS-HET). AMPS-1D, SCAPS-1D, ASA, and PC-1D were compared in a recent review article by Burgelman et al. [70]. The extension into two or three dimensions, which allows to simulate lateral fluctuations in polycrystalline thin-film solar cells (e.g., grain boundaries), is more difficult to achieve and remains in the domain of commercial software packages, such as APSYS, ATLAS 2D, DESSIS, or Medici. A subset of these programs have been used for the work presented here and their capabilities and limitations will be briefly reviewed.

3.3.1 AMPS-1D

AMPS-1D, an acronym for "**A**nalysis of **M**icroelectronic and **P**hotonic **S**tructures," was developed under the guidance of Stephen J. Fonash at the Pennsylvania State University with support of the Electric Power Research Institute. AMPS-1D is known for its stability and user friendliness; no updates have been made since the beta release of version 1.0 in 1997. Some of the key advantages and disadvantages are listed below.

Reproduced with permission of the copyright owner. Further reproduction prohibited without permission.

Key features of AMPS-1D

PROs	CONs
• allows batch processing of simulations • very stable in general; complex devices can introduce some instabilities • good user interface, including a flexible plotting program • well-documented user manual	• limited to 400 mesh points and 30 layers; a version that supports 2000 mesh points is available upon request • no treatment of interfaces, requires definition of "interfacial layers" • must enter *all* information by hand (can not read, e.g., spectral files) • binary case files can only be read in AMPS-1D (no manipulation of text files possible)

AMPS-1D was used for earlier work on CdTe solar cells that is not reported in this work [36, 44] and for the results presented in Sects. 4.1 and 4.3.

3.3.2 SCAPS-1D

SCAPS-1D, an acronym for "**S**olar Cell **Cap**acitance **S**imulator in 1 Dimension," was developed at the University of Ghent under Marc Burgelman [38, 70]. It is continuously updated and the progress is well documented in the literature (update to version 2.3, see Ref. [71]). In the latest release, version 2.4, SCAPS-1D remains to be a very fast and versatile utility

Key features of SCAPS-1D

PROs	CONs
• all input files are user-accessible text files, this includes spectral data as well as device definition files • sophisticated treatment of interface recombination and interface trapping • very fast • inclusion of series resistance, capacitance-voltage and capacitance-frequency response	• can be unstable when the device is far from ideal and includes secondary barriers • no batch processing, every calculation (J-V, QE, etc.) of every model has to be performed "by hand" • inflexible plotting utility is of little use

Reproduced with permission of the copyright owner. Further reproduction prohibited without permission.

that has some advantages on the device physics side, however, stability and batch processing are still missing which makes it a tedious tool for comprehensive studies. SCAPS-1D was used for the studies that made intensive use of the interface feature, reported in Sect. 4.2.

3.3.3 ISE-TCAD (DESSIS)

Integrated Systems Engineering (ISE), recently acquired by Synopsis Inc., offers a comprehensive simulation solution. The entire software package is referred to as "ISE-TCAD" and licensed on a modular basis to the end user. At the heart of the device simulations is the code DESSIS, which is a *"... multidimensional, electrothermal, mixed-mode device and circuit simulator for one-, two-, and three-dimensional semiconductor devices"* [48]. This software was made available through a collaboration with the Measurement and Characterization Division at the National Renewable Energy Laboratory.

Extending simulations into two or three dimensions does not only require substantially higher computing power, but also requires more sophisticated model definition, meshing, material definition, solution algorithms, and plotting capabilities. In ISE-TCAD, these functions are separated into different applications, to name only the ones most relevant to this work:

GENESISe — The "host" of the application suite, manages projects, and ties all other applications together by organizing data transfer between individual components. Simulation "experiments" can include hundreds of individual calculations.

MDRAW — Graphical drawing programs in which the user specifies geometry, material associations, and mesh details.

DESSIS — Performs the calculations. Supports many physical models specific to Si and III-V semiconductors. Defect distributions, interface definitions, illumination spectrum, etc., are all input to this calculation.

Tecplot-ISE — Plotting utility that allows two- and three-dimensional analysis of the results and the creation of cuts, contour plots, vector plots, etc.

Reproduced with permission of the copyright owner. Further reproduction prohibited without permission.

ISE-TCAD is completely independent of particular applications, e.g., solar cells, which makes it extremely versatile, but also very difficult to get started with. The device definition file, called the "command file" in DESSIS lingo, specifies the physical models that should be applied, the boundary conditions, the details of what is calculated, the details of the numerical procedure, and much more. ISE-TCAD was used for the work described in Chapter 5.

Key features of ISE-TCAD

PROs	CONs
• two-dimensional (in the configuration used) • extremely comprehensive and flexible • excellent batch and queue capabilities, including distributed computing • very comprehensive documentation	• difficult to get started, establishing a "first model" is a significant challenge • no built-in support for solar-cell application • expensive

Reproduced with permission of the copyright owner. Further reproduction prohibited without permission.

Chapter 4

One-dimensional simulations: absorber grading, heterojunction interface, and photoconductive buffer layer

A great number of questions relating to CIGS solar cells can be effectively addressed by one-dimensional simulations even without specific knowledge of their polycrystalline nature. The inclusion of grain boundaries is, depending on the GB characteristics, not likely to substantially change the qualitative or quantitative results. In fact, one of the primary conclusions of Chapter 5 is that strongly charged GBs are unlikely to be present in highly-efficient cells and this alleviates most of the impact that GBs could have on the one-dimensional results. More specific evidence supporting this approach is given in Chapter 5.

This chapter discusses the three most important regions of a CIGS solar cell. First, the absorber layer is discussed and in particular the effects of compositional variations on device performance is analyzed. Second, the CdS/CIGS material interface is studied, and it is shown that interfacial recombination can explain the V_{oc}-failure frequently observed in wide-band-gap devices. Last, the photoconductivity of CdS, which leads to non-superposition and distortion of the current-voltage curves, is addressed. The treatment of these problems is

Reproduced with permission of the copyright owner. Further reproduction prohibited without permission.

general with conclusions that are independent of particular material properties (parameter choices) and, therefore, apply to a wide range of CIS and CIGS devices. In each section, previous work is reviewed, the model applied to the problem is presented, and the results are discussed and summarized.

4.1 Compositional Ga/(Ga+In) grading in Cu(In,Ga)Se_2

The quaternary system of Cu(In,Ga)Se_2 (CIGS) has an adjustable band gap that varies with Ga content over a range of 1.04–1.67 eV. A non-uniform Ga/(Ga+In) ratio throughout the film thickness ("grading") allows additional fields to be built into p-type CIGS absorbers, and some researchers have asserted that these fields can significantly enhance the device performance. The experimental evidence that grading improves performance, however, has not been compelling, mostly because the addition of Ga itself improves device performance and, hence, a consistent separation of the grading benefit has not generally been achieved. Numerical modeling tools are used to show that (1) there can be a beneficial effect of grading, (2) in standard thickness CIGS cells the benefit is smaller than commonly believed, (3) there is also the strong possibility of reduced rather than of increased device performance, and (4) thin-absorber cells derive more substantial benefit.

4.1.1 Review

Substitution of Ga for In in Cu(In,Ga)Se_2 enlarges the band gap from 1.04 to 1.67 eV, with the change occurring primarily in the conduction band [72]. There are three typical approaches used in graded solar cells (displayed in Fig. 4.1). The band gap either increases toward the front of the absorber ("front grading"), toward the back ("back grading"), or both ("double grading"). Lundberg [73] gave a comprehensive summary of the different effects that can be expected due to these grading approaches. Here it shall only be noted, that the general expectation has been that (a) back grading by itself or contained in the double grading increases minority carrier collection from the bulk, because additional drift fields for electrons are established in the quasi-neutral region and (b) front grading separately or as part of the double grading leads to higher open-circuit voltage as the band gap in

Reproduced with permission of the copyright owner. Further reproduction prohibited without permission.

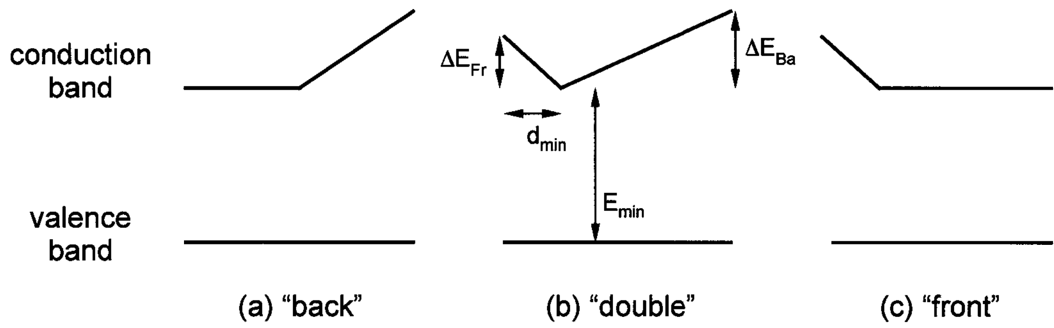

Figure 4.1: Typical grading approaches. E_g increases toward the back (a), front (c), or both (b). In (b), the grading parameters are defined.

the space-charge region (SCR) expands, while similar current-densities can be maintained. Both approaches are predicted to allow for combinations of V_{oc} and J_{sc} that are better than those that can be achieved with uniform absorber layers with constant E_g.

Record conversion efficiencies of CdS/CIGS thin-film solar cells are approaching 20% [25]. The absorber layers used in these cells are deposited by the three-stage process [74], which leads to non-uniform Ga/(Ga+In) composition versus absorber depth. Other methods commonly used, such as co-evaporation, allow the engineering of Ga/(Ga+In) profiles by varying the elemental fluxes during deposition. The effects of these non-uniform Ga/(Ga+In) compositions in $CuIn_{1-x}Ga_xSe_2$ have been broadly investigated by simulations and experiments. Simulations have predicted: (1) small (<0.5%) to moderate (<1%) improvements in efficiency with back grading [75–79], (2) small to large (>2%) improvements due to front grading [76–80] (3) small to large improvements in double grading approaches [75–78, 81, 82]. Interpretation of experiments has agreed reasonably well with these results, and there are reports in the literature of moderate improvements due to back grading [79, 83–85], moderate improvements due to front grading [79] and large improvements (>3%) due to double grading [81–83]. All of these results are summarized in Fig. 4.2, which shows the maximum efficiency gains reported. Often however, there is a wide range of results available when simulation parameters or experimental conditions were varied, such that back [76, 79, 83], front [76, 79, 84], and double grading [82] have also been observed to reduce efficiency.

Reproduced with permission of the copyright owner. Further reproduction prohibited without permission.

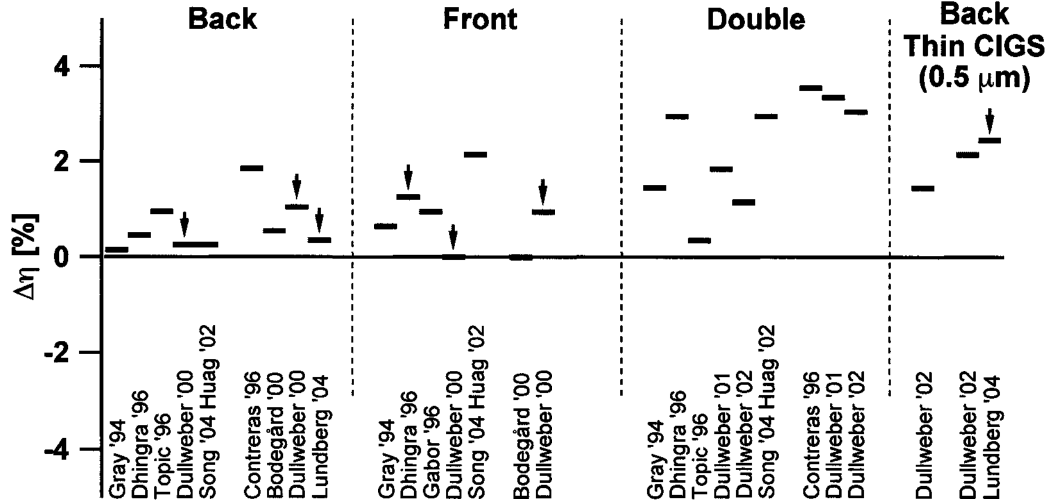

Figure 4.2: Reported maximum efficiency gains for CIS or low-Ga CIGS solar cells from simulations or experimental studies. Reference is given by first author and year of publication. Arrows indicate when an uniform band-gap energy other than the minimum band gap was used to establish reference performance.

4.1.2 Model

The starting point for the simulations is the three-layer CIGS baseline case discussed in Sect. 3.2.1 with additional mid-gap recombination centers being present in the absorber. This baseline configuration includes a 200-nm ZnO window, 50-nm CdS buffer, and 3-μm CIGS absorber layer. The uniform-Ga-content device efficiency with these parameters is shown as a function of the absorber band-gap in Fig. 4.3. It yields $\eta(E_g = 1.04 \text{ eV}) = 15.1\%$ and $\eta(E_g = 1.15 \text{ eV}) = 16.8\%$, which is typical for good CIS and ungraded CIGS solar cells. Recombination at the CdS/CIGS interface is not included as the results reported in Sect. 4.2 show that for positive band offsets, interface recombination has a negligible effect. For all cases considered here this criteria is fulfilled.

Band-gap variations (back, front, and double gradings, Fig. 4.1) are described by the parameters: linear E_g-increase toward the front or back (ΔE_{Fr} or ΔE_{Ba}), minimum band gap (E_{min}), and distance of the minimum from the junction (d_{min}). The numerical model approximates these variations by discrete layers of varying band gap and optical absorption spectrum. The band-gap difference between two adjacent layers is always less than 2kT and in most cases less than kT (26 meV). Hence, a graded device model typically consists of 10–25 layers of absorber material. The absorption spectrum reported for 1.15 eV-CIGS

Reproduced with permission of the copyright owner. Further reproduction prohibited without permission.

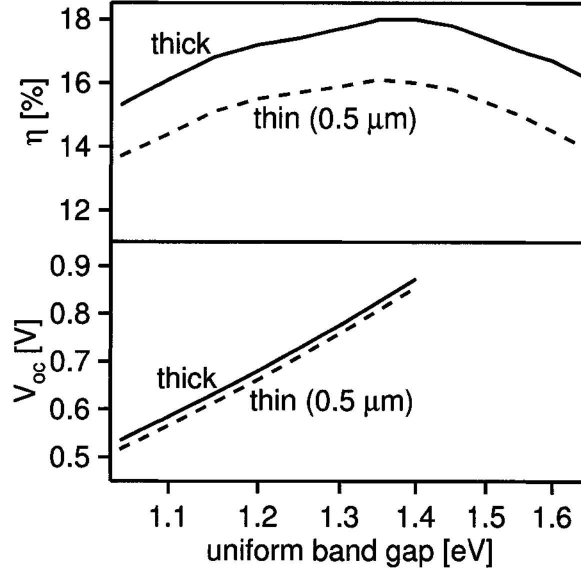

Figure 4.3: η and V_{oc} for uniform band-gap absorbers with thicknesses of 3 μm and 0.5 μm. Up to 1.4 eV, η increases monotonically with E_g and V_{oc}. For higher E_g, V_{oc} depends on the CdS/CIGS interface quality and a V_{oc}-limitation can occur (Sect. 4.2).

[59] is used, and it is shifted on the energy axis according to the band-gap in each layer.

4.1.3 Identifying the true grading benefit

Typical high-efficiency devices have minimum band gaps of 1.1 to 1.2 eV. Addition of a Ga/(Ga+In) grading to an absorber with a minimum band gap E_{min} < 1.4 eV *may increase its performance due to either the grading benefit or the increase in average Ga content* (higher average band gap in Fig. 4.3). In fact, Dullweber et al. [79] observed a close correlation between the average Ga-content and the device performance, independent of the Ga distribution. Except for references [76, 79, 85], uniform band-gaps equal to the graded band-gap minimum (1.04 eV "CIS," in most cases) are used for comparison to determine the grading benefit. This unfortunate selection of the reference performance, results in overestimates of efficiency gains attributed to the grading benefit, especially for front and double grading structures where the band gap increases in high recombination regions. In Refs. [76] and [79] an average band-gap is used for comparison (red arrows in Fig. 4.2), and in Ref. [85] the results are normalized to the optical band-gap (blue arrows in Fig. 4.2).

When the band-gap of the absorber layer increases, V_{oc} will increase and J_{sc} will decrease

Reproduced with permission of the copyright owner. Further reproduction prohibited without permission.

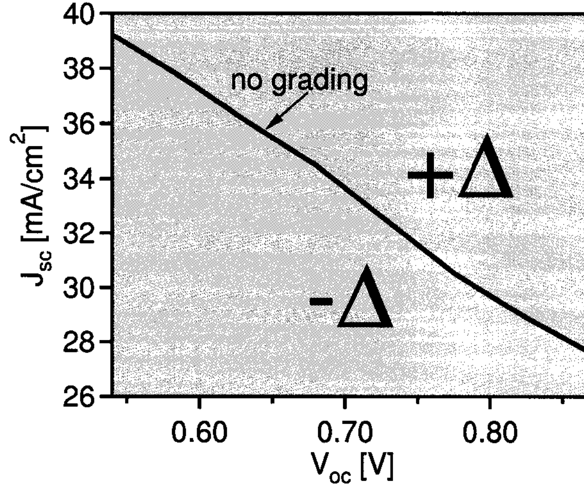

Figure 4.4: Objective evaluation of grading benefits by comparison to common V_{oc}.

(e.g., see Fig. 4.13 in Sect. 4.2.3). As stated in the introduction, grading is believed to achieve a combination of V_{oc} and J_{sc} that is improved compared to uniform band-gap devices. This is illustrated in Fig. 4.4 where J_{sc} is plotted vs. V_{oc}. The black line corresponds to uniform band-gap absorbers. If grading is beneficial, the resulting (V_{oc}, J_{sc}) pair will lie above the black line, and a net benefit is achieved that is not possible with uniform absorbers. On the contrary, points below the black line in Fig. 4.4 indicate losses due to grading. The true grading benefit will be apparent if the quantitiy

$$\Delta X = X(\Delta E_{fr}, \Delta E_{ba}, d_{min}) - X(const\, E_g, same\, V_{oc}) \tag{4.1}$$

is studied, where X = J_{sc}, FF, or η. This comparison establishes an objective and absolute criteria for grading benefits, independent of changes in average Ga composition. The alternative comparison to the effective optical band-gap used in Ref. [85] would yield similar results.

4.1.4 Results

Back grading

Back grading establishes an additional drift field for minority electrons that assists carrier collection and reduces back-contact recombination. Normalized current-voltage parameters

Reproduced with permission of the copyright owner. Further reproduction prohibited without permission.

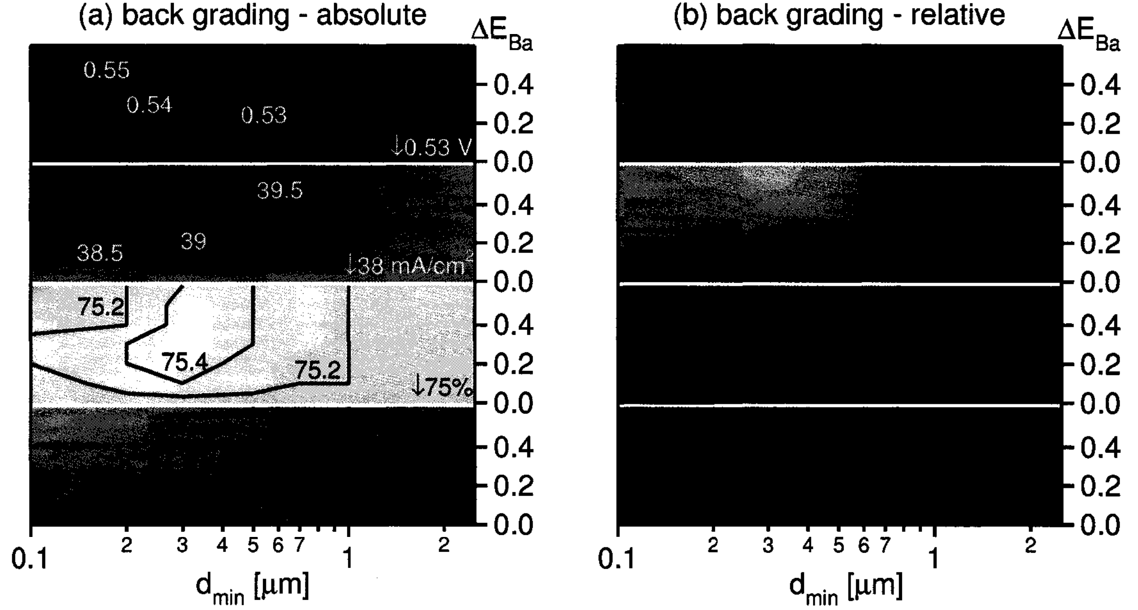

Figure 4.5: Performance evaluated for back gradings with ΔE_{Ba} = 0–0.6 eV. (a) Absolute scale; performance of minimum-uniform band-gap (1.04 eV) is given in the lower right corner of each plot. From top to bottom: V_{oc} (V), J_{sc} (mA/cm^2), FF (%), and η (%). (b) Normalized results show the true grading benefit. From top to bottom: $\Delta V_{oc} = 0$, ΔJ_{sc} (mA/cm^2), ΔFF (%), and $\Delta\eta$ (%).

for E_{min} = 1.04 eV, ΔE_{Ba} = 0–0.6 eV, and d_{min} = 0.1–2.5 μm are shown in Fig. 4.5(a) in terms of absolute performance and in Fig. 4.5(b) the normalization expressed in Eq. 4.1 was applied. Compared to the minimum-uniform band-gap (1.04 eV) performance, back grading increases V_{oc} once it extends throughout the quasi-neutral bulk, such that d_{min} is close to or within the SCR. J_{sc} forms a small maximum of 39.5 mA/cm^2 and overall η gains are slightly over 1%.

Applying the normalization (Fig. 4.5[b]), a small J_{sc} increase of ~1.5 mA/cm^2 is observed once the back grading extends into the front half of the device (d_{min} < 1.5 μm). This is weakly dependent on the parameter ΔE_{Ba}. FF shows a negligible decrease with large ΔE_{Ba} and small d_{min}. The net gain in efficiency is typically 0.5%. With ΔE_{Ba} > 0.4 eV and $d_{min} \approx 0.3$ μm, a maximum benefit of $\Delta\eta$ = 0.7% is observed.

One example of the resulting band structure is shown in Fig. 4.6. The *discrete* back grading is clearly visible in the conduction-band steps toward the back contact. As long as these steps are small, electrons can flow freely across these discontinuities and the electron

Reproduced with permission of the copyright owner. Further reproduction prohibited without permission.

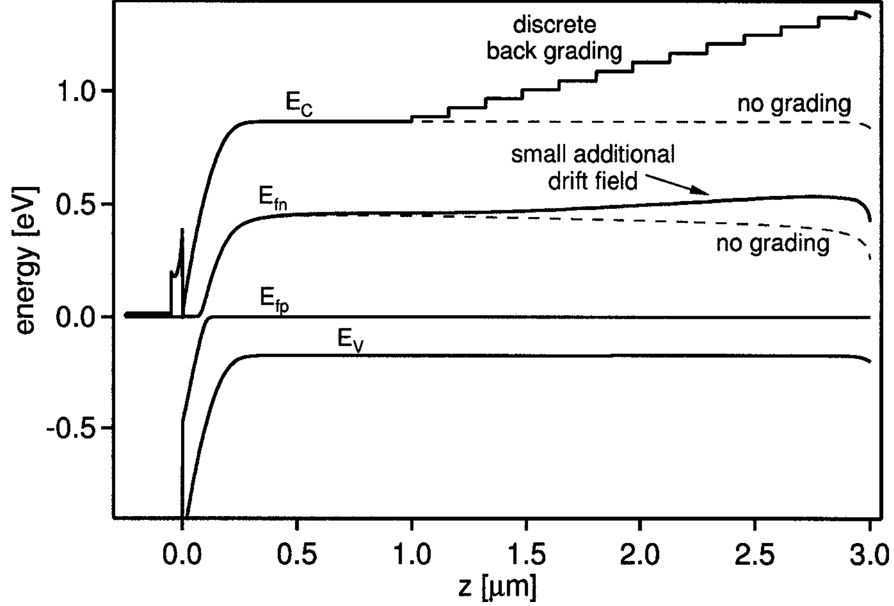

Figure 4.6: Back grading with $\Delta E_{Ba} = 0.5$ eV and $d_{min} = 1$ μm. Conduction and valence bands and quasi-Fermi levels under one-sun illumination and zero bias.

quasi-Fermi level, E_{fn}, represents a smooth function. Electron current flow can in general be expressed as [15]

$$J_n = -qn\mu_e \nabla\phi_{fn}. \tag{4.2}$$

$\phi_{fn} = -(E_{fn}/q)$ is the electron quasi-Fermi potential. The positive slope in E_{fn} indicates a net electron flow toward the front junction. E_{fn} for an ungraded device is shown in comparison (dashed lines in Fig. 4.6) and this curve has a small negative slope indicating electron flow toward the back contact (loss in J_{sc}). The grading "strength" is $\Delta E_{Ba}/q(W - d_{min}) \simeq 2500$ V/cm, but the resulting effective drift field

$$\mathcal{E}_e = -\nabla\phi_{fn} \tag{4.3}$$

is only the order of ~500 V/cm. The effective drift field for electrons is indeed much weaker than the slope of the grading. Equality between the latter and $\mathcal{E}_e$ could only be achieved if the electron density throughout the device would be constant (E_{fn} parallel to E_V), but this is unlikely because (1) the intensity, and therefore the generation, falls off exponentially as a function of penetration depth, (2) the expanding band-gap results in less absorption, and

Reproduced with permission of the copyright owner. Further reproduction prohibited without permission.

(3) the back-contact recombination leads to minority carrier depletion.

The improvement in the drift/diffusion length can be estimated assuming carrier drift during the carrier lifetime τ_e [85]:

$$\Delta L = \mu_e \cdot \mathcal{E}_e \cdot \tau_e. \tag{4.4}$$

Reference [85] suggested use of $\mathcal{E}_e \approx \Delta E_{Ba}/q(W - d_{min})$, but Fig. 4.6 implies that this would overestimate the benefit of grading. Using Eq. 4.3 and $\tau_e \sim 2 \times 10^{-9}$ s (baseline values), $\Delta L \approx 1$ μm for the case shown in Fig. 4.6. This represents a significant improvement compared to the baseline diffusion length of $L_e \approx 0.7$ μm. Most effective back grading occurs where carriers have a high photogeneration density and less-than-ideal collection efficiency. This is the case just a few tenths of a micrometer outside the SCR (Fig. 4.5[b]). For larger d_{min}, fewer carriers will be affected, and for smaller d_{min}, the grading extends into the SCR where collection is very good even in the absence of grading such that no further improvement is achieved.

Front grading

Grading toward the front of the device by itself is not commonly used in well-working devices. It has however, been studied thoroughly (Fig. 4.2), particularly due to its application in double grading structures. Front grading increases the band gap in the SCR where most of the recombination occurs (e.g., see Fig. 3.4 in Sect. 3.2). However, the enlarged band gap also leads to deeper absorption such that generated minority carriers are more likely to recombine before they are collected. *J-V* results for front gradings of magnitude ΔE_{Fr} = 0–0.3 eV are shown in Fig. 4.7, again on the absolute (a) and relative (b) scale.

The absolute results show that V_{oc} increases as the front grading extends far into the back of the device. This is logical, as the average band-gap, particularly the band gap in the SCR increases. At the same time J_{sc} decreases. FF shows a significant loss centered around d_{min} ~ 0.3 μm. Overall, the efficiency is always reduced compared to CIS (1.04 eV) performance. The same conclusion can be drawn from the normalized results in Fig. 4.7(b); these results, however, further show that the trade-off between V_{oc} and J_{sc} is indeed much worse than

Reproduced with permission of the copyright owner. Further reproduction prohibited without permission.

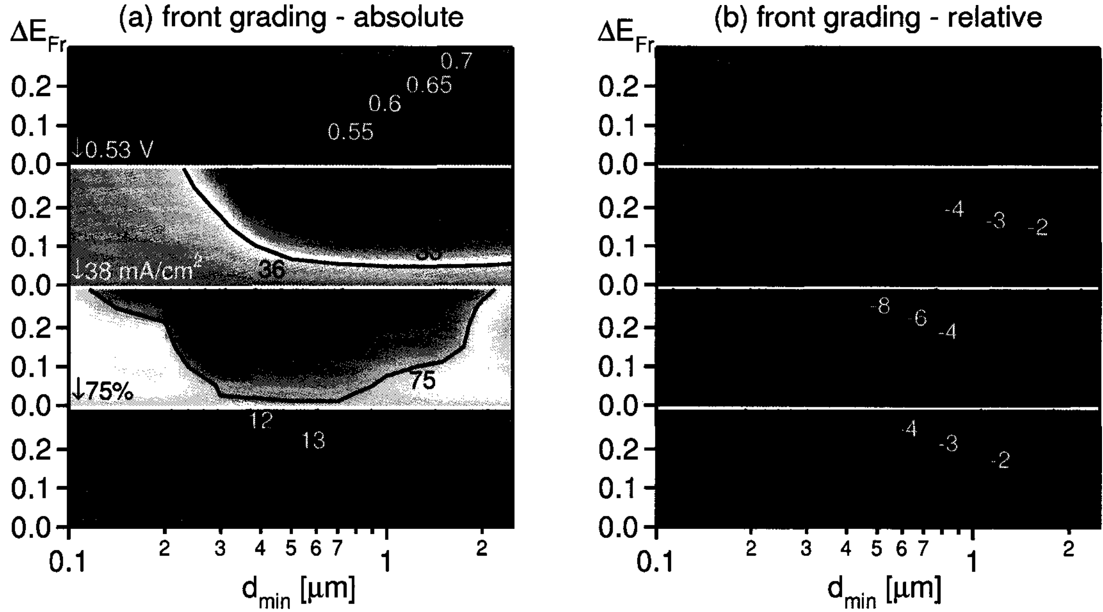

Figure 4.7: Performance evaluated for front gradings with ΔE_{Fr} = 0–0.3 eV. (a) Absolute scale; performance of minimum-uniform band-gap (1.04 eV) is given in the lower left corner of each plot. From top to bottom: V_{oc} (V), J_{sc} (mA/cm^2), FF (%), and η (%). (b) Normalized results show the true grading benefit. From top to bottom: $\Delta V_{oc} = 0$, ΔJ_{sc} (mA/cm^2), ΔFF (%), and $\Delta\eta$ (%).

that expected from a comparison with uniform band-gap increases. The graded device structures achieve significantly lower J_{sc}'s when compared to uniform band-gap absorbers with the same V_{oc}.

Figure 4.8 shows the conduction band for three different front gradings with $d_{min} = 0.1$, 0.3, and 1 μm (a) at a voltage between the maximum power voltage and V_{oc} and (b) at zero bias. For small d_{min}, the front grading is completely contained in the SCR and slightly reduces the field. With $d_{min} = 0.3$ μm, good collection is still possible at zero voltage (no reduction in J_{sc}). However, a barrier exists under forward bias that leads to poorer collection and is observed as a reduction in FF. The location of this barrier, which separates the good collection region, $z < z_{barrier}$, from the poor collection region, $z > z_{barrier}$, shifts with the applied voltage and this leads to a voltage-dependent collection effect. FF reduces for d_{min}'s that are larger than ~0.2 μm (Fig. 4.7[b]), which corresponds to the depletion width under forward bias. Larger values for d_{min} lead to barriers under all condition, reducing J_{sc} and FF. With lower doping concentrations (here 2x10^{16} cm^{-3} was used for the

Reproduced with permission of the copyright owner. Further reproduction prohibited without permission.

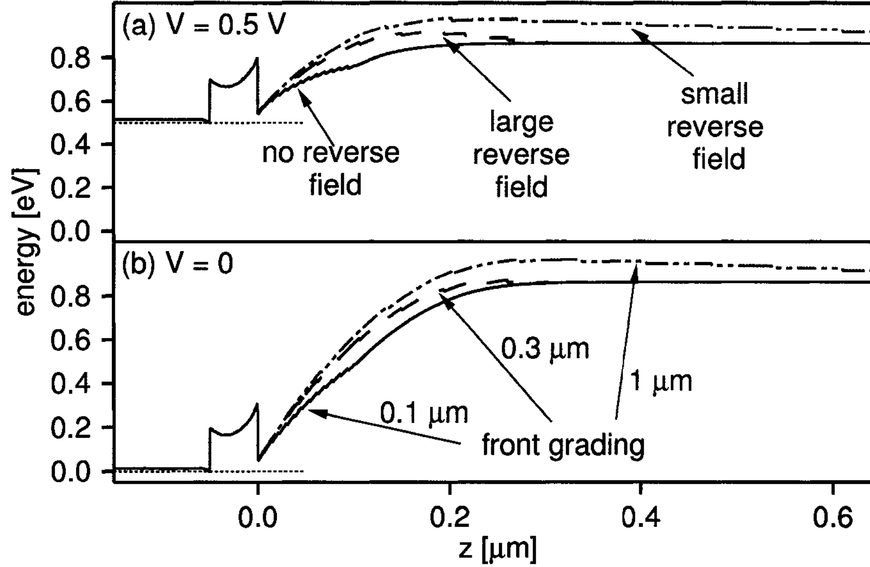

Figure 4.8: Conduction band (a) at forward bias and (b) at zero bias for front gradings with ΔE_{Fr} = 0.2 eV and d_{min} = 0.1 μm, 0.3 μm, and 1.0 μm. Intermediate positions of the band-gap minimum lead to a significant reverse field for electrons.

CIGS), the SCR widens and the range of d_{min} that is unfavorable is expected to decrease.

Double grading

Conceptually, double grading allows increased performance by achieving a high J_{sc}, which is determined by the minimum band-gap in the device, and at the same time increased V_{oc}, due to the locally increased band gap in the SCR. This principal of "band-gap separation" was experimentally verified by Dullweber et al. [86]. The quantified η gains reported in Ref. [82], however, used the minimum band-gap absorber as reference performance and, hence, overestimated the grading benefit.

The normalized current-voltage parameters from simulations with E_{min} = 1.04 eV, ΔE_{Ba} = 0–0.6 eV, $\Delta E_{Ba}/\Delta E_{Fr}$ = 2, and d_{min} = 0.1–2.5 μm show that the double grading benefits are rather modest. On the absolute scale (Fig. 4.9[a]), a similar trade-off between V_{oc} and J_{sc} exists as for the front grading. A small region of increased FF is observed and the highest efficiency is 17%, an increase of 2% over uniform 1.04 eV performance.

The relative results (Fig. 4.9[b]) clearly show that double grading can in fact be seen as a superposition of front and back grading effects. For d_{min} < 0.3 μm the simulations predict J_{sc} gains similar to those seen with the back grading. For larger d_{min}, however, J_{sc}

Reproduced with permission of the copyright owner. Further reproduction prohibited without permission.

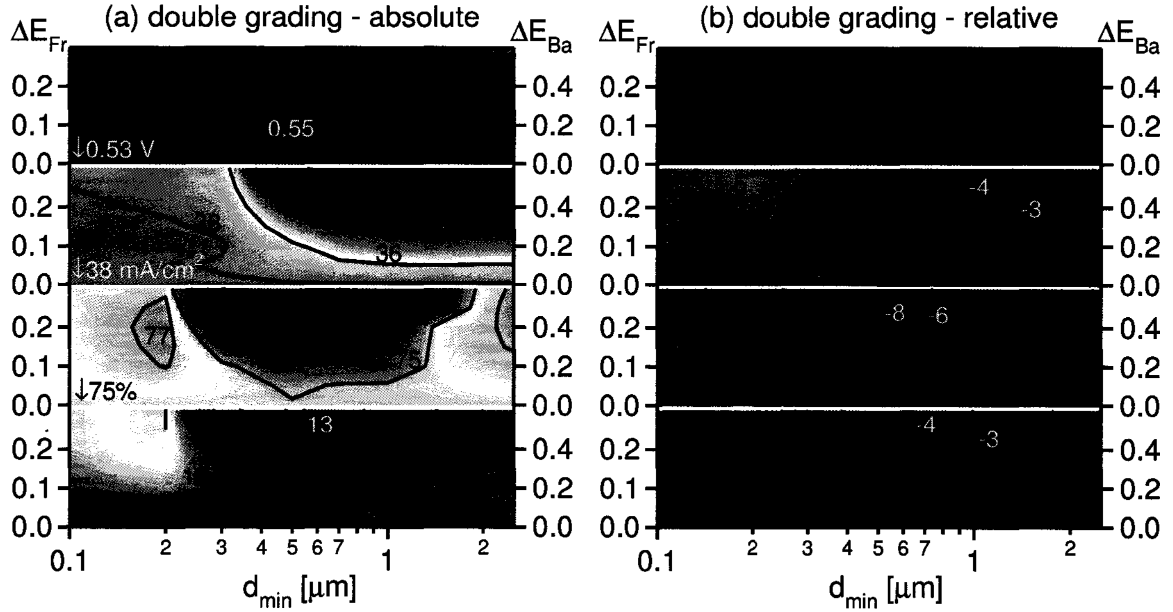

Figure 4.9: Performance evaluated for double gradings with ΔE_{Fr} = 0–0.3 eV and ΔE_{Ba} = 0–0.6 eV. (a) Absolute scale. From top to bottom: V_{oc} (V), J_{sc} (mA/cm^2), FF (%), and η (%). (b) Normalized results show the true grading benefit. From top to bottom: ΔV_{oc} = 0, ΔJ_{sc} (mA/cm^2), ΔFF (%), and $\Delta\eta$ (%).

is strongly reduced, as much as 5 mA/cm^2, depending on the height of ΔE_{Fr}. FF improves with small d_{min}, but it also shows considerable reduction for intermediate d_{min} in the range of 0.2–1.5 μm. The highest efficiency gain is close to 1% when the minimum band gap is located in the middle of the space-charge region near 0.2 μm. Comparing this 1% increase with the 0.7% achieved by back grading alone, the additional gain achieved by *band-gap separation* is quite modest.

The front grading has been observed as a detrimental effect and, therefore, it is questionable, whether the choice of r = $\Delta E_{Ba}/\Delta E_{Fr}$ used in Fig. 4.9 is ideal. Double grading with different ratios of r = 1, 2, and 3 are evaluated (Fig. 4.10). The larger r, the less front grading is present and the J_{sc} and FF losses are reduced (Fig. 4.10[b]): $\Delta\eta_{max}$ increases from 0.6% for r = 1, 1% for r = 2, to 1.2% for r = 3. This also increases the gain from electrical and optical band-gap separation to about ~0.5% for r = 3.

Reproduced with permission of the copyright owner. Further reproduction prohibited without permission.

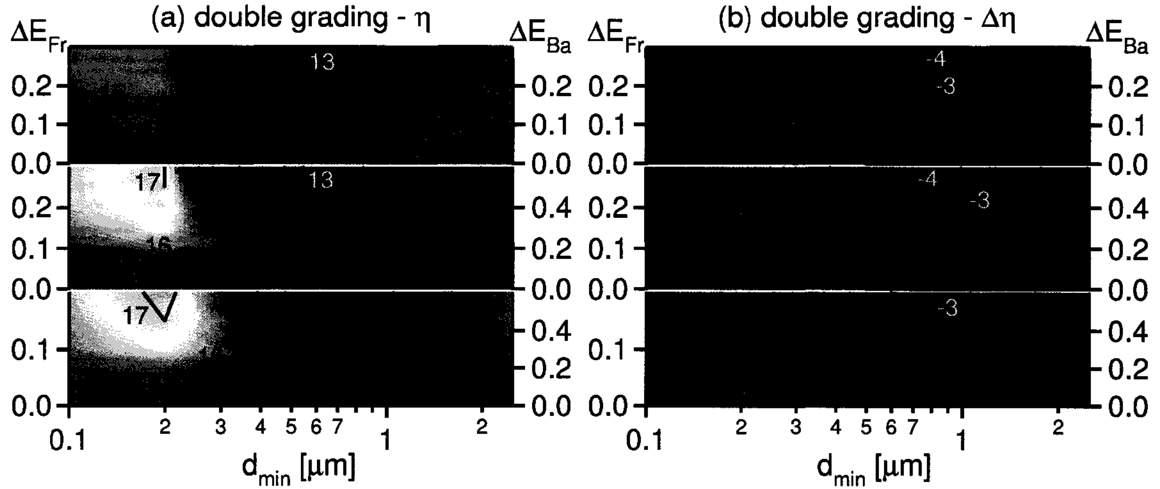

Figure 4.10: Solar-cell efficiency with varying back/front grading ratio r = $\Delta E_{Ba}/\Delta E_{Fr}$. (a) Absolute scale. (b) Normalized results show true grading benefit.

"Thin" $Cu(In,Ga)Se_2$

Material and deposition costs in large-scale manufacturing can be greatly reduced by thinning the CIGS absorber layers from standard thicknesses of 2–3 μm. Optically, roughly 0.5 μm is sufficient to absorb 90% of the light with $E_{ph} > E_g$, even without considering reflection of the light at the back contact. Lundberg et al. [87] investigated the performance of CIGS solar cells as a function of absorber thickness and found that the dominanting loss for thinner absorber layers is a reduction of J_{sc}. This J_{sc}-loss exceeded the reduction in generation, because there is also increased back-contact recombination.

Predicted efficiencies for the constant band-gap model with a reduced absorber thickness of 0.5 μm are shown in Fig. 4.3. Efficiencies are lowered by about 2% compared to the thick absorbers, and these losses are mostly in J_{sc}, followed by a lower FF, and a slightly reduced V_{oc}. Experimentally, an efficiency loss closer to 6% has been observed for 0.5 μm CIGS [87]. This larger loss is most likely correlated to the experimental difficulties in adjusting the film thickness without changing other film parameters at the same time, especially morphology and defect structure. In this sense, the "thin" solar-cell model is incomplete as it only considers performance changes caused by reduced absorption and increased back contact recombination.

Incorporating back gradings into such devices can be greatly beneficial. The results are

Reproduced with permission of the copyright owner. Further reproduction prohibited without permission.

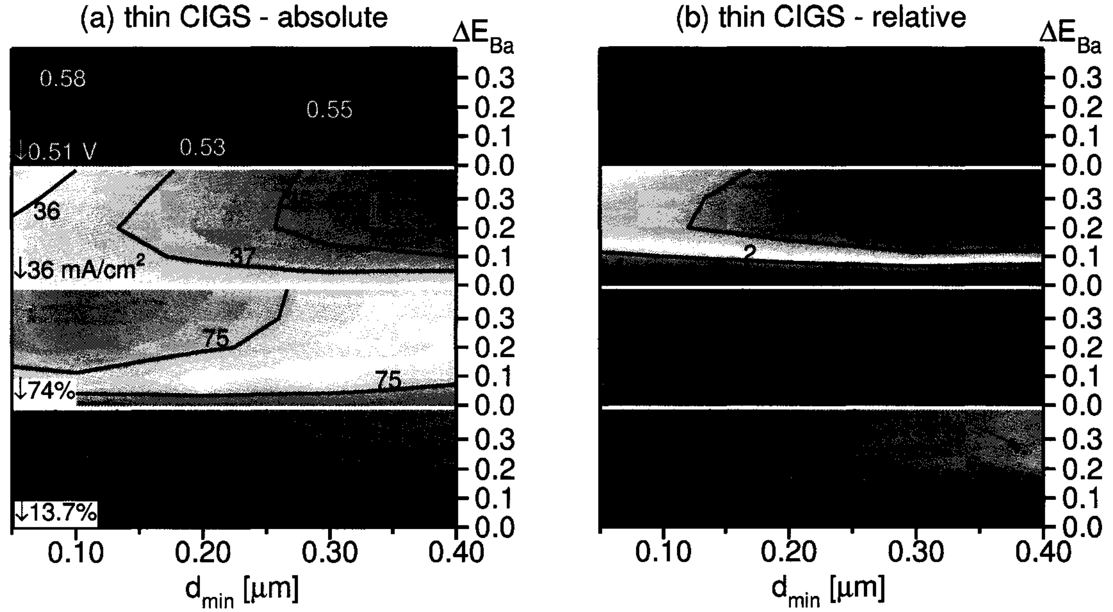

Figure 4.11: Performance evaluated for thin CIGS solar cells with back gradings. (a) Absolute scale. From top to bottom: V_{oc} (V), J_{sc} (mA/cm^2), FF (%), and η (%). (b) Normalized results show true grading benefit. From top to bottom: $\Delta V_{oc} = 0$, ΔJ_{sc} (mA/cm^2), ΔFF (%), and $\Delta\eta$ (%).

shown in Fig. 4.11. Particularly from the normalized plot (b), it is apparent that a significant gain in J_{sc} can be achieved. For steep gradings, the back contact becomes passivated and the J_{sc} losses introduced by thinning are recovered. J_{sc} with $d_{min} > 0.25$ μm is practically identical to the J_{sc} achieved by thick-ungraded absorbers. Hence, absorber thinning is predicted to be practical without a significant loss in efficiency, if an appropriate back grading is employed.

4.1.5 Summary

The best device efficiencies and the conditions under which they were achieved are summarized in Table 4.1. Back grading in CIGS solar cells is seen to improve simulated device efficiency compared to ungraded devices. For devices with standard thicknesses, the effect is small, around 0.5% in efficiency. The potential efficiency gain increases significantly as the absorber thickness is reduced. Improvements of 2% are predicted at a thickness of 0.5 μm, which means that the thinning losses are nearly fully recovered. These efficiency gains are in good agreement with experimental work [85], but experimentally the thinning losses were

Reproduced with permission of the copyright owner. Further reproduction prohibited without permission.

Table 4.1: Summary of the grading benefits. Maximum efficiency gains achieved after normalization.

grading	ΔE_{Fr} (eV)	ΔE_{Ba} (eV)	d_{min} (μm)	$\Delta\eta_{rel}$ (%)	comments
back	0	>0.3	~0.3	**0.7**	$d_{min} \gtrsim W_{scr}$
front	-	-	-	**<0**	no improvement
double	$\frac{1}{2}\Delta E_{Ba}$	>0.3	~0.2	**1**	$d_{min} < W_{scr}$
double	$\frac{1}{3}\Delta E_{Ba}$	>0.5	~0.2	**1.2**	$d_{min} < W_{scr}$
thin-back	0	>0.2	>0.3	**1.9**	

greater and not fully recovered by adding back grading. Double grading shows benefits similar to those from back grading, but the additional front grading can lead to large losses in FF and J_{sc}, if the band-gap minimum is not contained within the space-charge region. The large FF loss has been observed by Topič et al. [75] and was argued to be due to the reverse drift field for the minority carriers. The results presented in this work confirm this conclusion.

Although frequently believed to be a major contributor to high efficiency devices, it has been shown that the benefit that can be expected by implementing back, front, or double grading in standard-thickness CIGS solar cells to be small. Large losses in FF and J_{sc} can be realized with front and double gradings. Thin CIGS devices, however, can benefit significantly from a back grading that reduces back contact recombination.

4.2 Band alignment at the CdS/CIGS heterojunction

Wide-band-gap chalcopyrite solar cells, most prominently $Cu(In,Ga)Se_2$ with high Ga content, have failed over the past years to achieve conversion efficiencies consistent with those achieved with lower-Ga CIGS. Starting from a simple baseline case of a ZnO/CdS/CIGS solar cell, the effects of bulk and interface recombination for a broad range of absorber band-gap energies are investigated assuming that the Ga/In ratio primarily affects the conduction band. The model predicts that even very small interface recombination velocities limit the open-circuit voltage, when the conduction-band offset (CBO) between window and absorber layer is close to zero or is negative. This is the case for CdS/CIGS structures with

Reproduced with permission of the copyright owner. Further reproduction prohibited without permission.

absorber band gaps above 1.3–1.4 eV. The simulations further predict that surface phases or pinning of the Fermi level at the interface can inhibit interface recombination, and hence, lead to an improvement in cell efficiency. Conversion efficiencies for all band-gap energies are calculated based on a generic window layer/absorber structure assuming that the band alignment can be arbitrarily chosen.

4.2.1 Review

Earlier work discussed the effect of the CBO for CdS/CIS [88–90] or low-Ga content CdS/CIGS solar cells [91] assuming a fixed absorber band gap while the CBO was varied. It has been observed that increasing recombination at the window-absorber interface lowers the open-circuit voltage for negative CBO [89–91] and, hence, a positive band offset is important for high device performance. Many attempts in recent years to increase V_{oc} of the Cu(In,Ga,Al)Se_2 system beyond 0.8 V have not been successful [92–95]. The open-circuit voltage increases proportionally to the absorber band gap, E_g, up to band-gap energies of about 1.3 eV; in this lower regime the approximate expression $V_{oc} = E_g - 500$ mV holds reasonably well [94]. For larger band gaps, the difference between V_{oc} and E_g increases, and for high band gaps V_{oc} is constant at about 0.8 V.

4.2.2 Model

The modeling calculations presented in this section used the software tool SCAPS-1D [38] (Sect. 3.3). Recombination currents are calculated with the Shockley-Read-Hall (SRH) model for bulk defects and an extension of the SRH model for interface defects:

$$R_{intf} = \frac{np - n_i^2}{(n + n_1)/S_p + (p + p_1)/S_n} \tag{4.5}$$

where all parameters have their usual meaning as introduced in Sect. 3.1.3. For simplicity it is assumed $S_n = S_p = S$. The interface quality is expressed as a recombination velocity S in units of (cm/s); a general reference level is the thermal velocity v_{th} ($\approx 10^7$ cm/s), $S \sim v_{th}$ would imply that every minority carrier reaching the interface recombines. The SRH interface approach implemented in SCAPS-1D allows carriers from both conduction

Reproduced with permission of the copyright owner. Further reproduction prohibited without permission.

and valence bands to participate in the interface recombination process. A recombination process, as outlined in Sect. 3.1.3, can therefore occur between CdS-electrons and CdS-holes, CdS-electrons and CIGS-holes, CIGS-electrons and CIGS-holes, and CIGS-electrons and CdS-holes.

The starting point is the baseline case as described in Sect. 3.2.1 with additional bulk recombination centers ("neutral" defect states, with large capture cross sections and small density) being present. The latter was added so that bulk-recombination can be investigated over a broad range of carrier lifetimes without introducing significant additional charge in Eq. 3.1. Starting from this configuration, the band gap is varied under the assumption that changes occur in the conduction band only, as it would be expected for interchanging Ga or Al for In in $CuInSe_2$ [72]. *J-V* curves are calculated for band-gap energies in the range from 0.85–2.05 eV, which intentionally exceeds the physical limits of the $Cu(In,Ga)Se_2$ system, since the results should be general and not limited to this particular material system. The conduction-band offset varies in the model from +0.6 eV to –0.6 eV. The CBO is positive (spike, i.e., Fig. 4.12[a]), by convention, if conduction- and valence-band offset (VBO) are

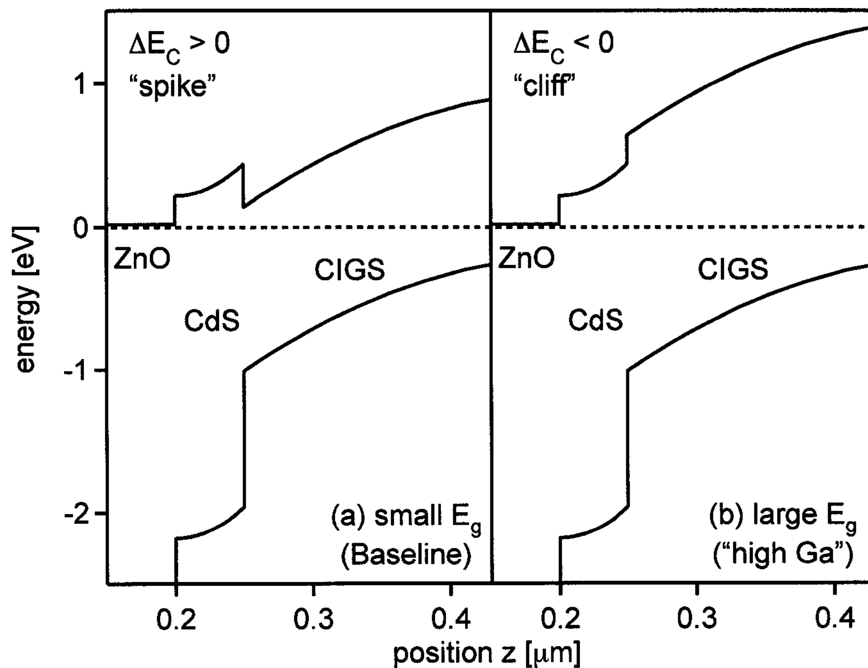

Figure 4.12: Conduction and valence band for (a) a small and (b) a large band-gap ZnO/CdS/CIGS solar cell.

Reproduced with permission of the copyright owner. Further reproduction prohibited without permission.

both smaller than the band-gap difference, ΔE_g. If the VBO is larger than ΔE_g, then the CBO is negative (cliff, i.e., Fig. 4.12[b]).

4.2.3 Bulk vs. interface recombination

Figure 4.13 shows the simulated J-V results with spatially uniform bulk recombination centers for the range of band gaps investigated. V_{oc} increases as $V_{oc} = E_g - 530$ mV, and J_{sc} decreases with increasing band gap due to the lower-wavelength cut off. For a CBO greater than 0.5 eV, J_{sc} is dramatically reduced due to the large spike barrier for photogenerated electrons. The fill factor is relatively flat and decreases with large offsets in either direction due to cliff or spike barriers. In this simulation without interfacial recombination, the highest efficiency of 18.3% is achieved with a band gap of 1.35 eV, however, 17–18% devices are calculated with band gaps from 1.15–1.55 eV, which corresponds to conduction-band offsets of +0.3 eV to –0.1 eV. The previous results change only quantitatively if the density, $N_{Baseline}$ or N_{BL}, of the charge-free recombination centers, which are assumed mid-gap for all band gaps, is increased (3x, 10x, 30x, 100x) (Fig. 4.13). V_{oc} losses are slightly higher for band gaps below 1.5 eV. With 100xN_{BL}, the highest efficiency drops to 11.4%, and 10–11% devices are found for band-gap energies of 1.25–1.75 eV.

When charge-free recombination centers at the CdS/CIGS interface are added to the model, there is a qualitative change in the variation of voltage with band-gap energy. V_{oc} and η are shown for the range of absorber band gaps (Fig. 4.14) for interface recombination velocities $S \sim 0$, 10^3, 10^4, 10^5, and 10^6 cm/s. $S = 0$ corresponds to the baseline presented in Fig. 4.13.

For negative CBOs, V_{oc} depends on the interface quality, but becomes independent of the absorber band gap. This is in good agreement with earlier results [89–91] that showed that for a constant absorber band gap V_{oc} decreases approximately at the same rate as the CBO and the analytical predictions of a band-gap-independent open-circuit voltage [96]. For devices with negative CBOs, the dominating recombination current flows through the interface states and depends only on the electron and hole density at the interface. With $S \sim 10^5$ cm/s, the highest efficiency is only slightly reduced to 17% with a band gap of 1.25 eV, but the range of high efficiency results (16–17%) is limited to band gaps

Reproduced with permission of the copyright owner. Further reproduction prohibited without permission.

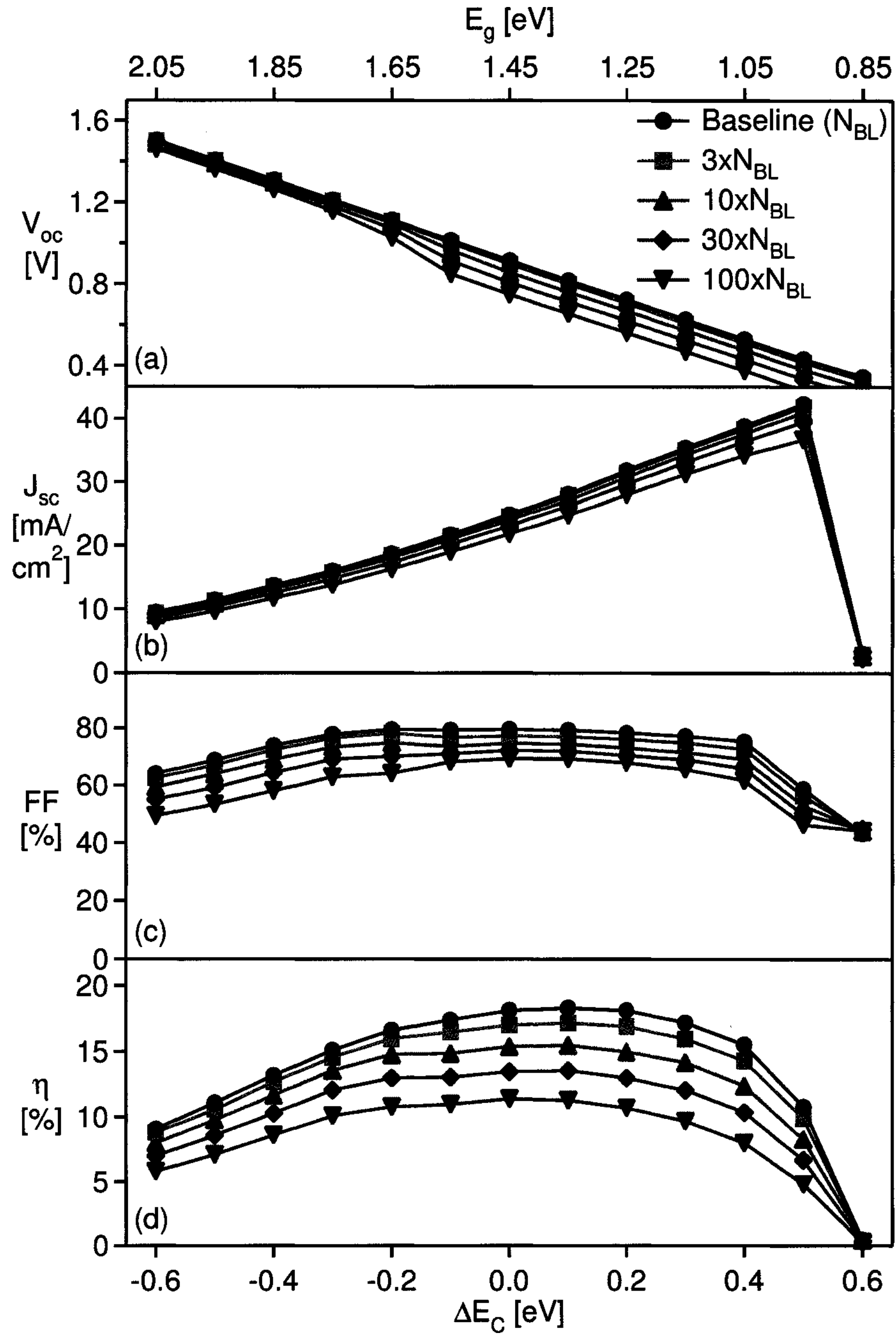

Figure 4.13: Simulated *J-V* parameters with increasing density of bulk recombination centers. Filled circles correspond to the baseline trap-density case with varying absorber band gap. CdS window is assumed.

(1.15–1.35 eV) that have a positive band offset. J_{sc} and FF results are unchanged except that no FF reduction occurs for large negative CBO, since the cliff barrier is ineffective when the dominating current flows through the interface.

Reproduced with permission of the copyright owner. Further reproduction prohibited without permission.

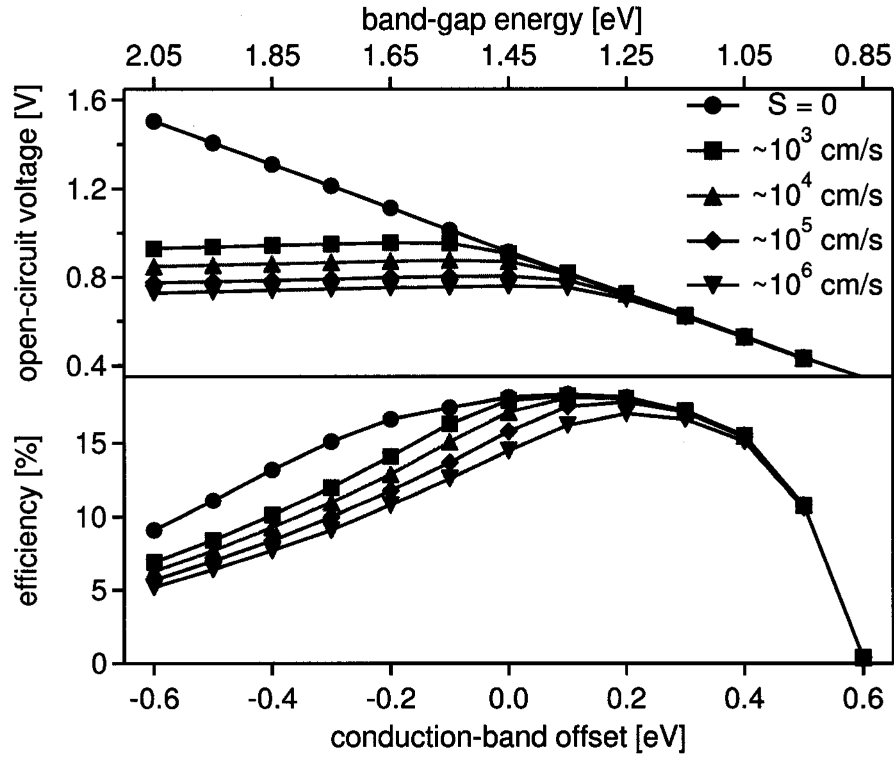

Figure 4.14: Effects of interface recombination on V_{oc} and η. Interface quality is parameterized as an approximate interface recombination velocity. The case with $S \sim 10^5$ cm/s is used as basis for further investigations (IF-BL).

$S \sim 10^5$ cm/s results in the best match to experimental V_{oc}'s [92–95, 97], the comparison is shown in Fig. 4.15. This configuration is the starting point for calculations discussed in the following sections and will be referred to as the interface-baseline (IF-BL).

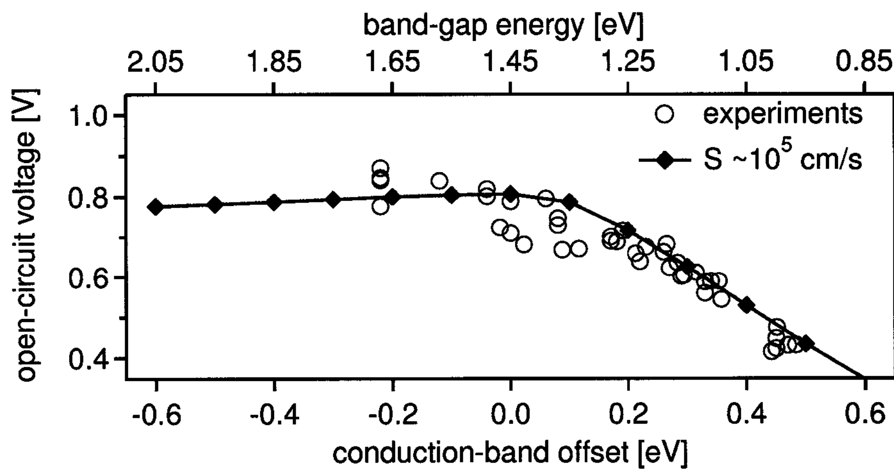

Figure 4.15: V_{oc}-limitations calculated for $S \sim 10^5$ and experimental results [92–95, 97].

Reproduced with permission of the copyright owner. Further reproduction prohibited without permission.

4.2.4 Alternative windows — efficiency limits

Considerable current may be lost due to absorption in a CdS window layer. In addition, the above results imply that a favorable band alignment is necessary to achieve high open-circuit voltages. A possible solution for wider-band-gap CIGS is alternative window or buffer materials such as Zn(O,S) compounds that have larger band gaps and a more optimal CBO. For Zn(O,S), the CBO should increase with S content according to theoretical studies [72]. Experimental efficiency of 18.6% has been demonstrated for ZnS(O,OH) window layers [98], which is very promising for future work. Many other materials have been investigated as alternatives for the standard ZnO/CdS configuration such as CdZnS, ZnSe, $ZnIn_2Se_4$, In_2S_3, In_2Se_3, $In(OH)_xS_y$, and others. A review of alternative window and buffer materials and a comprehensive compilation of references is given in Ref. [32].

Here, a systematic study of alternative windows is performed focusing on the effect of the resulting band-alignment on solar-cell performance. The results presented form an upper bound to achievable device performance that all configurations will be subject to. It is likely, however, that other mechanisms besides an unfavorable band offset will lower experimentally observed device efficiencies. Many benefits have been identified with the standard ZnO/CdS layers that might not be readily achieved with alternative configurations, such as (1) prevention of shunting by the CdS buffer, (2) protection of the absorber during ZnO sputtering by the CdS buffer, or (3) passivation of surface defects.

To evaluate the potential of alternative windows, the calculations for the same band gap range are repeated starting from a modified IF-BL that has an alternative window layer instead of the standard ZnO-CdS. The window layer is assumed to have characteristics similar to ZnO (n^+, $E_g \sim 3$ eV). The window/absorber band alignment is set to be +0.9 eV, +0.6 eV, +0.3 eV (IF-BL), or 0 eV with respect to the 1.15 eV absorber and varies with the absorber band gap. The larger offsets are a more favorable match for higher band-gap absorbers. V_{oc} and η results are shown in Fig. 4.16. For window layers that create larger offsets, the V_{oc}-limitation occurs at progressively higher voltages. This allows device efficiencies greater than 18% in the range of absorber band gaps from 1.15 eV to 1.75 eV, covering almost the complete $Cu(In,Ga)Se_2$ range. Large spike barriers (CBO > 0.4–0.5 eV)

Reproduced with permission of the copyright owner. Further reproduction prohibited without permission.

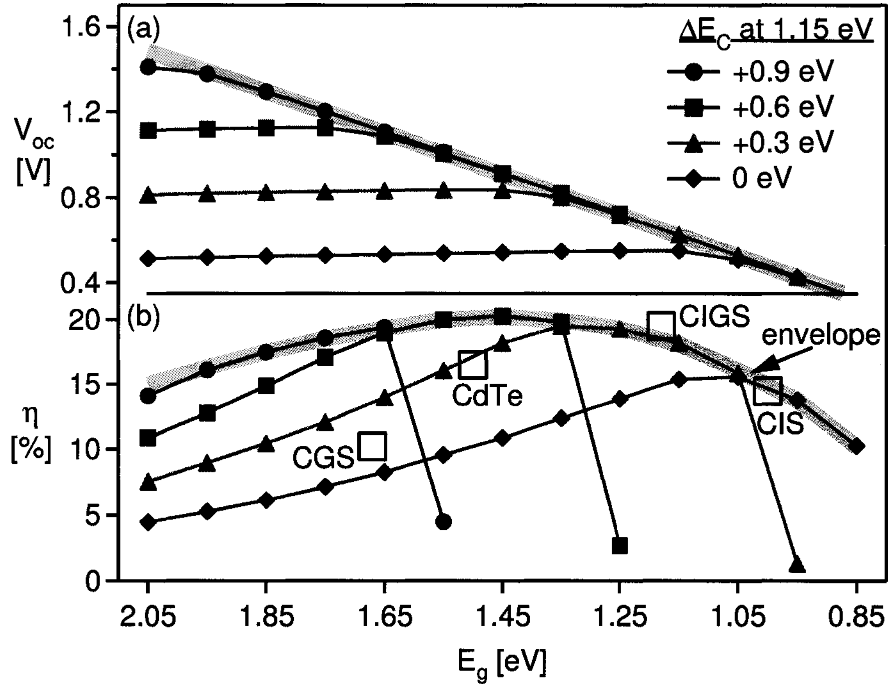

Figure 4.16: V_{oc} and η with different band alignments. The +0.3 V curve corresponds to the CdS/CIGS interface baseline case (IF-BL). Details will vary with choice of parameters. Highest reported cell efficiencies (open squares) follow the predicted efficiencies.

cause the sharp efficiency drop on the lower band-gap side for high-offset models.

Calculations assuming a fixed band offset of +0.2 eV for all absorber band-gaps form an upper envelope of the previous results (thick line in Fig. 4.16[b]). The highest efficiency in this envelope is 20.2%, which occurs near 1.45 eV. This curve is a quite general statement for CIGS thin-film solar cells assuming a film quality similar to what has been shown in record cells. Possible pathways to exceed these predicted efficiency limits are the application of non-uniform absorber materials ("grading"), discussed in Sect. 4.1, but these benefits are predicted to be small. Other improvements beyond the green envelope curve require improvements in material quality (lower defects) or new approaches that have not yet been considered.

The highest experimental efficiencies for CdS/CIS [99], CdS/CIGS [27], CdS/CGS [100], and CdS/CdTe [19] solar cells are shown for comparison with the modeling calculations (open squares). Except for the CdS/CGS solar cell, the record efficiencies all lie on the +0.3 eV curve, which was used as the CBO in the previous calculations for the CdS/CIGS

Reproduced with permission of the copyright owner. Further reproduction prohibited without permission.

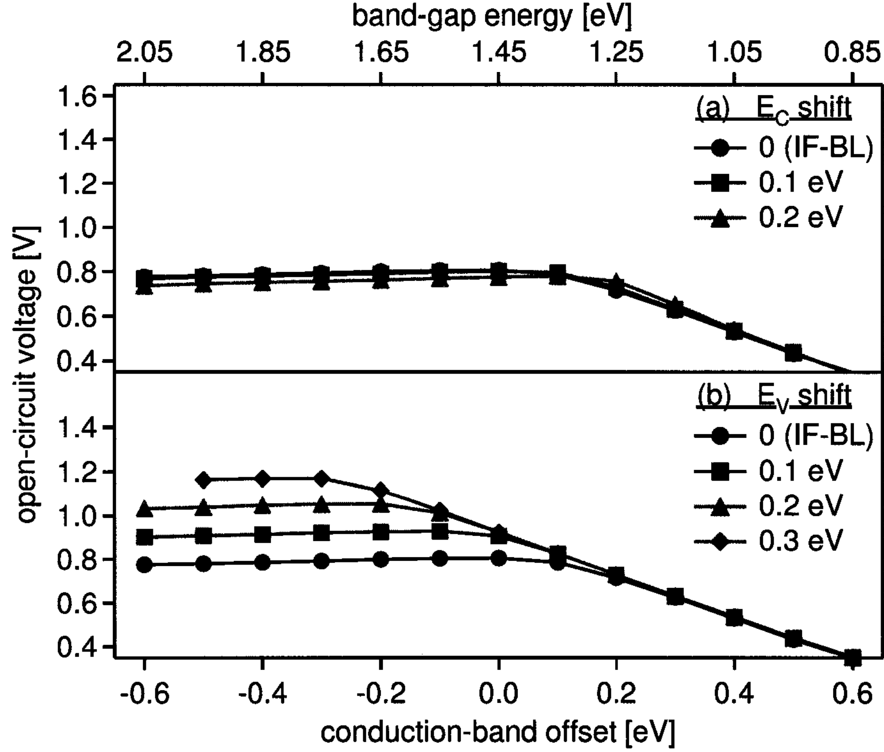

Figure 4.17: Band gap widening in the (a) conduction band or (b) valence band.

band offset. For the CdS/CGS system, efficiencies up to 14% are predicted, if a CGS film with comparable quality to CIS films can be grown. An alternative window with an appropriate offset, increases the highest predicted CGS efficiency above 19%.

4.2.5 Surface modifications

The band gap approaching the surface of a CIGS absorber is often different from the bulk. Typical examples are copper-poor surface phases (e.g., $Cu(In,Ga)_3Se_5$), which shift the valence band downwards [29] or intentional band-gap grading (e.g., increasing Ga/In ratio towards the junction, which shifts the conduction band upwards). Calculations were performed starting from the IF-BL assuming a surface phase that has (1) 100 nm thickness, (2) a band gap increased by ΔE = 0.1, 0.2, or 0.3 eV in either the conduction or the valence band, (3) optical absorption shifted according to ΔE, and (4) otherwise the properties of the bulk material. J_{sc} and FF results are unchanged. V_{oc} for all band gaps is shown in Fig. 4.17(a) for conduction-band widening and (b) for valence-band widening. The results are

Reproduced with permission of the copyright owner. Further reproduction prohibited without permission.

nearly unaffected if the widening occurs in the conduction band and, hence, the introduction of Ga/(Ga+In) grading (Sect. 4.1) is unlikely to improve the device performance, if interface recombination is the limiting process. Valence-band widening, however, leads to a depletion of holes at the interface that directly affects V_{oc}. It is apparent from these results that the hole concentration is the recombination-limiting parameter and V_{oc} is limited to voltages at which sufficient holes are supplied to the interface. This is in good agreement with the analytical findings that the valence-band position at the interface determines the voltage limitation [96] and that holes are the minority carrier at the interface for a n^+p junction [101].

4.2.6 Fermi-level pinning

A sufficiently high number of charged defects at the CdS/CIGS interface (10^{14} cm^{-2} are used in the simulation) will pin the Fermi level at the interface. Interface defects are largely unidentified for CdS/CIGS solar cells. Heath et al. [37] give a broad introduction into capacitance related defect analysis, and their results for CIGS solar cells suggest that the dominating defect response is a bulk defect level and not related to interface states. On the other hand, there is some earlier evidence of surface and interface defects (e.g., anion vacancies [102]). The question to whether interface states are present in substantial densities to cause pinning of the Fermi-level has not been answered. Recent first-principles calculations by Zhao et al. [103] investigated the doping limits of $CuInSe_2$ and $CuGaSe_2$. Their findings suggest that wider-band-gap materials are incapable of achieving n-type doping, as a Cu vacancy forms which leads to a compensation of shallow donor levels. Similarly, such compensating defects could pin the Fermi-level at the CdS/CIGS interface.

Pinning defects are introduced into the model with very small capture cross sections to decouple pinning from recombination. Acceptor states at a fixed distance above the CIGS valence band (0–1 eV) were found to reduce the depletion width. In this case, V_{oc}-limitations always occur, and no overall efficiency gain is achieved. Donor states, however, can increase the depletion width, and representative results are shown in Fig. 4.18. Donors a fixed distance above the CIGS valence band (shown in Fig. 4.18 for 1.4 eV above E_V) increase the inversion, reduce the hole concentration, and increase the V_{oc} limit by about

Reproduced with permission of the copyright owner. Further reproduction prohibited without permission.

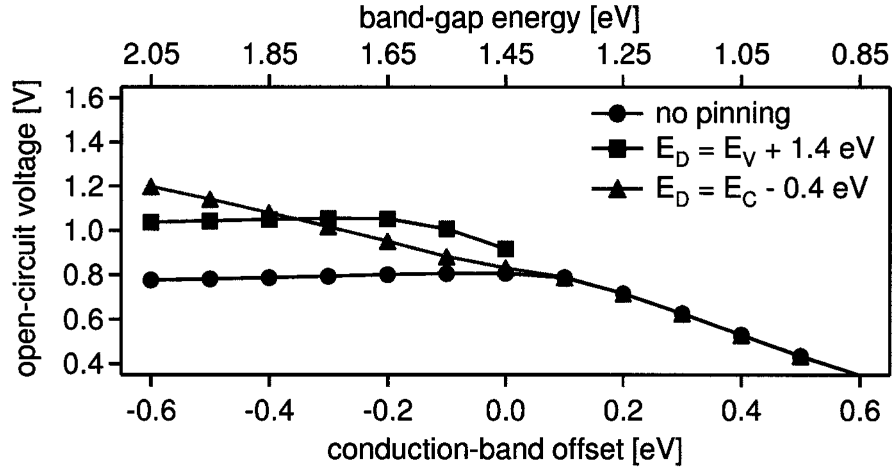

Figure 4.18: Pinning of the Fermi level by donor (D) interface states. The defects are located at a fixed distance above the valence band or below the conduction band.

0.2 V. Donors a fixed distance below the CIGS conduction band (shown for 0.4 eV below E_C) couple the hole depletion to the band-gap increase, and V_{oc} increases proportional to the band gap, but is slightly lower than for the interface-recombination free baseline (Fig. 4.13).

4.2.7 Summary

Inclusion of interface recombination into the baseline model ($E_g = 1.15$ eV, $\Delta E_C = 0.3$ eV) shows that under baseline conditions, interface recombination is entirely negligible, and therefore, it can be safely omitted in many device models (e.g., Sect. 4.1 and 4.3). However, if wider band-gap energies are considered, the open-circuit voltage has a limiting value independent of the absorber band gap for negative conduction-band offsets, in good agreement with a number of experiments. The voltage limitation should be addressable by appropriate matching of window and absorber to preserve a favorable offset. Efficiency limits have been calculated for all values of E_g and for certain alternative buffers, but also under the assumption of being able to establish a favorable CBO for every E_g.

The voltage situation also improves if the band gap widens in the valence band toward the interface, or if pinning states increase the depletion width. Both clearly indicate that the hole concentration is the limiting, voltage-modulated parameter that determines V_{oc}. Although details may change with variations in some parameters of calculations or

Reproduced with permission of the copyright owner. Further reproduction prohibited without permission.

experiments, the basic concept of an upper limit for V_{oc} independent of E_g appears to be a general characteristic. These results are suggestive that the typical window/buffer layer materials for low band gap CIGS materials will not allow high device efficiencies for wide-band-gap CIGS. Even if all other problems could be overcome, interface recombination will establish a performance limit unless the CBO is modified. To address these difficulties, the exploration of alternative window materials or of CIGS surface modification is recommended.

4.3 Photoconductive window and buffer layers

Experimental and simulation results presented in this section were part of the M.S. thesis of M. Gloeckler [60]. Selected data is reproduced to complete the coverage of 1D simulations of CIGS solar cells and to allow for additional discussion.

CIGS solar cells often show a failure of light/dark superposition of their current-voltage curves and such failure generally becomes more pronounced at lower temperatures. J-V measurements under red light may also show an additional distortion that indicates a dependence of the distortion on the CdS buffer layer. The proposed explanation is that a secondary barrier results from the conduction-band offset (CBO) between CIGS and the commonly employed CdS buffer layer. The secondary barrier is modified by photo-induced changes in trap occupancy in the CdS layer. Numerical modeling of the proposed explanation gives a very good fit to measured light and dark J-V curves over a wide temperature range.

4.3.1 Review

Well-behaved solar cells can usually be described by the diode equation and the assumption of a constant light generated current J_L (Eq. 2.10). Under this assumption, dark and light curves do not cross each other. However, in CdS/CIS and some CdS/CIGS solar cells, cross-over of light and dark J-V curves is frequently observed [104]. One possible cause of cross-over is a voltage dependence of the light generated current, $J_L(V)$, which

Reproduced with permission of the copyright owner. Further reproduction prohibited without permission.

is often associated with poor material quality. This has been studied thoroughly and is often encountered in a-Si and some CdTe solar cells [41, 105]. It is very unlikely, however, to explain the majority of results seen in CdS/CIGS solar cells, since these distortions are observed in low and high quality solar cells and they are qualitatively not compatible with a $J_L(V)$ mechanism. The cross-over observed in CdS/CIGS solar cells is different in nature, in that while the light J-V curves are well-behaved, the dark J-V curves are shifted to higher voltages and, in extreme cases, a strongly non-exponential behavior in the power quadrant of the J-V plot is observed. Additionally, these distortions are enhanced by measurements under red-light illumination (omitting photons with $h\nu > E_g^{CdS}$); this feature has been christened the "red kink" due to its wavelength dependence and intensely studied [104, 106–111]. Although there is not unanimity on its cause, most works explain these distortions following the model provided by Eisgruber et al. [107], which will be briefly reviewed in the course of the discussion.

"Photo-doping"

At the core of the observed effects lies the tendency of the wide-band-gap semiconductor CdS to self-compensate [17, 112]. This leads in general to strong photoconductivity, which can be either directly observed [113] or indirectly through the changes it causes in device performance. The increase in free carriers upon illumination is much greater than the photoconductivity expected by the photogenerated carriers alone, which suggests that charge trapping into deep levels is involved. Quantitative models typically assume a high number of shallow donor levels and a similarly high number of deep acceptor levels in the CdS material (e.g., discussed in Ref. [60, 114]). Agostinelli et al. [115] used the term "photo-doping" to express the effective increase in free carriers by illumination and discussed possible changes this could cause in J-V curves. A number of papers also investigated the influence of CdS photoconductivity on quantum efficiency measurements [116–118], summarized in Ref. [36]. The qualitative change to the band structure is shown in Fig. 4.19. Free electrons are trapped by the deep acceptor levels in the dark. Under illumination, these carriers are released and the n-type character of the CdS layer increases, which causes a downshift of the conduction-band minimum.

Reproduced with permission of the copyright owner. Further reproduction prohibited without permission.

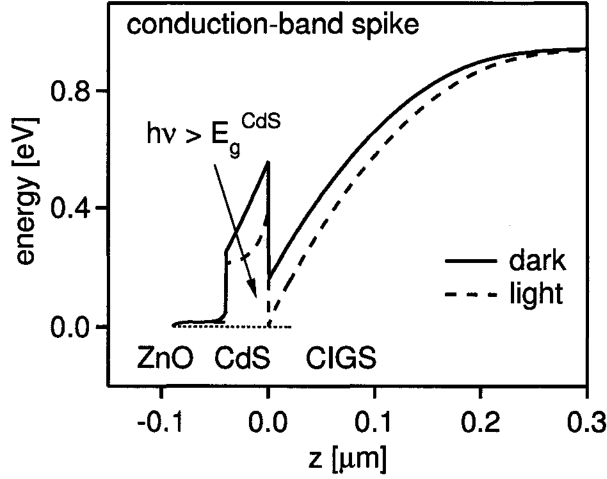

Figure 4.19: Conduction-band lowering due to the "photo-doping" in CdS.

4.3.2 *J-V cross-over*

Samples were provided by the Institute of Energy Conversion, University of Delaware. *J-V* results showed a cross-over of the light and dark curves. *J-V* measurements taken over a range of temperatures revealed a voltage progression of the dark curves of -3.3 mV/K, whereas V_{oc} progressed at a typical rate of -1.9 mV/K. The voltage progression for the dark curves was evaluated at a current density equal to the short-circuit current density J_{sc}. Therefore, not only did a cross-over exist at room temperature, but it also become stronger at lower temperatures. QE data suggests a band gap of about 1.12 eV for the samples studied.

The baseline case (Sect. 3.2.1), is able to reproduce the experimental data after the following adjustments have been made (BL values in parentheses): CdS thickness 40 nm (50 nm), CIGS band gap 1.12 eV (1.15 eV), and conduction-band offset $\Delta E_C = 0.4$ eV (0.3 eV) at the CdS/CIGS interface. These changes were made to match the experimental device and only the ΔE_C parameter was used as a fitting parameter.

Experimental and simulated *J-V* results are shown in Fig. 4.20(a) and (b) for light and dark conditions, respectively, and at T = 238 K, 268 K, and 298 K. The light curves are reproduced in 4.20(b) with dashed lines to visualize the cross-over of dark and light curves. The fits show the correct temperature progression in the light and dark.

The explanation for this behavior is found in the spike barrier of "considerable height"

Reproduced with permission of the copyright owner. Further reproduction prohibited without permission.

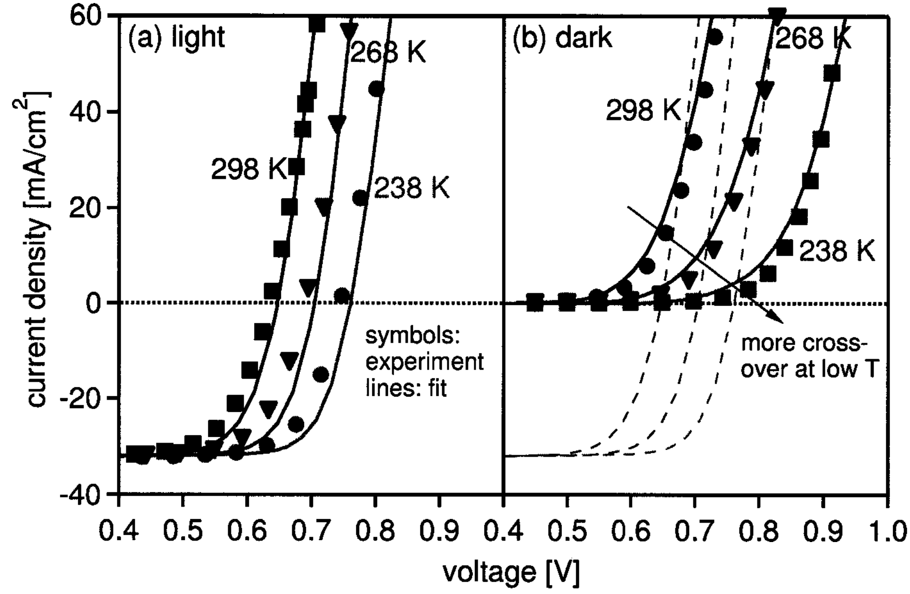

Figure 4.20: Comparison of (a) light and (b) dark *J-V* curves from experiment and simulation at three temperatures. The cross-over of dark and light *J-V* curves shown in (b) increases at lower temperature.

caused by the large conduction-band offset. A brief review of the transport mechanism will allow to specify a quantified meaning of "considerable height," before the model that resulted in the best fit to the experimental data is analyzed.

Current restriction by the conduction-band spike

Assuming thermionic emission transport across the interface [15], electron current across the conduction-band spike is limited to

$$J_n = \int_{E_{fn}+\phi}^{\infty} q \cdot v_x \cdot dn \simeq A^* T^2 e^{-\phi/kT}. \tag{4.6}$$

$A^* = (4\pi q m^* k^2/h^3)$ is the Richardson constant and ϕ is the barrier height; in the case under consideration, $\phi = E_C$ - E_{fn}. According to Eq. 4.6, only carriers in conduction-band states contribute to the electron current. Furthermore, in the absence of electric fields, the carrier transport is limited by the thermal velocity of carriers ($\sim 10^7$ cm/s). Hole currents are negligible because the large valence-band offsets at the ZnO/CdS and CdS/CIGS interfaces prevent any hole flow toward the front contact.

Reproduced with permission of the copyright owner. Further reproduction prohibited without permission.

Equation 4.6 can be rearranged to describe the minimum barrier height necessary for conduction of current J:

$$\phi = E_C - E_{fn} = kT \cdot ln\left(\frac{A^*T^2}{|J|}\right) \tag{4.7}$$

For typical values of N_C and a current of $J \sim J_{sc}$, this requires that $E_C - E_{fn} < 0.47$ eV. Note that Eq. 4.7 is independent of the current direction. In the power quadrant of the J-V plot (V > 0, $J < 0$), $|J|$ is always less than J_{sc}, but for positive voltages, J can be either positive or negative and can be limited in either direction.

With this general understanding, the J-V results (Fig. 4.20) are interpreted. Figure 4.21 shows the conduction band and electron quasi-Fermi level in the dark and under illumination and at zero and forward bias:

(a) V = 0 V, dark: the heavily compensated CdS is depleted; ϕ is large, but since the net current across the barrier is zero, the barrier is inactive.

(b) V = 0 V, light: illumination lowers the CdS conduction band, the barrier is significantly reduced, $\phi < 0.47$ eV, and current, $J < 0$, can flow.

(c) V = 0.7 V, dark: the barrier is high, but the applied external bias allows for some current flow across the spike barrier (electrons travel from left to right); this is achieved at the cost of a small voltage drop across the CdS, labeled as ΔV_{CdS}; ΔV_{CdS} represents the shift of the dark curve with respect to the light curve as shown in Fig. 4.20.

(d) V = 0.7 V, light: illumination leads to photo-doping; the barrier is lowered and current, $J > 0$, can flow.

As the carrier concentration in any semiconductor is strongly affected by the temperature T, so is the blocking qualities of the spike barrier. At lower temperatures, the blocking for the same current flow will occur at smaller barrier heights ϕ (Eq. 4.7), and in return, larger voltage drops ΔV_{CdS} are necessary (more shift in dark J-V, hence, more cross-over at low T, Fig. 4.20).

Reproduced with permission of the copyright owner. Further reproduction prohibited without permission.

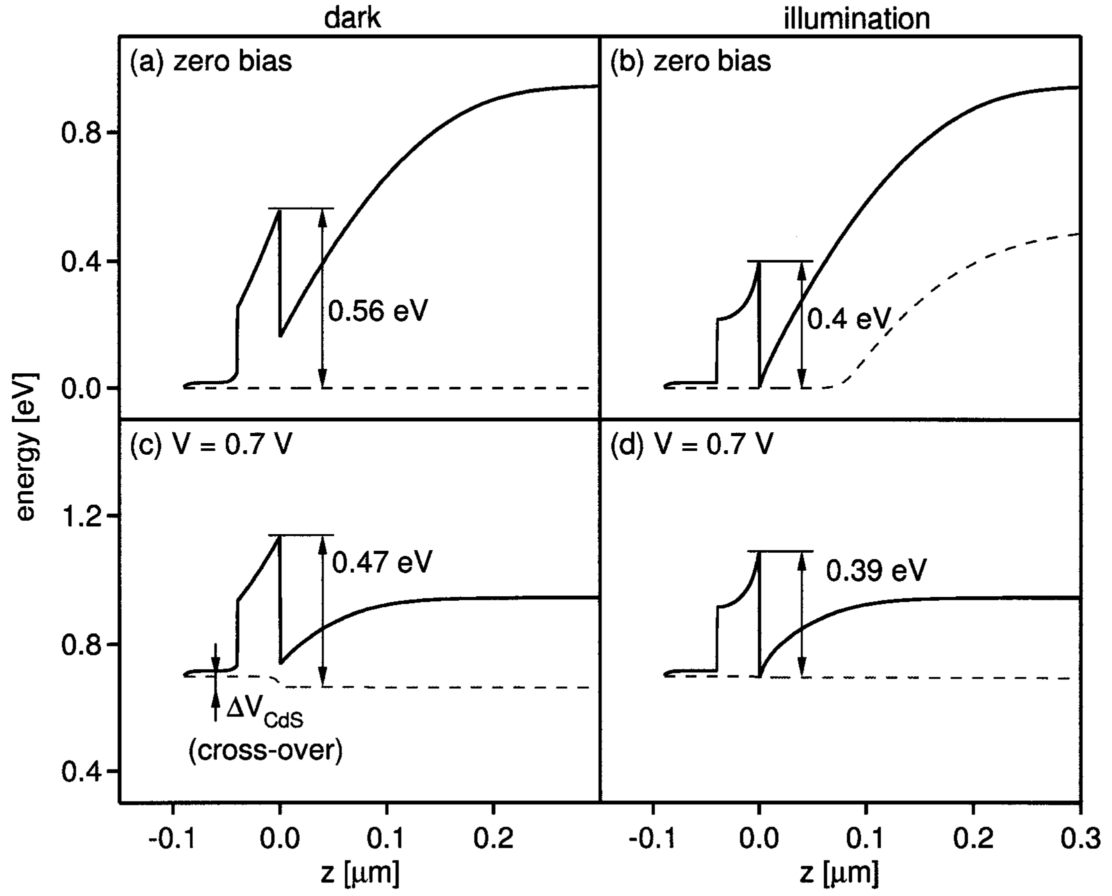

Figure 4.21: Conduction band and quasi-Fermi level for the device model in the dark (left) and under illumination (right). Only in the dark and under forward bias (c), is the barrier high enough to restrict current flow.

Earlier proposed explanations [60, 104, 114] emphasized the relative position of the conduction-band spike with respect to the bulk conduction band of the absorber layer. This phenomenological description is correct, yet it distracts from the actual cause of the effect. The similarity in the two descriptions can be seen considering a typical device: the p-type bulk conduction band is located roughly 0.9 eV above the hole quasi-Fermi level; further considering that E_{fn} and E_{fp} are split by the applied bias V, blocking that occurs at operating voltages $V > 0.4$ V implies that the spike (~ 0.5 eV above E_{fn}) is approximately at the same energetic level as the bulk CIGS.

Reproduced with permission of the copyright owner. Further reproduction prohibited without permission.

4.3.3 "Red kink"

From the previous discussion it is apparent that the distance from the highest point in the spike barrier to the electron quasi-Fermi level determines whether the *J*-*V* curve is distorted. This distance is influenced by many parameters, such as CdS thickness [109], ΔE_C at CdS/CIGS interface, doping and compensation level in CdS [110], the presence and thickness of intrinsic ZnO layers, and others. In a first-order approximation, all of these parameters reduce to the key value, which is the barrier height ϕ as defined above.

Smaller and larger barrier heights are investigated by varying the conduction-band offset at the CdS/CIGS interface, shown in Fig. 4.22 for ΔE_C = 0.3, 0.4, 0.45, and 0.5 eV. The *J*-*V* response is calculated in the dark, under normal white light, and under monochromatic "red light" illumination of intensity necessary to achieve the same photocurrent. The latter leads to absorption and photogeneration in the CIGS, but not in the photoconductive CdS layer.

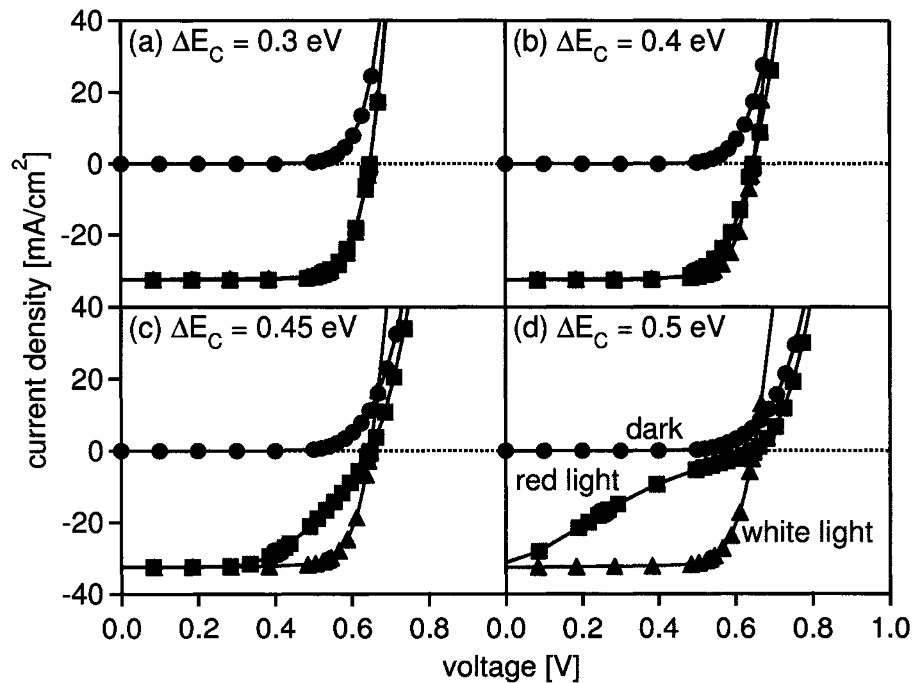

Figure 4.22: Current-voltage curves calculated in the dark and under red and white light illumination with increasing conduction-band offset. Larger offsets, cause a higher barrier in the conduction band and lead to current blockage for $\Delta E_C > 0.4$ eV. White light lowers the barrier by photo-doping of the CdS layer.

Reproduced with permission of the copyright owner. Further reproduction prohibited without permission.

(a) $\Delta E_C = 0.3$ eV: ϕ is small and the J-V curves show no anomalies.

(b) $\Delta E_C = 0.4$ eV: ϕ approaches the limiting value of 0.47 eV in the dark and under red light. A weak cross-over between white and dark J-V curves is observed. The red curve also indicates a small current restriction, because a small voltage loss (appears like a series resistance) is necessary for current transport across the barrier.

(c) $\Delta E_C = 0.45$ eV: ϕ is substantial in the dark and under red illumination. White light illumination reduces the barrier and, therefore, a strong cross-over is seen. Substantial voltage drop, ΔV_{CdS}, across the CdS is necessary to ensure current transport. This voltage drop is non-linear to the current response and can not be interpreted as series resistance.

(d) $\Delta E_C = 0.5$ eV: Large ϕ in the dark and under red light leads to a strong current blockage and strong cross-over. Fig. 4.22 is typical for CdS/CIS cells that exhibit red-kink behavior [104].

It has to be noted, that practically all configurations shown in Fig. 4.22 have very similar white light J-V curves and, therefore, one might readily conclude that spike barriers are of little interest for practical solar-cell applications. However, under low light illumination and particularly for the application in thin-film tandem solar cells [119], a "red light" illumination might reasonably well describe the true operating conditions. Hence, understanding and reducing these current blocking mechanism becomes of considerable interest.

The relation between the J-V distortion under red-light and the effect on the bands is discussed in more detail for the case $\Delta E_C = 0.45$ eV. The J-V curve is reproduced in Fig. 4.23 and shows the CdS voltage loss ΔV_{CdS}, which is positive for $J > 0$ and negative for $J < 0$. ΔV_{CdS} is noted in Fig. 4.23 for two current values that correspond to cell voltages of $V = 0.5$ V and 0.75 V of the red light curve. The conduction band and electron quasi-Fermi level under these conditions for white and red light illumination are shown in Fig. 4.24.

Under white light illumination and $V = 0.5$ V, the barrier $\phi < 0.47$ eV and the light generated current ($\sim$32 mA/cm^2) can cross the barrier by thermionic emission. Under red light illumination (Fig. 4.24[b]), the barrier restricts the current and an additional voltage

Reproduced with permission of the copyright owner. Further reproduction prohibited without permission.

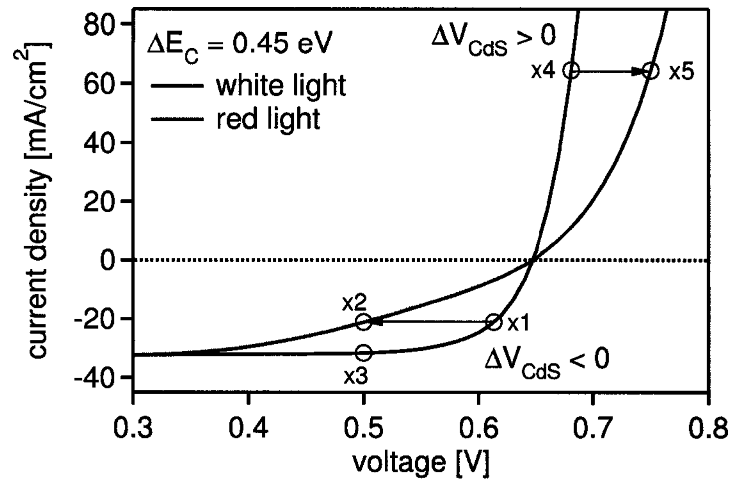

Figure 4.23: J-V curve for $\Delta E_C = 0.45$ eV under white and red light. The voltage loss, ΔV_{oc}, is positive or negative depending on the net current flow. The description of the barrier effect in terms of a voltage shift (x1 to x2) and (x4 to x5) is general and applies for voltages both above and below V_{oc}.

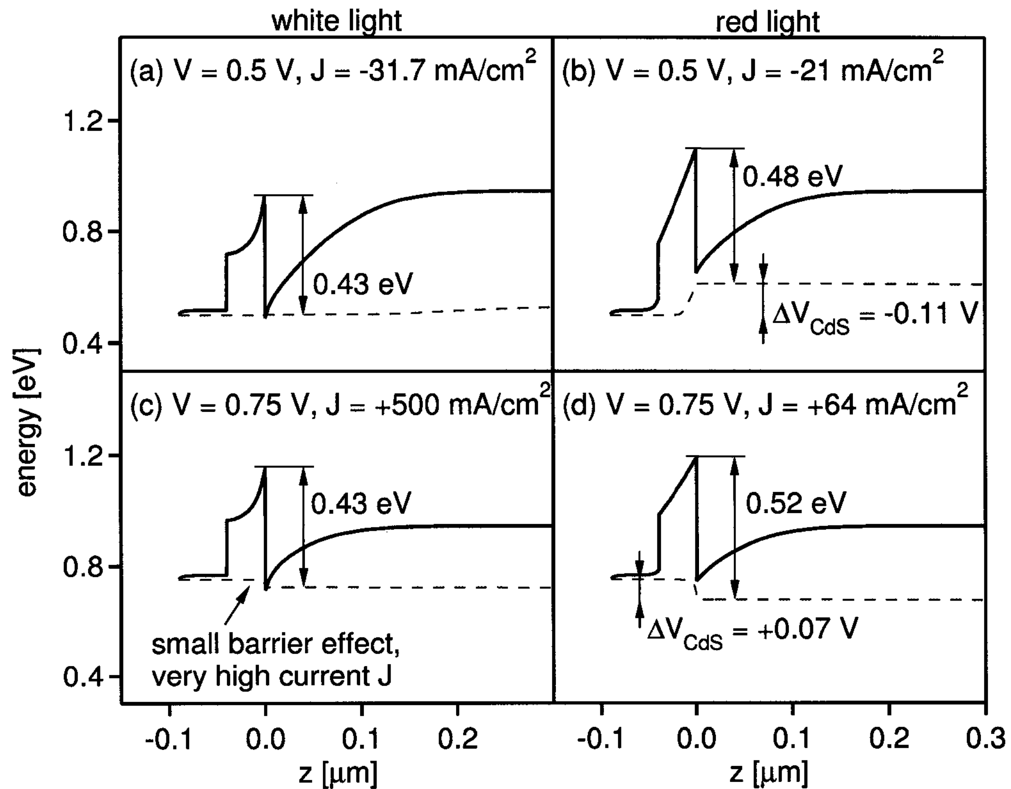

Figure 4.24: Bands for the case of $\Delta E_C = 0.45$ eV. White light alleviates the barrier effect, but under far forward bias, the current might still be limited (c). Under red light, the secondary barrier changes the voltage that is applied to the main junction in the positive (b) or negative (d) direction.

Reproduced with permission of the copyright owner. Further reproduction prohibited without permission.

loss across the CdS is necessary. This effectively places the main junction under additional forward bias ΔV_{CdS} and, hence, increased forward recombination occurs. Pictorially, this is represented by the shift of point x1 to x2 in Fig. 4.23. A qualitative description of the phenomena is to state that some current is blocked, which is more closely described by a shift from point x3 to x2 in Fig. 4.23. Both descriptions have their merit and can be similarly useful.

Under higher forward voltage $V = 0.75$ V (above V_{oc}), the net current across the junction is positive. White illumination reduces the barrier and allows for well-behaved performance. However, under such high voltages, the current through the solar cell and over the barrier will become very high (500 mA/cm^2 for the situation depicted in Fig. 4.24[c]) and once again the barrier becomes limiting ($\phi \sim 0.4$ eV limits currents above 500 mA/cm^2, Eq. 4.7). In red light (Fig. 4.24[d]), the barrier is not lowered due to illumination and a substantially higher voltage loss ΔV_{CdS} is necessary for transport across the barrier. This effectively lowers the voltage bias applied to the main junction and therefore the total current flow (shift from point x4 to x5 in Fig. 4.24[d]).

4.3.4 Summary

The baseline case reproduces, after minor modifications, the experimental results over a broad temperature range. A detailed analysis of the transport mechanism identified the barrier height $\phi = E_C - E_{fn}$ as the key parameter and showed that at room temperature well-behaved solar-cell performance can be expected if $\phi < 0.47$ eV. A large barrier will lead to small non-superposition of dark and light *J-V* curves as they were observed on the experimental devices. Under red light illumination, which may be of significant interest in the application of CIS solar cells in a tandem structure, *J-V* curves are much more readily distorted, since the restricted spectrum does not activate the photoconductivity in the CdS buffer. Smaller barriers may be mis-interpreted as a series resistance, but for significant barriers the voltage loss across the CdS becomes highly non-linear and results in strong distortions of the *J-V* curves, historically known as the red kink. This general treatment can explain all features observed, independent of any specific assumptions on device materials or configuration.

Reproduced with permission of the copyright owner. Further reproduction prohibited without permission.

Chapter 5

Advanced two-dimensional simulations: grain boundaries

In thin-film solar cells, lattice mismatch and defect gettering at inter-grain interfaces ("grain boundaries") are generally expected to create additional defect levels within the forbidden gap and, hence, cause additional recombination through such grain boundary (GB) states (for a general review on GBs see Refs. [17] and [120]). Polycrystalline CIGS solar cells, however, have achieved efficiencies close to 20% [25], which is higher than any other polycrystalline thin-film technology [121], and it appears that grain boundaries in CIGS solar cells are benign, or maybe even beneficial, to solar-cell performance.

Typical CIGS thin-films (Sect. 2.1.4) are only a few micrometers thick and average grain sizes are similar, such that "columnar" growth is typically achieved (Fig. 2.4). This work studies GBs in CIGS solar cells with numerical simulations in two dimensions and evaluates a number of possible scenarios: (1) charge-free "horizontal" GB, (2) charge-free "columnar" GB, (3) minority-electron repulsive band-bending, (4) majority-hole attractive band-bending, (5) downshift of the valence-band maximum at the GB, and (6) combinations of cases 4 and 5. For each of these scenarios, recombination in the quasi-neutral bulk of a solar cell, as well as recombination in the space-charge region is considered. It is concluded that the valence-band downshift is the likely explanation for high conversion efficiencies found in CIGS solar cells and their forgiving nature with respect to GBs.

Reproduced with permission of the copyright owner. Further reproduction prohibited without permission.

Collaborators have simulated the influence of GBs on photoluminescence, near-field scanning microscopy, and electron beam induced current experiments [122]. These results support the general conclusion found in this work that large hole-repulsive band-bending is unlikely to be present in highly-efficient solar cells.

5.1 Review

For decades, grain boundaries in polycrystalline materials have been studied intensely. In the mid-80's, polycrystalline silicon (PX-Si) was the first polycrystalline material to reach commercialization as a solar-cell material, and at the same time studies quantified the effects of GB recombination by means of analytical models. With the availability of more computing power, the PX-Si problem was more accurately addressed using numerical simulations. Some of these results are briefly reviewed, and aspects that apply to the problem of Cu(In,Ga)Se_2 solar cells are highlighted. However, one must consider that CIGS substantially differs from PX-Si: CIGS has a direct optical band-gap, which can vary from 1.04–1.67 eV with Ga content, and it depends on intrinsic defects and stoichiometric deviations to achieve doping. Furthermore, CIGS thin-films are typically grown on soda-lime glass or flexible substrates and have much smaller average grain sizes (~1 μm).

Experimentally, grain boundaries in Cu(In,Ga)Se_2 and CdTe solar cells have been only partially accessible due to the small average grain size (~1 μm) in comparison to the limited resolution of micro-characterization methods. As better instrumentation and processing control have become available, studies on solar-grade material have become more feasible, but have yielded controversial results.

5.1.1 Analytical and numerical models

Seto [123] proposed the presence of charged grain boundaries (majority repulsive) in PX-Si to explain the temperature dependence of the carrier mobility. Although this picture is widely accepted, no correlation between the proposed charged GBs and the performance of solar cells was given. Seto further identified an important criterion for charged defect levels at GBs: If the concentration of GB states $N_{gb} > N_A d_g$, where N_A is the shallow bulk dopant

Reproduced with permission of the copyright owner. Further reproduction prohibited without permission.

density and d_g the average distance between two adjacent columnar GBs (grain size), the bulk material will be depleted of free carriers. This establishes a barrier ϕ_{gb} at the GB

$$\phi_{gb} = q^2 d_g^2 N_A / 8\epsilon. \tag{5.1}$$

For the case that $N_{gb} < N_A d_g$, only part of the grain is depleted and the barrier height is found by integration of the Poisson equation to be

$$\phi_{gb} = q^2 N_{gb}^2 / 8\epsilon N_A. \tag{5.2}$$

Card and Yang [124] discussed the dynamics of charged GB states and concluded that under illumination the occupancy of these states adjusts to maximize GB recombination. The average reduction of the carrier lifetime by GB states can be estimated by the definition of an effective lifetime [124, 125] and this approach was used to calculate device performance as a function of grain size and other parameters for PX-Si. A similar approach will be discussed and used in Sect. 5.3.4 in comparison to the numerical model. Alternatively, a two- or three-dimensional analytical solution in the form of an infinite series can be derived [126–129]. Such solutions are limited to the quasi-neutral region (zero electric field) of the absorber material. Some authors have extended this approach to predict solar-cell performance [127, 128, 130], but charge trapping and trap dynamics were never incorporated. Analytical work by Green [131] showed that the collection efficiency within the space-charge region (SCR) is only marginally affected by columnar GBs, whereas GBs that are parallel to the junction can cause catastrophic current losses. Later work derived quite general bounds on GB recombination [132], which are discussed in Sect. 5.3.4. Edmiston *et al.* [133] used numerical simulations to discuss the effects of charged GB states in PX-Si solar cells and presented an improved analytical model describing the effective GB recombination velocity.

Numerical simulations find solutions to the two- or three-dimensional problem that can include charged trap levels and trap dynamics. The Poisson equation and the electron and hole continuity equations are solved subject to the boundary conditions. This has been

Reproduced with permission of the copyright owner. Further reproduction prohibited without permission.

done in the past for PX-Si solar cells [134–139]. Numerical as well as analytical approaches for PX-Si predict a strong detrimental effect of GB recombination, which is enhanced by the presence of small band-bending in the direction that attracts minority carriers.

Recent work by Taretto *et al.* [140] investigated grain boundaries in CIGS material with numerical simulations. These authors concluded that the GB recombination velocity must be less than 10^3 cm/s to allow for efficiencies around 19%, and that a shift in the valence-band energy results only in small improvements.

5.1.2 Micro- and macro-characterization of GBs

A number of studies have investigated GBs in CIGS films: Surface-Kelvin-Probe Microscopy (SKPM) on low-Ga content CIGS films determined a hole-repulsive band-bending of approximately 150 meV at GBs [141, 142]. The authors argued that since SKPM can only measure the potential variation at the surface, the band-bending in the bulk absorber may be larger and can assist in minority carrier collection. Studies on higher Ga-content samples [143], showed that no potential barrier at GBs was observable for $CuIn_{1-x}Ga_xSe_2$ with $x > 0.4$. Transport analysis on CGS samples ($x = 1$), however, have determined a potential barrier of 60–130 meV [144]. Sadewasser et al. [145] and Fuertes Marrón et al. [146] measured hole-repelling barriers with SKPM of about 100 meV on CGS materials and observed a reduction of this band-bending under illumination. For Cu-rich CGS samples, an electron-repelling barrier of 75 meV has also been reported [147].

First-principles calculations have predicted a downshift of the valence-band edge at grain boundaries that will repel holes without requiring electrically active defects [148]. This valence-band offset is predicted to be 0.2–0.4 eV in magnitude and localized to a very thin layer at the grain surface in which the surface reconstruction takes place. A closely related effect is the formation of Cu-poor "ordered defect compounds" that have been reported at the CIGS surface [50]. Recent experiments have shown that CIGS grain boundaries are similarly deficient in copper [149].

Reproduced with permission of the copyright owner. Further reproduction prohibited without permission.

5.2 Model description

The solar-cell model consists of window, buffer, and absorber layers and is implemented as 200-nm ZnO, 50-nm CdS, and 3-μm CIGS layers respectively, typical of CIGS solar cells. The model parameters for these layers are given in Table 3.2 (p. 31) and were discussed in Sect. 3.2 and Ref. [69]. The back-contact reflectivity was set to zero (baseline 0.8) for convenience, but J-V results are essentially independent of that value. Interface recombination at the CdS/CIGS interface is included, but, as it has been discussed in Sect. 4.2, the positive conduction-band offset suppresses the hole concentration at the CdS/CIGS interface and, hence, interface recombination is negligible. All layers have uniform band-gap energies vs. depth (no grading); laterally, the band gap varies for the cases that consider valence-band offsets at GBs (Sects. 5.5.1 and 5.5.2).

The numerical model is two dimensional, assuming the third dimension to be uniform. GBs are either perpendicular or parallel to the main junction, which will be referred to as "columnar" (Fig. 5.1[a]) or "horizontal" (Fig. 5.1[b]) GBs. The distance between two columnar GBs is 1 μm and the model consists either of one or two unit cells (Fig. 5.1[a] shows one unit cell). Grain boundaries are modeled by a thin (2 nm) layer located between two uniform regions of CIGS material, and the GB layer differs from the surrounding bulk

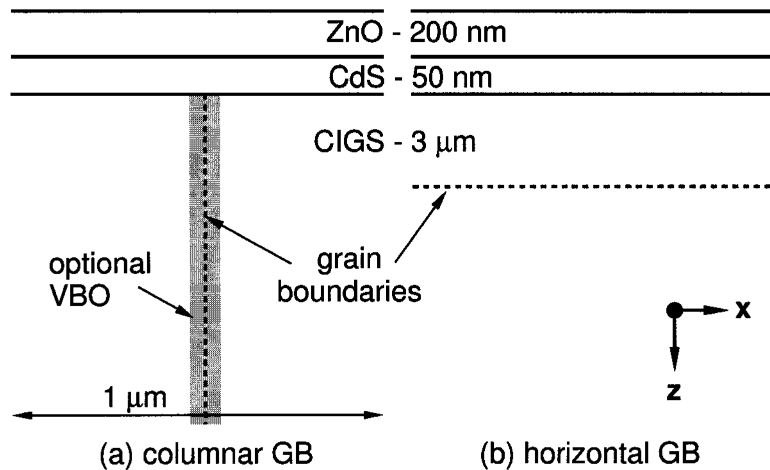

Figure 5.1: Schematic model configuration (not so scale) for (a) columnar GBs and (b) horizontal GBs. The x-axis is defined to be in the plane of the solar-cell layers and the z-axis normal to the plane.

Reproduced with permission of the copyright owner. Further reproduction prohibited without permission.

Table 5.1: Simulation GB parameters. GB defect density N_{gb}; defect peak-energy E_A and E_D; and capture cross-section σ. Subscript e/h refers to electron/hole properties.

CIGS grain-boundary defects	N_{gb} (cm^{-2})	E_A, E_D (eV)	$\sigma_e = \sigma_h$ (cm^2)
"Neutral" recombination center	10^3–10^8	mid-gap	10^{-8}
Donor (Sect. 5.4.2)	10^{11}–10^{12}	$E_C - 0.2eV$	10^{-18}
Acceptor (Sect. 5.4.3)	10^{11}–10^{13}	$E_V + 0.1eV$	10^{-18}

material only by the presence of additional defects; such models are often used to describe GBs [120]. The results are not sensitive to the width of the GB layer, and in fact, identical results were obtained using planar boundaries (thin-layer GBs of distinct width have some practical advantages).

GB input parameters (Table 5.1) and most results are expressed in terms of a planar boundary (i.e., "sheet" instead of "volume" density of trap levels). GB recombination is modeled by mid-gap states that are assigned a low density and a large capture cross-section ("Neutral" in Table 5.1). This choice dictates that these states are "neutral" in that the provided charge density is negligible compared to the bulk doping and no significant electrostatic potential difference is established; these neutral defects are included in all simulations. The magnitude of the GB recombination is expressed by the recombination velocity $S_{gb} = \sigma N_{gb} v_{th}$, where v_{th} is the thermal velocity of the carries ($\sim 10^7$ cm/s) and the other parameters are defined in Table 5.1. Charged defects with comparatively small capture cross-sections are used to introduce band up- or down-bending at the grain boundary. This choice of defect configuration is somewhat artificial, but allows the effects of recombination and band-bending to be decoupled and evaluated separately.

The simulations were performed with the software program DESSIS (Sect. 3.3) [48]. A customized mesh is applied to the one- or two-unit-cell configuration; this mesh typically contains 2,000–10,000 mesh points and is chosen to be denser in areas where parameters are expected to vary more rapidly, i.e., close to the junction, the CdS/CIGS interface, and the GBs. The meshing is illustrated in Fig. 5.2 for a two unit-cell model. The mesh was chosen dense enough that further increase in mesh lines leaves the outcome of the simulation unaltered within the necessary accuracy. Hetero-interfaces at the ZnO/CdS and CdS/CIGS interface and also the valence-band offsets considered in Sect. 5.5 are treated with special

Reproduced with permission of the copyright owner. Further reproduction prohibited without permission.

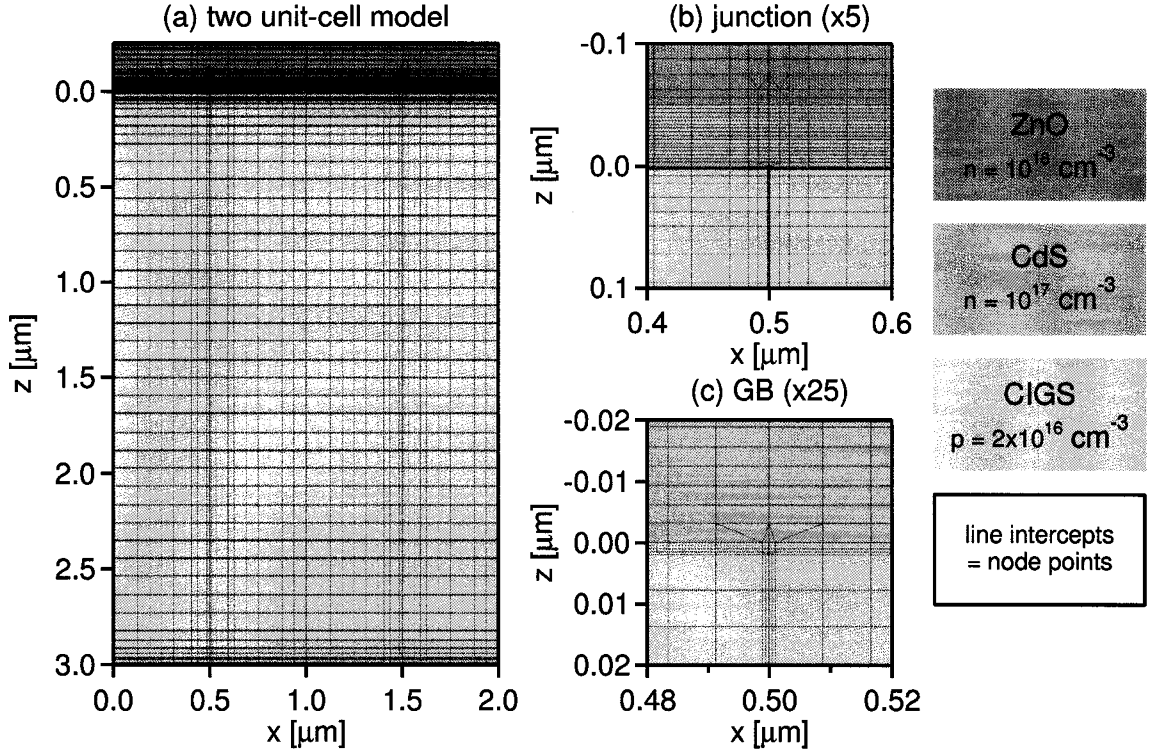

Figure 5.2: (a) Example of mesh configuration; black lines correspond to mesh lines. In the simulation, a solution is found for all points where the mesh lines intercept (node points). Higher densities of mesh lines are used (b) within the junction and (c) close to the GBs.

care through the definition of degenerate mesh points along these interfaces (two mesh points with the same coordinates, one belonging to each material) [48].

The reference performance given by a GB-free model ($S_{gb} = 0$) is identical to the one-dimensional baseline results (Sect. 3.2.1): open-circuit voltage $V_{oc} = 0.64$ V, short-cricuit current density $J_{sc} = 34.7$ mA/cm^2, fill factor FF = 79%, and efficiency $\eta = 17.6\%$. Diode analysis results in a diode saturation-current density $J_0 \simeq 2 \times 10^{-8}$ mA/cm^2 and a diode-quality factor near 1.2. All these characteristics are similar to properties of high-quality CIGS cells.

5.3 Neutral grain boundaries

Prior to investigating the effects of charged grain boundaries and compositional variations at GBs, the influence of GB recombination alone has to be considered. Although CIGS films

Reproduced with permission of the copyright owner. Further reproduction prohibited without permission.

show mostly columnar grain growth, particularly at the beginning of the growth, horizontal GBs do form (primarily towards the back contact of the device), and therefore both limiting cases of neutral horizontal and columnar GBs are considered. These calculations also establish a limit on the achievable device performance as a function of the GB recombination velocity, $\eta_{max}(S_{gb})$. In the more general case, including potentials or valence-band offsets at GBs, it is also often possible to establish a relation between the nominal S_{gb} (input parameter) and the effective GB recombination, S_{eff}, such that the same limit can be applied to these more general cases in terms of $\eta_{max}(S_{eff})$.

Further detailed analysis shows how different parts of columnar GBs affect the carrier collection and forward recombination and that for typical grain sizes found in CIGS materials, GB recombination might be indistinguishable from bulk recombination. This section closes by using the previously mentioned one and two-dimensional analytical solutions to find comparative solutions to the problem.

5.3.1 Horizontal grain boundaries

Simulations including horizontal GBs at a varying distance, z_{gb}, from the CdS/CIGS interface were performed. It has to be noted, however, that this model is somewhat artificial as it implies that a horizontal GB extends throughout the entire solar cell. However, much can be learned about how such horizontal GBs could cause *local* weak spots in thin-film solar cells. S_{gb} was chosen as 10^5 cm/s. Resulting J-V curves and J-V parameters are shown in Fig. 5.3.

Voltage losses are highest if the GB is located within the space-charge region, particularly if it is located at the point where $n \sim p$. This is in good agreement with analytical considerations [132]. The catastrophic J_{sc}-loss for GBs within the SCR predicted by Green [131] is not observed. This prediction was based on a circuit-equivalent model of the SCR that assumed an infinite GB recombination strength (zero-resistance shunt in the circuit-model). For moderate values of $S_{gb} = 10^5$ cm/s (Fig. 5.3), the effect on the current collection at zero voltage is small, and carrier transport across the GB is possible. If the grain boundary is located outside the SCR, J_{sc}, V_{oc}, and FF are only weakly (less than 5% relative) affected, and the net efficiency losses are minor.

Reproduced with permission of the copyright owner. Further reproduction prohibited without permission.

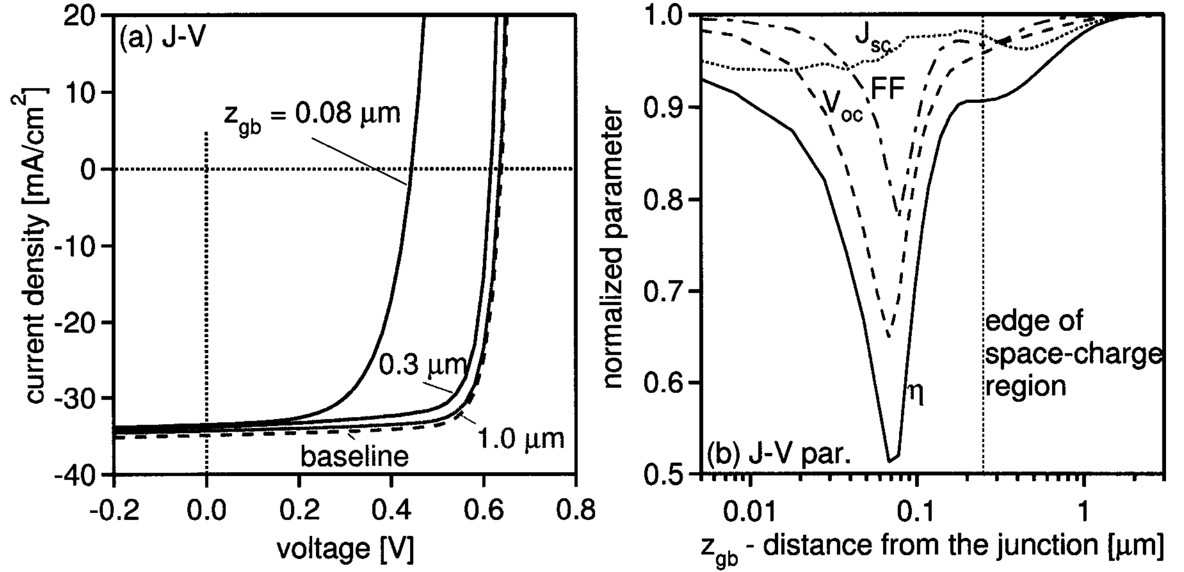

Figure 5.3: *J-V* performance with horizontal GBs at a distance z_{gb} from the CdS/CIGS interface. (a) *J-V* curves for selected values of z_{gb} and (b) *J-V* parameters.

The band diagram, carrier concentration, and recombination distribution is shown in Fig. 5.4 for $z_{gb} = 0.3$ μm. Horizontal GBs located in the quasi-neutral region, outside of the SCR, cause recombination of light generated electrons at a rate of $R_{gb} = \Delta n S_{gb}$. However, most of the light is generated within the first few tenths of a micron (Fig. 3.1) and, therefore, the effect on J_{sc} is weak for $z_{gb} > 0.3$ μm. Within the SCR, the recombination is small at zero bias as this region is depleted of carriers and the strong electric field sweeps light generated carriers out. Close to the SCR edge, minority carriers are also efficiently collected by diffusion into the SCR. Hence, in summary, the effect of horizontal GBs on current collection and J_{sc} is minor.

Under forward bias, Fig. 5.4(b), the recombination for horizontal GBs outside the SCR (as shown) is only weakly affected. However, as carriers are injected into the SCR by the applied bias, the typical high-recombination peak forms in the SCR and this recombination can be greatly enhanced, if the horizontal GB is located in the middle of the SCR around $z_{gb} \sim 0.1$ μm (not shown).

A number of techniques have been used to investigate lateral non-uniformities. From the above results, it can be predicted that a horizontal GB within the SCR, extending laterally over one or a few grains, can result in a local weak diodes (low V_{oc}) and shunting,

Reproduced with permission of the copyright owner. Further reproduction prohibited without permission.

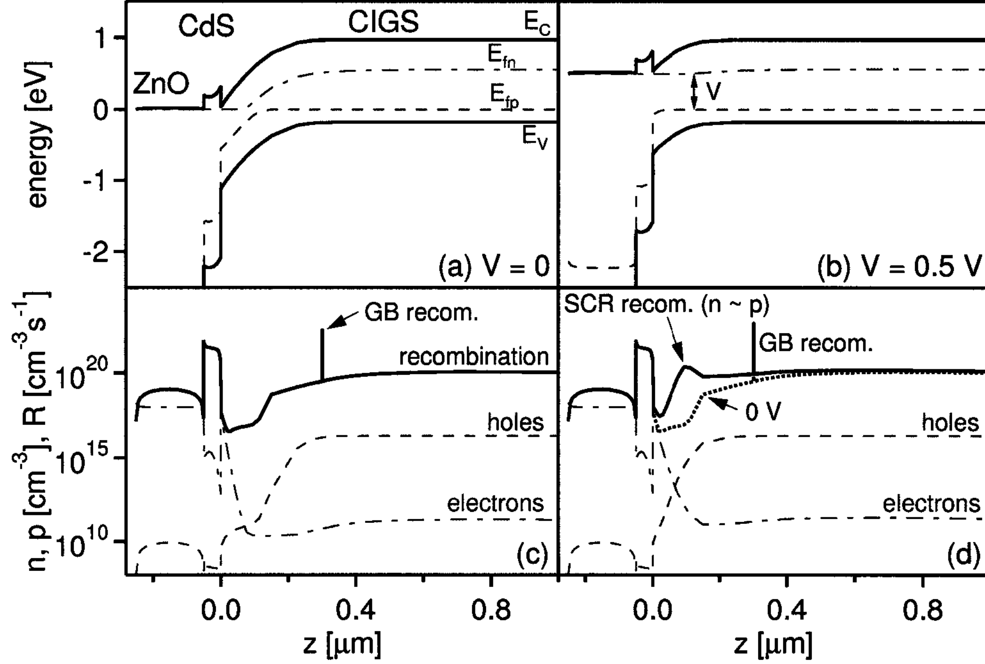

Figure 5.4: Conduction band, valence band, and electron and hole quasi-fermi level (top). Recombination rate and electron and hole density (bottom). (a, c) Zero bias. The electron density in the CIGS is greatly increased due to the one-sun illumination. The horizontal GB at $z_{gb} = 0.3\,\mu$m causes a recombination peak at the same location. (b, d) Forward bias $V = 0.5$ V. SCR recombination peak develops centered around $z \sim 0.1\,\mu$m.

as has been conceptually discussed by Karpov et al. [150]. CdTe solar cells, which are more likely to have horizontal GBs within the SCR due to the reversed growth process, often show such local weak spots by electroluminesence experiments [151]. Techniques that measure the collection efficiency, such as Laser-Beam-Induced-Current measurements [152], are insensitive to this type of micro-nonuniformity, because the current collection is only weakly affected by the presence of horizontal GBs.

5.3.2 Columnar grain boundaries

Columnar GBs with a grain size of 1 μm (model Fig. 5.1[a]) and $S_{gb} = 10^2$–10^7 cm/s are evaluated in this section. J-V and QE curves are shown in Fig. 5.5, performance parameters for the full range of S_{gb}, normalized to the GB-free model, are shown in Fig. 5.6.

CIGS is a direct band-gap material with very strong absorption and, hence, unlike Si solar cells, most of the light (> 85%) is absorbed in the narrow SCR. Therefore, J_{sc}-losses

Reproduced with permission of the copyright owner. Further reproduction prohibited without permission.

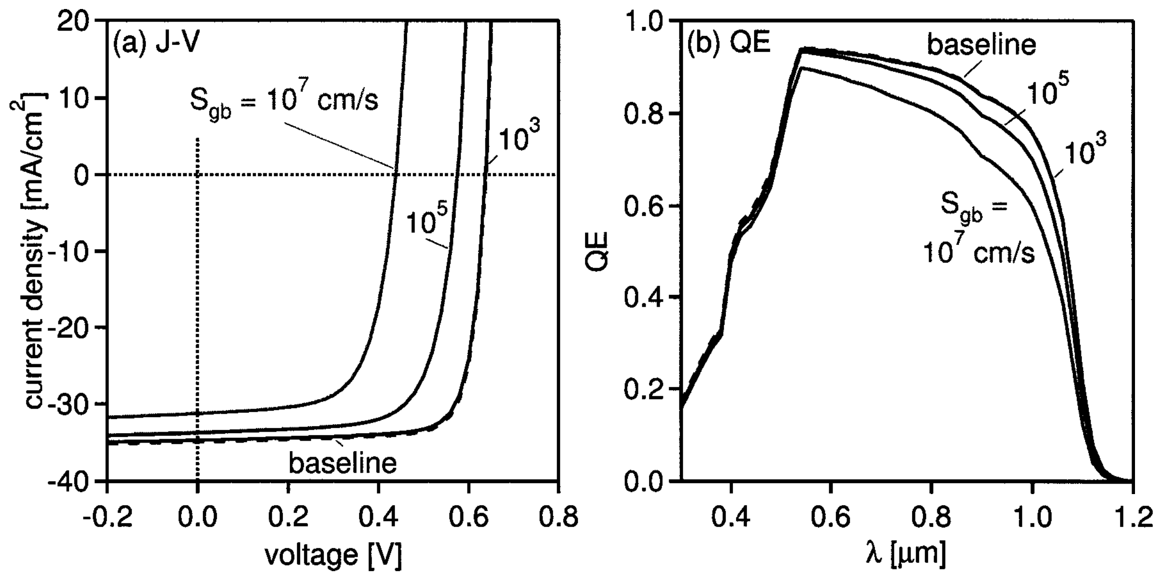

Figure 5.5: J-V and QE curves with columnar GBs for selected values of S_{gb}.

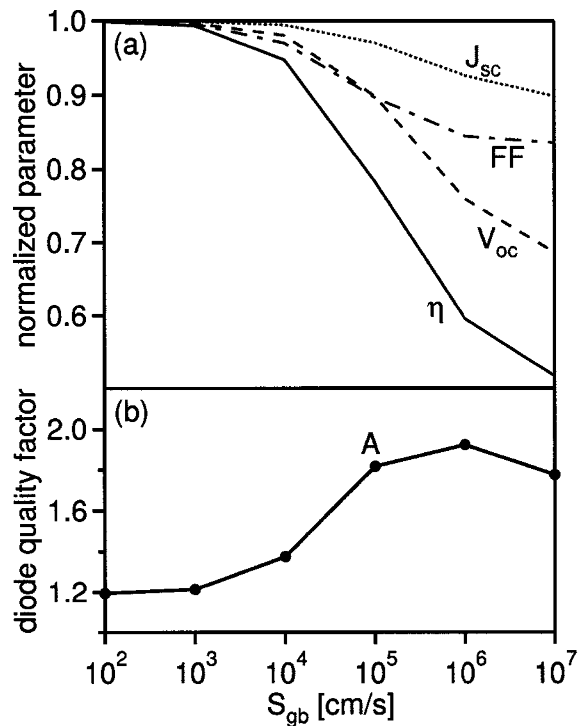

Figure 5.6: (a) J-V parameters for columnar GBs with S_{gb} = 10^2–10^7 cm/s. (b) Diode quality factor A.

Reproduced with permission of the copyright owner. Further reproduction prohibited without permission.

correlate to reductions in the long-wavelength quantum efficiency ($S_{gb} = 10^5$ cm/s in Fig. 5.5). This agrees well with analytical models that predict that the losses due to columnar GBs in the SCR should be negligible [131] and, hence, only deeply generated electron-hole pairs (corresponding to longer wavelength photons) should have an increased chance of recombination as S_{gb} increases. For very large values of S_{gb}, however, the transit time through the SCR (Sect. 5.3.4) becomes similar to the recombination lifetime and strongly absorbed blue light also shows lower QE ($S_{gb} = 10^7$ cm/s in Fig. 5.5).

V_{oc} decreases rapidly with increasing S_{gb} due to the strong recombination within the part of the GB that is located in the SCR. This is accompanied by a transition of the diode quality factor A from about 1.2 to 2 (Fig. 5.6[b]), as the dominant recombination path changes from the absorber bulk to the SCR. In comparison to the GB-free baseline (η = 17.6%), the effects of GB recombination are noticeable (loss of relative 5% or absolute 1%) once $S_{gb} \geq 10^4$ cm/s. This suggests that efficiencies of 17% or higher require some type of passivation, such that the effective GB recombination velocity is the order of 10^3 cm/s or less, in agreement with results of others [140].

The resulting carrier distribution throughout the two-dimensional model as well as carrier concentration and recombination profile at the grain boundary are shown in Fig. 5.7(a) at zero bias and 5.7(b) under 0.5 V forward bias ($S_{gb} = 10^5$ cm/s). For moderate values of S_{gb}, the carrier concentrations are constant across the GB. Very large S_{gb} (> 10^6 cm/s) results in a noticeable depletion of electrons at the GB, and, since this depletion cannot be considered in a one-dimensional model, "effective-lifetime" models overestimate GB recombination for high values of S_{gb}. This will be discussed in detail in Sect. 5.3.4. Recombination in forward bias occurs predominantly in the 0.25 μm-wide SCR, which is apparent from the narrow recombination peak in Fig. 5.7(b).

Two additional questions of importance that will be briefly discussed are whether the presence of GBs affects bulk recombination and whether GBs are of equal importance anywhere in the device.

"Does the presence of GBs affect bulk recombination?"

Green [132] discusses this question qualitatively and establishes an upper bound that says

Reproduced with permission of the copyright owner. Further reproduction prohibited without permission.

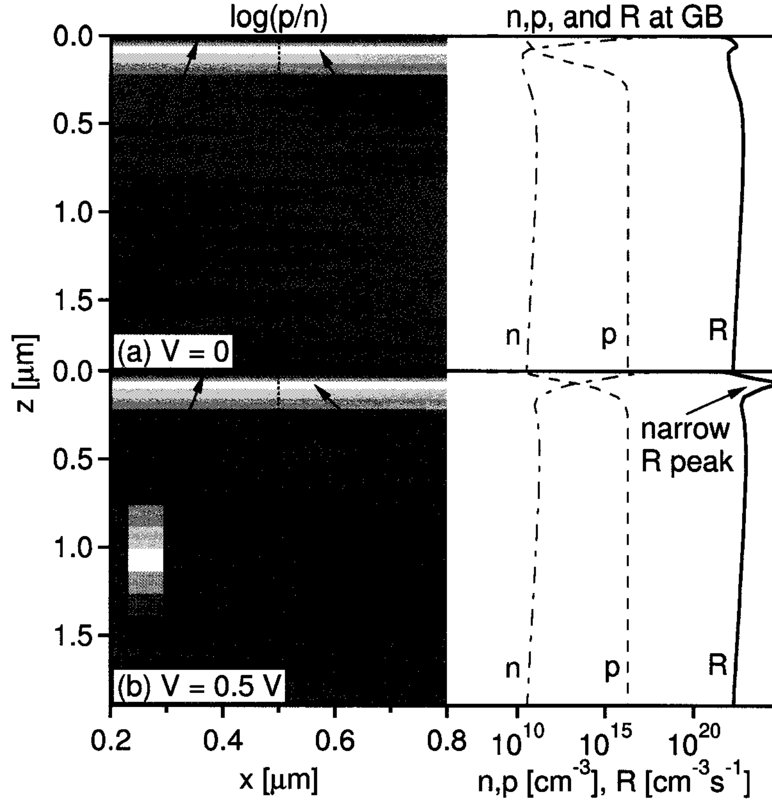

Figure 5.7: Neutral GB recombination, $S_{gb} = 10^5$ cm/s. Relative carrier concentration in the 2D model (left) and n, p, and recombination R along the GB at $x = 0.5$ μm (right) under one sun illumination at (a) $V = 0$ and (b) $V = 0.5$ (slightly below V_{oc}).

that if $R_{bulk}(\vec{x}) = \Delta n/\tau$ is the recombination rate at location $\vec{x}$ in the presence of GBs, then $R_{bulk}(\vec{x}) < R^0_{bulk}(\vec{x})$, where $R^0_{bulk}(\vec{x}) = \Delta n_0/\tau$ and Δn_0 is the excess minority carrier concentration in the absence of GBs. This is a quite general statement based on the observation that any additional recombination introduced by GBs leads to a reduction of the minority carrier density and, hence, also to a reduction of minority recombination. However, the sum of R_{bulk} and R_{gb} will always increase with S_{gb}.

Figure 5.8 shows how the recombination at zero bias is divided between the GBs and the bulk of the material. For zero GB recombination, the current loss is approximately 3 mA/cm^2. This corresponds to the long-wavelength recombination losses discussed in Section 2.2.2. As the GBs become responsible for more recombination, the bulk recombination in fact reduces due to the depletion of minority carriers. Above $S_{gb} > 10^5$ cm/s, the GB recombination losses exceed the bulk losses, although the total current losses have only increased by roughly 30%. For very high values of S_{gb}, recombination occurs predominantly

Reproduced with permission of the copyright owner. Further reproduction prohibited without permission.

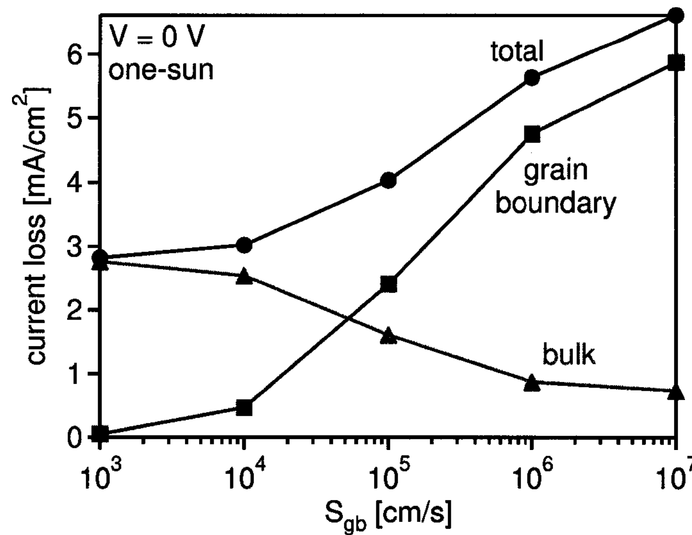

Figure 5.8: GB and bulk recombination with increasing S_{gb}. Higher S_{gb} leads to minority carrier depletion and reduced bulk recombination.

at GBs. It is important to note, that these simulations do not include charged defects which cause electrostatic carrier repulsion or attraction by GBs and strongly influence the results shown in Fig. 5.8. This will be discussed in Sect. 5.4.

"Are GBs of equal importance anywhere in the device?"

Columnar GBs that either start at the CdS/CIGS junction and extend a distance z_{gb} into the film ("expanding," Fig. 5.9[a]), or are of length 50 nm and located at the position z_{gb} ("shifting," Fig. 5.9[b]) are considered. *J*-*V* results corresponding to these two configurations are shown in Fig. 5.10 as a function of GB location z_{gb}.

V_{oc}-losses can be *exclusively* attributed to GBs within the SCR; hence, to achieve high V_{oc}, passivation of GBs in the first few tenths of a micrometer is necessary. Grain boundaries within the quasi-neutral bulk affect the collection efficiency of deeply generated carriers and reduce the long-wavelength quantum efficiency and J_{sc}. The lower V_{oc} also correlates with higher diode quality factors and higher saturation current densities (Fig. 5.6) and this leads to a lowering of the fill factor. The part of columnar grain boundaries that is located deeper than 1 μm from the CdS/CIGS interface is irrelevant for *J*-*V* performance (constant performance for "expanding" GB with $z_{gb} > 1$ μm).

Reproduced with permission of the copyright owner. Further reproduction prohibited without permission.

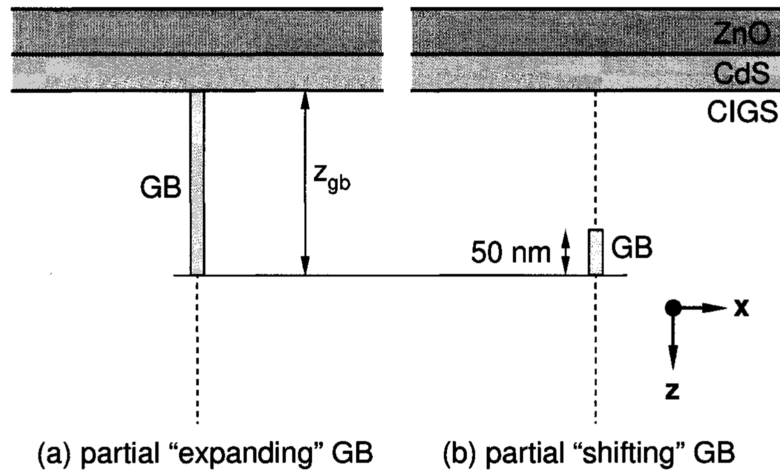

Figure 5.9: Schematic of grain boundaries that either (a) expand or (b) shift through the device along the z-axis. The lateral distance between two grain boundaries is 2 μm.

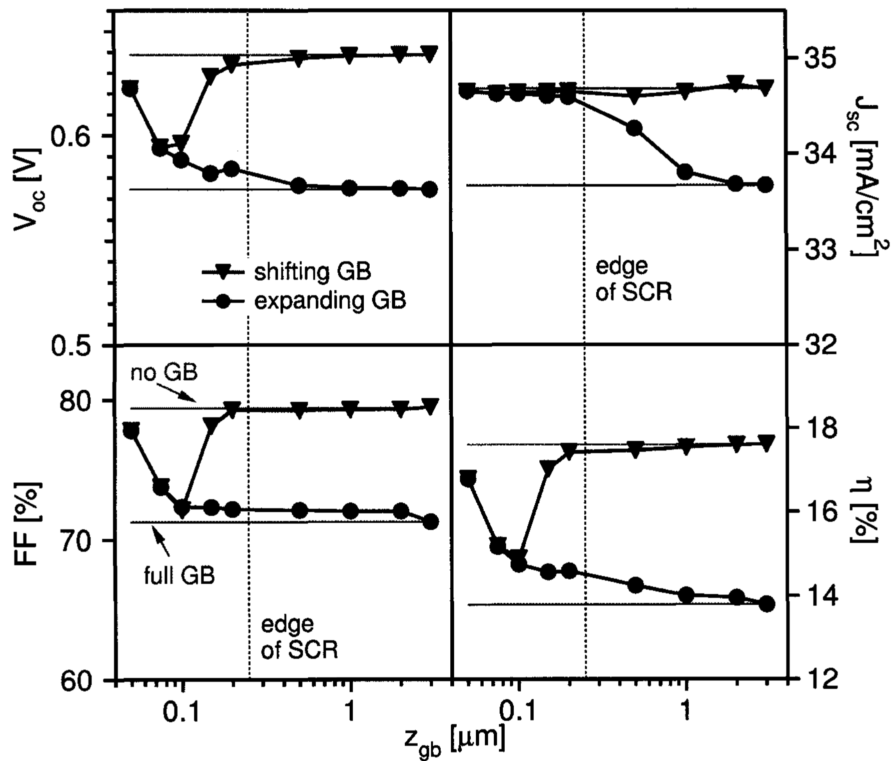

Figure 5.10: J-V results for partial grain boundaries. $S_{gb} = 10^5$ cm/s. For reference, the performance of a GB-free device and a device that contains full columnar GBs at equal S_{gb} are shown.

Reproduced with permission of the copyright owner. Further reproduction prohibited without permission.

5.3.3 Comparison of bulk and grain-boundary recombination

One of the key aspects of this work is to illuminate the effects of grain boundaries on solar-cell performance. A related problem is, *can electrical characterization determine whether GBs limit device efficiency?* Two approaches are taken to investigate this question.

Direct comparision

Direct comparison of bulk and GB recombination for equivalent density of defect states is shown in Fig. 5.11, and the resulting efficiencies for the two cases are tabulated in Table 5.2. There are several important observations to note: (1) there are no qualitative differences in the losses introduced by GBs compared to bulk defects for small to moderate S_{gb} up to 10^5 cm/s, (2) for the same total number of defects and very high S_{gb}, it is favorable to have the defects accumulated within the GB, and (3) there is no difference observable for devices that have modest to high efficiencies (> 12%).

This allows GB recombination to be approximated in one-dimensional models by an increase in bulk defect levels, if the GB effects are weak. An indicator for the latter is a high device performance.

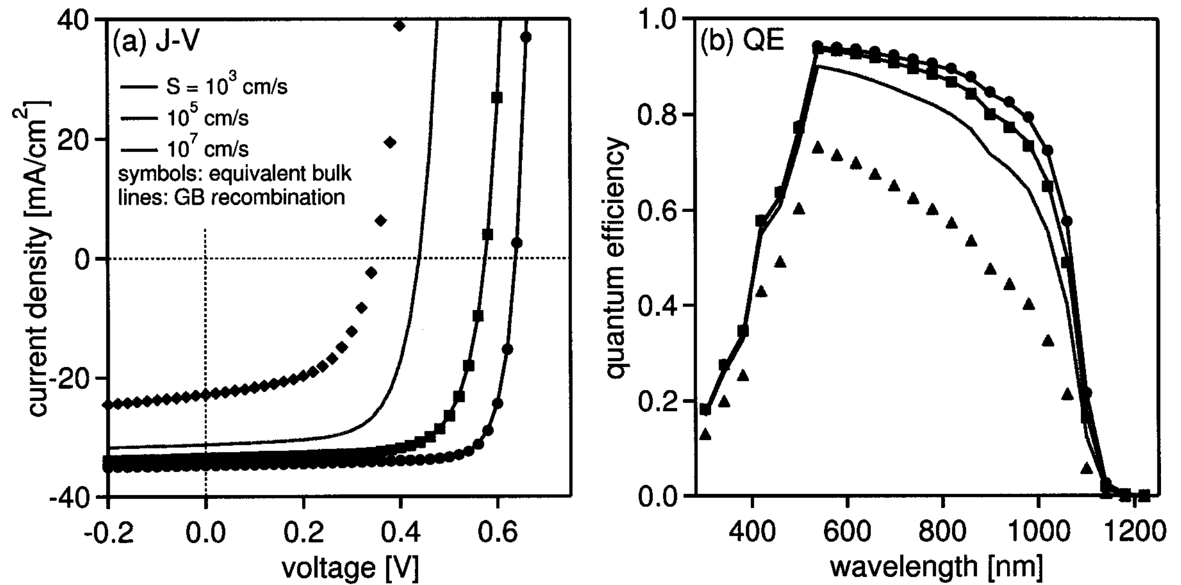

Figure 5.11: Comparison of bulk and grain-boundary recombination. (a) *J-V* and (b) quantum efficiency for selected values of S_{gb}.

Reproduced with permission of the copyright owner. Further reproduction prohibited without permission.

Table 5.2: "Bulk equivalent" and grain boundary models. Parameters further describing the defect levels are used as given in Table 5.1 for both models. All calculations include the defect levels specified for the baseline case listed in Table 3.2. d_g is the distance between two columnar GBs.

	"GB model"	"bulk equivalent"
defect density at GB	10^3–10^8 (cm^{-2})	0
defect density in bulk	0	10^3–$10^8/d_g$ (cm^{-3})
S_{gb} (cm/s)	η (%)	η (%)
10^3	17.5	17.6
10^4	16.7	16.8
10^5	13.8	13.8
10^6	10.5	9.4
10^7	9.1	4.4

On the question of scale

Assuming a constant density of GB states/volume (S_{gb}/d_g = const, in 2D; S_{gb}/d_g^2 = const, in 3D), GB recombination should have an effect very similar to bulk recombination for small grain sizes. In the limit of infinitesimal grain size, $d_g \rightarrow 0$, the results should be identical within the accuracy of the model. On the other hand, in the limit of $d_g \rightarrow \infty$, grain boundaries should become negligible and the performance should recover to that of GB-free device. This is illustrated by the dotted curve in Fig. 5.12. For typical grain sizes of a few micrometers and $S_{gb} = 10^5$ cm/s, GB recombination does indeed appear like bulk recombination and the limit for small d_g is the "bulk equivalent" performance. Grain sizes above 100 μm are necessary to result in a spatial passivation of the GBs. This is far from the experimentally observed grain sizes and, hence, very unlikely to occur.

For comparison, the effects of GB recombination are shown, when it is assumed that S_{gb} is constant as the grain size varies (triangles in Fig. 5.12). In this case, the total number of defects per volume is inversely proportional to d_g in 2D and inversely proportional to the square of d_g in 3D. In 2D, moderate GB quality ($S_{gb} = 10^5$ cm/s) requires grain sizes larger than 10 μm to establish performance above 17%; this is equivalent to the earlier finding that in 1 μm-devices, S_{gb} has to be less than 10^4 cm/s for 17% efficiency. This equivalency, however, breaks down for very large grains, as demonstrated by the black dots in Fig. 5.12, or for very high values of $S_{gb} > 10^5$ cm/s as seen in Table 5.2.

Reproduced with permission of the copyright owner. Further reproduction prohibited without permission.

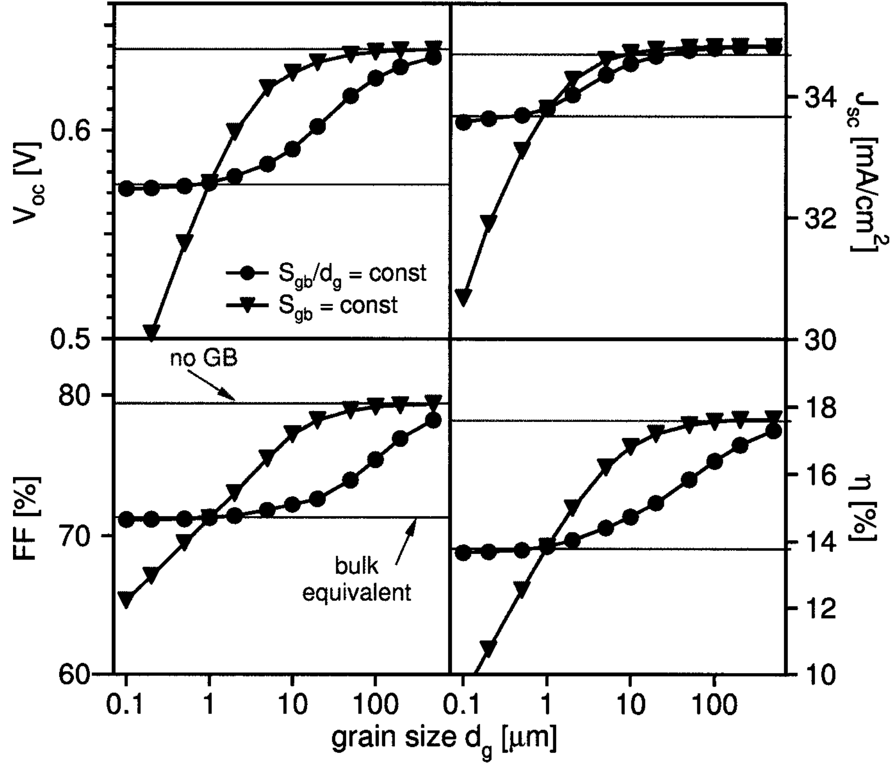

Figure 5.12: *J-V* parameters with varying grain size for columnar GBs.

5.3.4 Analytical model

The *neutral* GB problem can be solved analytically in absence of charge trapping or valence-band offsets. The analytical approach, however, is limited to the calculation of the photoresponse (J_{sc}) as only recombination in the quasi-neutral region (QNR) of the device is considered. GB recombination in the SCR, which is the dominating loss mechanism in forward bias and leads to lowering of V_{oc} and FF (Sect. 5.3.2), is neglected and, therefore, analytical models can not predict these parameters.

Principle of photon accounting

The principle of "photon accounting" [153] is applied to calculate the photocurrent response at zero bias. Three different models determine the collection efficiency from the quasi-neutral bulk region. All of these calculations are based on the same spectral data as the numerical simulations (listed in Appendix A). The calculation of the photocurrent response assumes (1) front reflection $R_F = 5\%$, (2) no collection from ZnO or CdS layer, (3) perfect

Reproduced with permission of the copyright owner. Further reproduction prohibited without permission.

collection in the CIGS space-charge region, (4) collection from the QNR as calculated from the analytical model, and (5) no back reflection. The calculation is performed in four steps:

1. **Reflection and absorption.** The relative absorption, $A = \Phi^{absorbed}/\Phi_0$ (Φ_0 is the incident photon flux), in the CdS layer and the SCR is determined. The photon flux reaching the QNR is reduced by the absorption in these two layers (ZnO absorption is neglected).

$$A_{CdS} = (1 - R_F) \cdot (1 - e^{-\alpha_{CdS} \cdot W_{CdS}}) \tag{5.3}$$

$$A_{SCR} = (1 - R_F - A_{CdS}) \cdot \left(1 - e^{-\alpha_{CIGS} \cdot W_{SCR}}\right) \tag{5.4}$$

2. **Collection probability.** The collection probability in the CdS layer is assumed zero, based on experimental experience. The collection probability in the SCR is assumed 100%, since the strong electric field efficiently separates carriers and reduces recombination. This assumption holds true as long as the transit time through the SCR is much shorter than the recombination lifetime τ:

$$\frac{W_{scr}}{\mu \mathcal{E}} \ll \tau \tag{5.5}$$

($\mathcal{E}$ electric field, μ carrier mobility) In the case of very active GBs, $S_{gb} \geqslant 10^6$ cm/s, this criteria might no longer be fulfilled, and in this case the analytical model overestimates the collection from the SCR.

The collection efficiency for carriers generated in the quasi-neutral region, CE_{QNR}, is determined by the analytical solutions as discussed below. Note that this collection probability includes losses due to deep penetration and, hence, it falls to zero for photons with energies less than the absorber band-gap.

3. **Quantum efficiency.** The quantum efficiency is found by adding the contributions from the SCR and the QNR:

$$QE = A_{SCR} + (1 - R_F - A_{CdS} - A_{SCR}) \cdot CE_{QNR} \tag{5.6}$$

Reproduced with permission of the copyright owner. Further reproduction prohibited without permission.

4. **Photocurrent.** The last step requires the computation of the total light generated current by summation (integration) over all wavelengths:

$$J_{sc} = q \sum_{\lambda} \Phi_{\lambda}^{AM1.5} QE_{\lambda} \tag{5.7}$$

Here, $\Phi_{AM1.5}$ is the discretized incident spectrum in units of [photons/cm^{2}s].

Figure 5.13 illustrates the process by showing (a) relative absorptions, (b) generation in each region considered, (c) collection efficiency calculated with the analytical model, and (d) resulting quantum efficiency of the solar cell. The deep penetration losses are only shown for illustration. The majority of the current ($\sim$ 85%) is collected from the SCR (with unit probability) and, therefore, a lower J_{sc} limit of $\sim$28 mA/cm^2 exists in this simplified analytical approach.

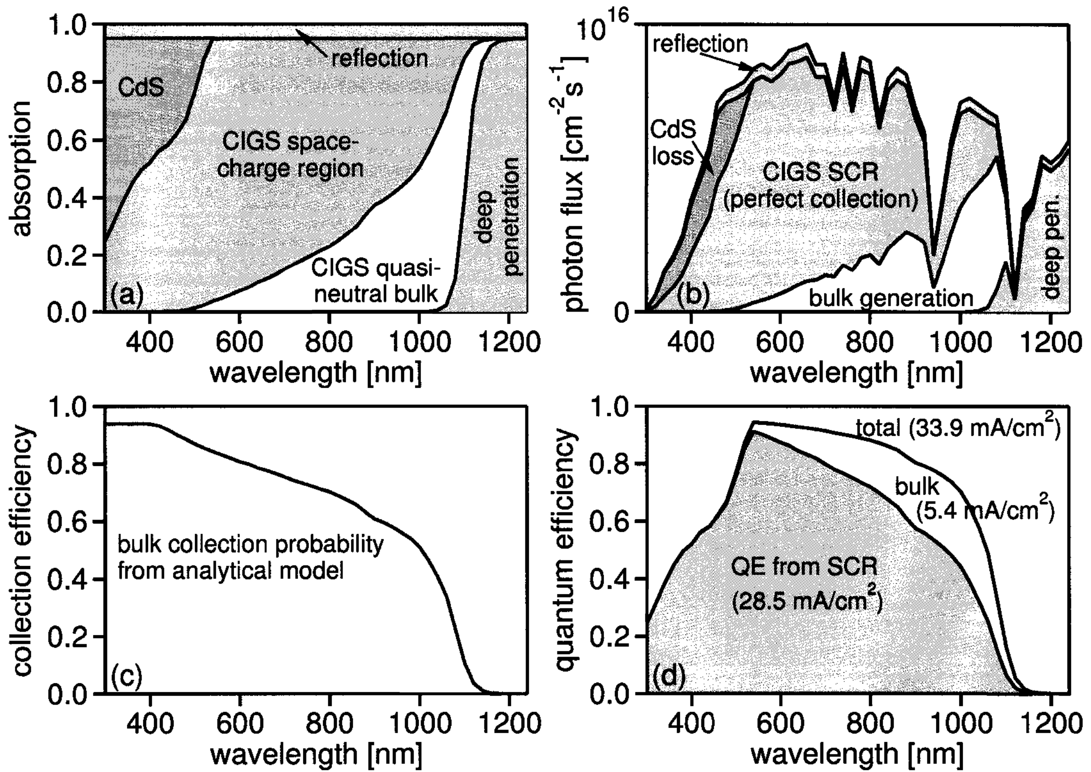

Figure 5.13: (a) stacked plot of relative absorptions and other loss mechanisms involved, (b) same as (a) multiplied by the standard terrestrial spectrum, (c) collection-probability from the QNR, and (d) quantum efficiency.

Reproduced with permission of the copyright owner. Further reproduction prohibited without permission.

Analytical models for the collection in the quasi-neutral region

Applying continuity and current-density equation to a one-sided p-n junction under illumination results in (Φ flux density at $z = 0$ μm, D_n diffusion coefficient) [15, 128]:

$$D_n \left(\frac{\partial^2 \Delta n}{\partial z^2} + \frac{\partial^2 \Delta n}{\partial z^2} + \frac{\partial^2 \Delta n}{\partial z^2} \right) - \frac{\Delta n}{\tau} + \alpha \Phi e^{-\alpha \cdot z} = 0. \tag{5.8}$$

In one dimension, this equation can be solved to determine the excess minority concentration $\Delta n(z)$. Once the carrier distribution is known, all other characteristics are determined as well and the photocurrent can be calculated [15]. This solution only depends on the bulk carrier lifetime τ. Dugas and Oualid [128] solved the problem in three dimensions considering GB recombination and the carrier concentration is then described by an infinite series of the form:

$$\Delta n(x, y, z) = \sum_k \sum_j Z_{kj} cos(c_k x) cos(c_j y). \tag{5.9}$$

The three different models considered for collection from the QNR are:

1. **Effective lifetime.** If GB recombination is weak, GB vs. bulk recombination is indistinguishable. The problem can then be treated in one dimension by the definition of an effective lifetime and a 1D solution to Eq. 5.8 [15]. The effective lifetime is calculated following the approach suggested by others [125, 132], which is equivalent to distributing the GB states throughout the bulk material.

$$\frac{1}{\tau} = \frac{1}{\tau_{bulk}} + \frac{S_{gb}}{d_g} \tag{5.10}$$

2. **Green's upper limit.** Green [132] discussed an upper bound to GB recombination by making the assumption that GB recombination always leads to carrier depletion and, hence, recombination in the presence of GBs is limited $R_{gb} < \Delta n_0 S_{gb}$, where Δn_0 is the minority carrier concentration in the absence of GB recombination. Using the carrier concentration Δn_0 based on the 1D solution that omits GBs [15], the upper

Reproduced with permission of the copyright owner. Further reproduction prohibited without permission.

limit to the GB losses can be calculated by

$$R_{gb} = q \int_{QNR} \Delta n_0(z) S_{gb} dz \tag{5.11}$$

and the photocurrent response is then

$$J_{sc} = J_{sc}(S_{gb} = 0) - R_{gb}/d_g. \tag{5.12}$$

3. **Three-dimensional model.** The series solution (Eq. 5.9) [128] is evaluated for a range of S_{gb}. The grain sizes are chosen as 1×1 μm^2 for the 3D calculation or as 1×10^4 μm^2 to establish a quasi-2D solution; the latter allows direct comparison to the numerical model results.

Analytical results for neutral GB recombination

The photocurrent response at zero bias (J_{sc}) based on all three analytical models is shown in Fig. 5.14(a). Green's upper limit strongly overestimates recombination at GBs for modest to large values of $S_{gb} > 10^4$ cm/s. In this situation, GB recombination is comparable to or dominates over bulk recombination, $S_{gb}/d_g < \tau_{bulk}$. The minority carrier density is assumed to be equal to the GB-free concentration (it does not reduce in the presence of additional recombination) and, hence, an unphysical situation is implied in which the same electron can recombine multiple times. It is concluded that this approach, although it does establish a valid upper bound on GB recombination, delivers poor quantification, if the disturbance caused by GB recombination is comparable to or stronger than bulk recombination, $S_{gb}/d_g \sim \tau_{bulk}$.

The effective lifetime model in Fig. 5.14(a) follows the 2D solution up to values in the mid-10^5 cm/s range. For lower values of S_{gb}, the agreement is excellent (this equivalency is very similar to the one shown in Table 5.2) and, therefore, for cases where GBs are a minor disturbance, an effective lifetime approach is appropriate. For larger values of S_{gb}, a local depletion of electrons occurs at the GB (in the 2D solution) that is ignored in the effective lifetime picture. The recombination at GBs, $R_{gb} = \Delta n S_{gb}$, becomes self-limiting

Reproduced with permission of the copyright owner. Further reproduction prohibited without permission.

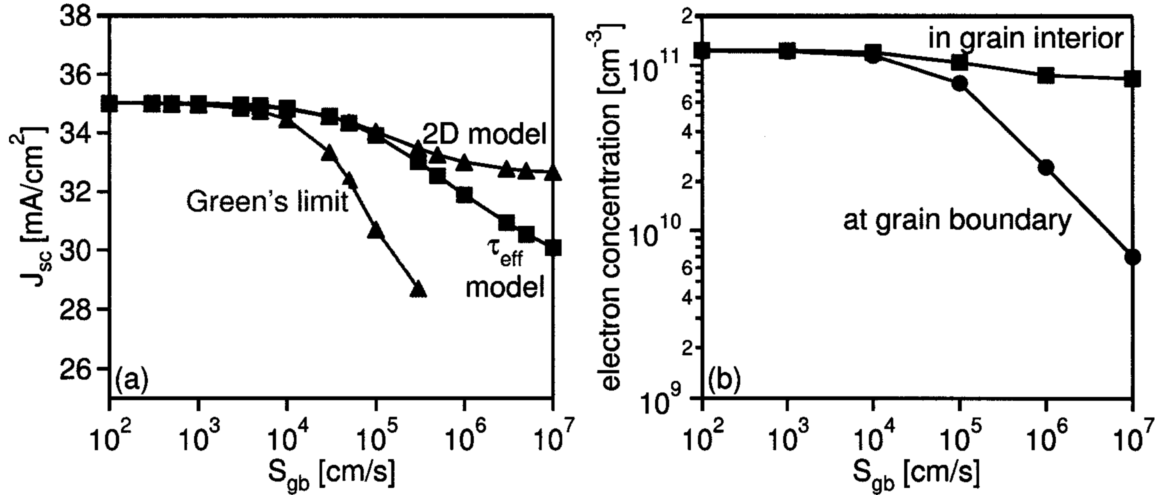

Figure 5.14: (a) Short-circuit current density for Green's limit, effective lifetime, and 2D models. (b) Carrier depletion at the GB from the 2D model, this effect is ignored in 1D approaches.

once large values of R_{gb} lead to a reduction of Δn. The depletion of carriers at the GB is shown in Fig. 5.14(b), which compares the carrier concentrations in the grain interior and at the grain boundary. For large values of S_{gb}, Δn at the GB, and with that the effective GB recombination, reduces by one order of magnitude.

The three-dimensional model following Ref. [128] allows a comparison of two- and three-dimensional models (Fig. 5.15[a]). The error introduced by using a 2D instead of 3D model is small. The difference is roughly a factor of 2 in S_{gb}, based on having twice as many GB states/volume in 3D compared to 2D. The results however, are similar enough across the full range of S_{gb} to justify the use of the 2D numerical model. Figure 5.15(b) shows the comparison between the two-dimensional numerical and analytical solutions. The J_{sc} values found from both models agree well, but a small discrepancy occurs for large S_{gb}. As discussed earlier, for very large values of S_{gb} the collection from the SCR is no longer ideal and the analytical model overestimates J_{sc}. Although, two or three-dimensional analytical models can give fairly good estimates on J_{sc}, the fact that they are limited to the quasi-neutral region limits their accuracy if S_{gb} is large.

Reproduced with permission of the copyright owner. Further reproduction prohibited without permission.

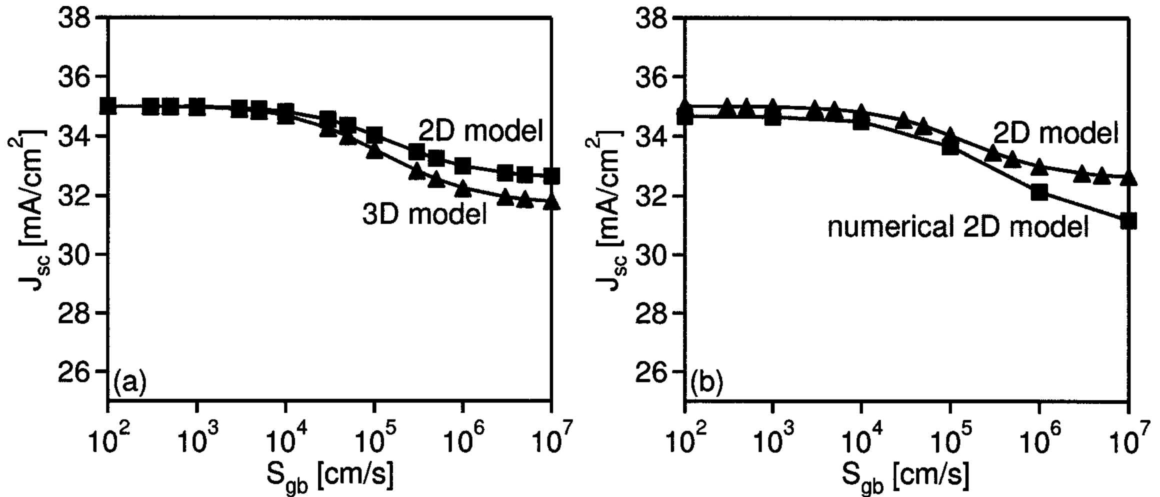

Figure 5.15: (a) J_{sc} calculated from 2D and 3D models. A small difference exists for large values of S_{gb}. (b) Comparison of numerical and analytical model, both 2D.

5.3.5 Summary

In this section, the effects of neutral grain boundaries on solar-cell performance has been investigated. The effects of horizontal and columnar GBs were quantified, and the stage is now set for the discussion of modified GBs in the Sects. 5.4 and 5.5. Horizontal GBs have the potential to be very detrimental and, hence, should remain under consideration in the studies of local non-uniformities. Columnar GBs, which are the typical CIGS thin films, can limit device performance, if the GB recombination exceeds 10^4 cm/s.

Detailed analysis showed that V_{oc} is only affected by GBs within the space-charge region, or conversely, a GB passivation mechanism needs to be only active within the SCR to achieve high V_{oc}. The short-circuit current density is affected by GBs within the quasi-neutral region, but GBs more than 1 μm from the junction are not important. Comparative simulations with bulk-distributed defects showed that solar-cell performance is indistinguishable between GB and bulk recombination. For a typical grain size of 1 μm, the GB recombination can be misinterpreted as an increased density of bulk recombination centers.

Several analytical models were used to calculate the photocurrent response at zero bias. One-dimensional solutions severely overestimate the impact of grain boundaries, because the carrier depletion is neglected. Two- or three-dimensional solutions are still limited in their accuracy, because the non-ideal collection efficiency from the SCR is ignored. Similar

Reproduced with permission of the copyright owner. Further reproduction prohibited without permission.

results are found with 2D and 3D solutions and, hence, the use of 2D numerical models becomes justified.

5.4 Charged grain boundaries

Any defect level in a semiconductor can cause both recombination and supply charge to the overall charge-distribution. In this section, charge carrying defects are introduced at GBs in sufficiently high densities to cause significant distortions to the conduction and valence bands. Such distortions, often labeled "grain-boundary potentials" or "band-bending," have been determined by surface-sensitive techniques and were reviewed in Sect. 5.1.2. It is unclear to date, whether such potentials exist in the grain interior.

Figure 5.16 shows the effects of charged donor levels (positive sheet charge) at a GB in a p-type semiconductor. In general, it is much more likely that GBs lead to a majority carrier "depletion" (as shown) instead of "accumulation," e.g., in the case of p-type material, the Fermi-level is close to the valence band and deep states are most likely positively charged

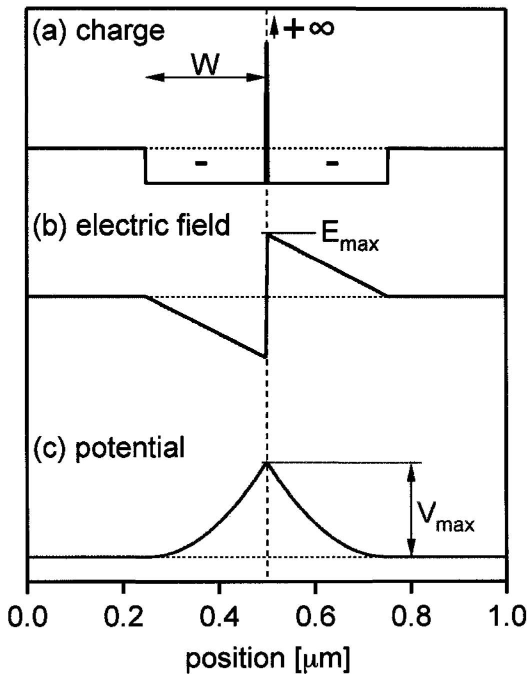

Figure 5.16: (a) Charge distribution in the presence of a positively charged GB. (b) Electric field is determined by integration of the Poisson equation. The maximum electric field is $\mathcal{E} = qN_{gb}/2\epsilon$. (c) Electrostatic potential $V(x)$.

Reproduced with permission of the copyright owner. Further reproduction prohibited without permission.

or neutral. The reverse would be true for n-type material. This situation is also supported by the majority of experimental results [141, 143–145]. A depletion region of width W is established on both sides of the GB. Charge neutrality demands

$$\begin{aligned} Q^- &= Q^+ \\ 2qN_AW &= qN_{gb}^+ \end{aligned} \tag{5.13}$$

where N_A is the bulk doping in (cm^{-3}) and N_{gb}^+ the density of charged GB states in (cm^{-2}). Integration of the Poisson equation gives the electric field (Fig. 5.16[b]) and a second integration step the electrostatic potential (Fig. 5.16[c]). Positive charges (hole carriers) are repelled from the negatively charged GB. The maximum potential difference is found at the location of the GB:

$$V_{max} = \frac{q}{8\epsilon}\frac{N_{gb}^{+2}}{N_A}. \tag{5.14}$$

For practical purposes, the remainder of this work will not use the potential difference, but the energy difference, ϕ_{gb}, as parameter. By convention, this parameter will be labeled positive if the potential is hole repulsive.

$$\phi_{gb} = |qV_{max}| = \frac{q^2}{8\epsilon}\frac{N_{gb}^{+2}}{N_A}. \tag{5.15}$$

Electron-repulsive potentials in p-type semiconductor ("accumulation of free holes") will be considered as well. In this case, the potential is established by free carriers and cannot be readily solved by integration; a detailed discussion is given by Mönch [154]. In the accumulated case, the barriers are described by the parameter $\phi_{gb} < 0$.

Input parameters for the simulation are the density of GB states and the energetic defect distributions (Table 5.1). The fully consistent solution determines whether these states are ionized under the considered light and voltage bias. The schematic for the charged GB model is given in Fig. 5.17(a) and an example for a resulting two-dimensional conduction band diagram is shown in Fig. 5.17(b). The band diagram represents the energy differences in terms of electron carries. A down-bending of the conduction band as shown in Fig. 5.17(b) is equivalent to an up-bending of the potential as shown in Fig. 5.16(c).

Reproduced with permission of the copyright owner. Further reproduction prohibited without permission.

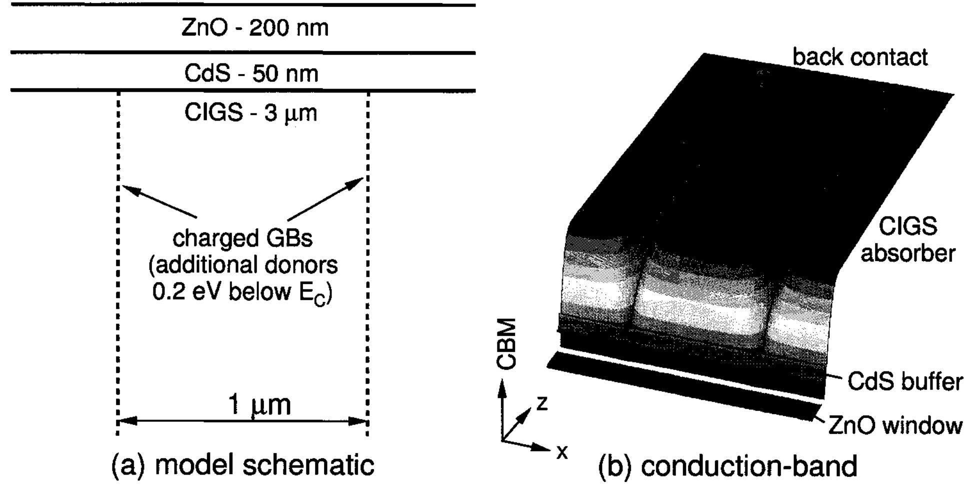

Figure 5.17: Two-dimensional model of charged grain boundaries: (a) schematic of the model and (b) resulting plot of the conduction-band minimum (CBM).

Case studies of ϕ_{gb} = -0.05 eV, +0.2 eV and +0.6 eV

The influence of GB potentials is investigated in two approaches:

1. GB potential is fixed, ϕ_{gb} = -0.05 eV, +0.2 eV, and +0.6 eV and S_{gb} is varied.

2. GB recombination velocity is fixed at $S_{gb} = 10^4$ cm/s and $S_{gb} = 10^5$ cm/s and ϕ_{gb} is varied.

The input parameters (type of defect, defect density) and output parameter (ϕ_{gb}, η) for these cases are listed in Table 5.3. Although ϕ_{gb} is a result of the simulation, this parameter is used for convenience to classify the models. There is an infinite combination of defect distributions and densities that can establish a particular value of ϕ_{gb}, but the *J-V* results are strongly dependent on the value of ϕ_{gb} and relatively insensitive to how it

Table 5.3: Input parameters and device efficiencies with $S_{gb} = 10^5$ cm/s for the three cases of band-bending that will be studied in detail, ϕ_{gb} = -0.05 eV, +0.2 eV and +0.6 eV. Case (a) has no charged defect levels and is only shown for reference.

Fig. 5.18	defect	N_{gb} (cm^{-2})	ϕ_{gb} (eV)	η at S$_{gb}$ = 10^5 cm/s (%)
(a)	-	-	0	13.8
(b)	donor	4.5×10^{11}	0.2	11.3
(c)	donor	9×10^{11}	0.6	14.3
(d)	acceptor	5×10^{11}	-0.05	15.4

Reproduced with permission of the copyright owner. Further reproduction prohibited without permission.

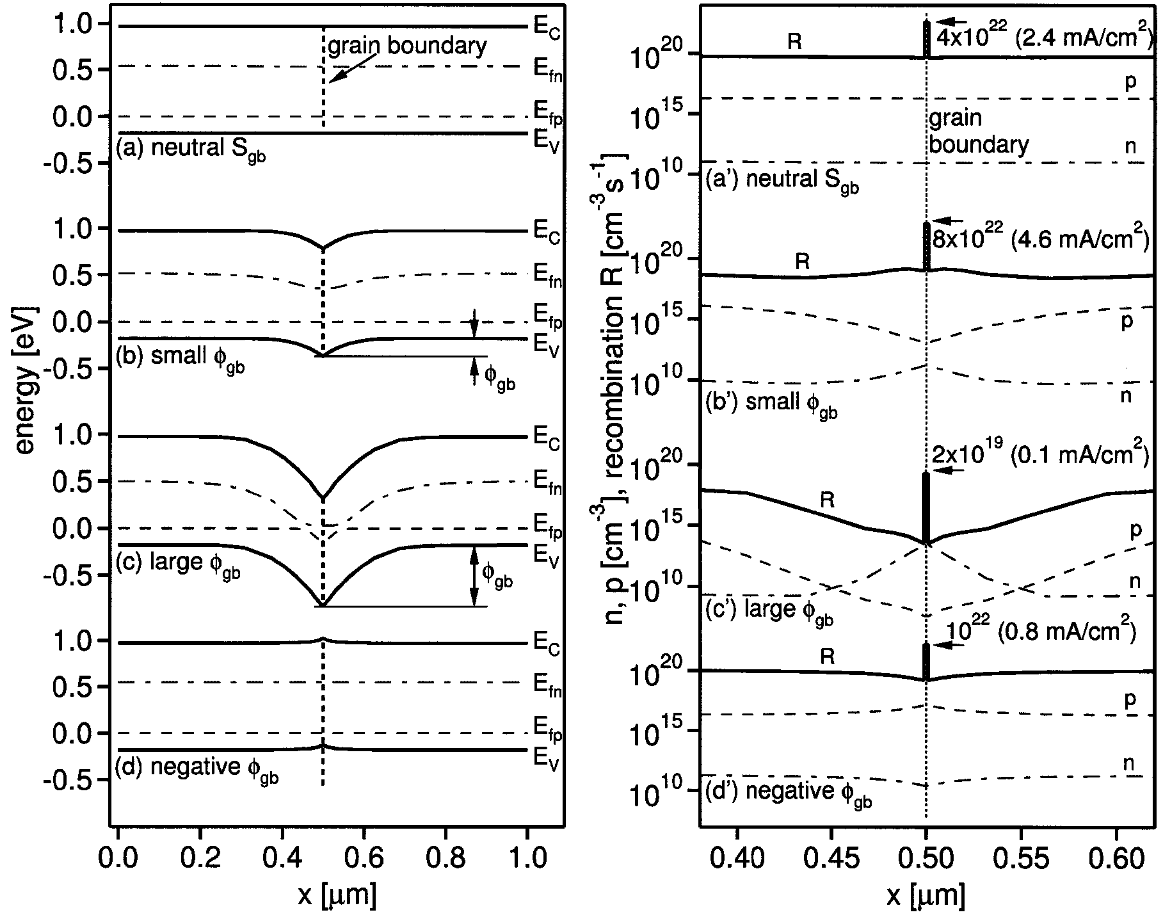

Figure 5.18: Band structure parallel to the main junction at $z = 1\mu$m. All cases for columnar GBs at zero external bias under 1 sun illumination: (a) no band-bending, (b) small positive, (c) large positive, and (d) small negative ϕ_{gb}. Figures (a')–(d') show the corresponding carrier concentrations and recombination rates (Note the expanded horizontal scale). The sheet density of recombination ($\text{cm}^{-2}\text{s}^{-1}$) is found by multiplying R at the GB by the GB width (2 nm). Corresponding integrated current losses are shown in parentheses.

was established. Additional discussion of this topic is given in Sect. 5.6.

Starting from a CIGS model with columnar GBs (schematic in Fig. 5.17[a]), and the flat band structure shown in Fig. 5.18(a), the following cases are discussed:

Electrostatic majority-hole repulsion by donor-like defects at GBs. These levels introduce a down-bending of both bands toward the GB by $\phi_{gb} = E_C^{bulk} - E_C^{GB}$; the resulting band structures for two values of ϕ_{gb} are shown in Fig. 5.18(b) and (c). There is no speculation on the nature of these donor defects and they are assumed to be located ~0.2 eV below the conduction-band edge with appropriate density to establish a band-bending of

Reproduced with permission of the copyright owner. Further reproduction prohibited without permission.

$\phi_{gb} > 0$.

Electrostatic minority-electron repulsion by an increased shallow acceptor density at the GB. These additional acceptor levels are placed 0.1 eV above the valence-band maximum. Conduction and valence band shift upward at the GB and this is described by the parameter $\phi_{gb} < 0$.

Figure 5.18(a')–(d') show the carrier concentration and recombination profile for the cases described in Fig. 5.18(a)–(d). The plots are 'cross-sections' to the 2D model parallel to and a distance of 1 μm from the main junction, outside of the SCR. Figure 5.18(a') shows the flat carrier densities n and p and enhanced recombination rate R at the GB corresponding to Fig. 5.18(a). Positive band-bending (Fig. 5.18[b']) repels holes, increases the density of electrons at the GB, and results in still higher GB recombination. Large positive band-bending (Fig. 5.18[c']) leads to a type inversion at the boundary, minority-electrons become majority carriers, and recombination decreases. The current densities in parentheses are the recombination losses integrated over the z direction (perpendicular to the graph). These losses are related, but not equal, to the losses in J_{sc}; the difference arises from changes in bulk recombination due to the presence of charged and uncharged grain boundaries similar to the effects discussed Sect. 5.3.2.

5.4.1 Results

The electrostatic potential difference, ϕ_{gb}, is defined at zero bias as indicated in Fig. 5.18(b) and only weakly affected by illumination. Solar-cell performance parameters calculated for S_{gb} up to 10^7 cm/s and the three values of ϕ_{gb} under study are shown in Fig. 5.19. Small negative band-bending leads to improvements in all parameters. Small or large positive ϕ_{gb} substantially lowers V_{oc}. J_{sc} is lower with $\phi_{gb} = 0.2$ eV, but high for $\phi_{gb} = 0.6$ eV. With the exception of very high values for S_{gb} and ϕ_{gb}, hole-repulsion at GBs leads to an additional reduction of device efficiency.

Performance parameters for $S_{gb} = 10^5$ cm/s in dependence of ϕ_{gb} are shown in Fig. 5.20. Negative ϕ_{gb} (acceptors) can help passivate the GB, current as well as voltage recovers. However, a very high density of GB states needs to be assumed (density/grain width $\gg$ bulk doping) to establish performance similar to that of GB-free devices. This possibility

Reproduced with permission of the copyright owner. Further reproduction prohibited without permission.

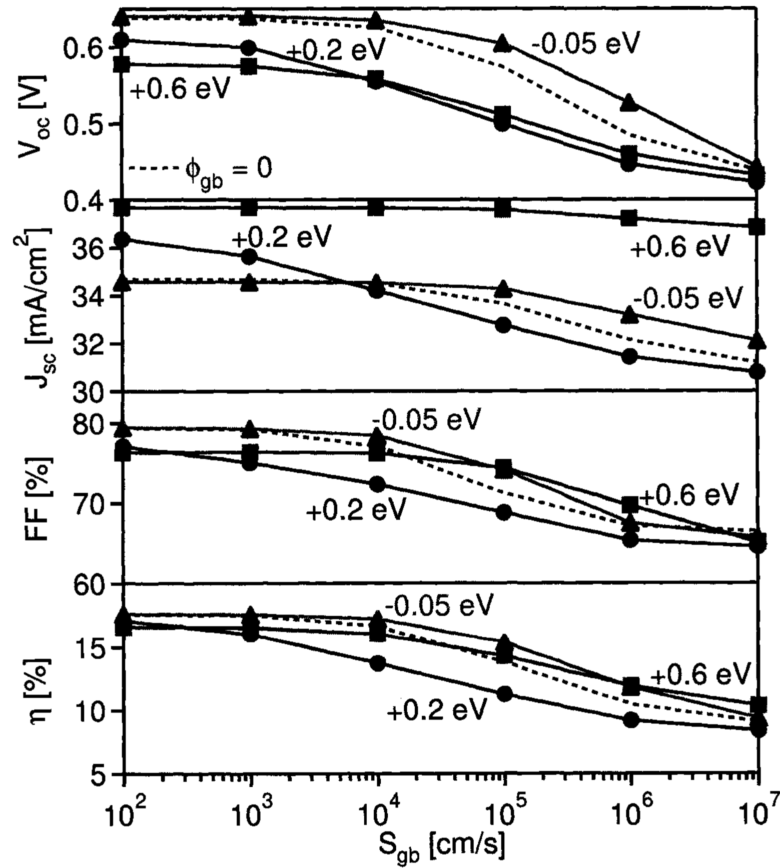

Figure 5.19: *J-V* parameters V_{oc}, J_{sc}, FF, and η for ϕ_{gb} = -0.05 eV (electron repulsion), 0.2 eV (weak hole repulsion), and 0.6 eV (strong hole repulsion). All band-bending is defined under one sun illumination at zero bias and at a distance $z = 1$ μm from the junction.

Reproduced with permission of the copyright owner. Further reproduction prohibited without permission.

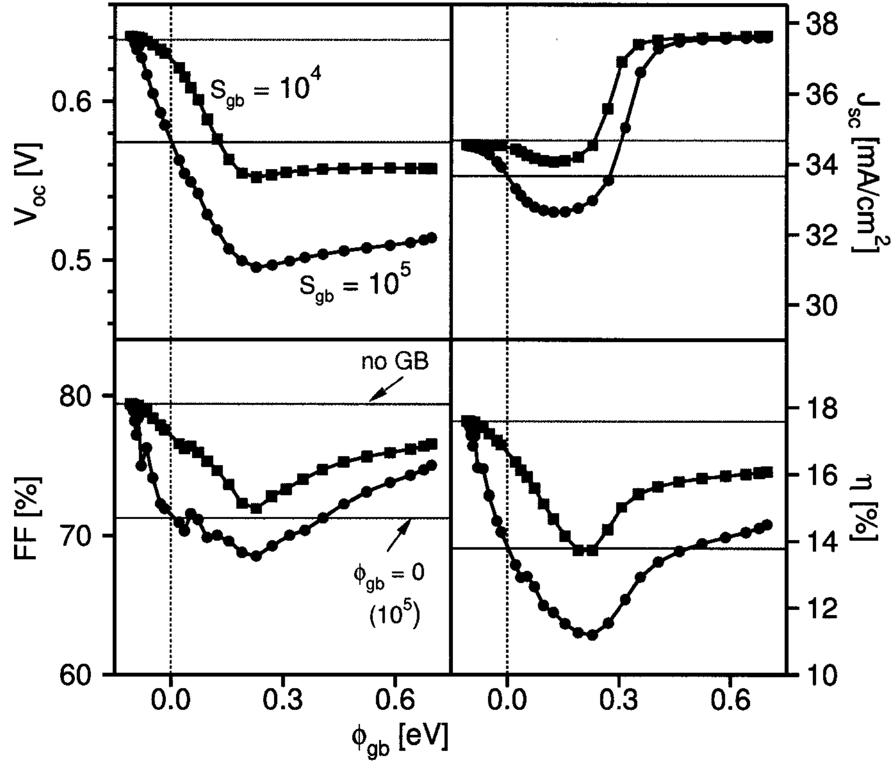

Figure 5.20: *J*-*V* parameters with positive and negative electrostatic potential ϕ_{gb}.

has to be considered as unrealistic because in this situation, defect characterization, e.g., by capacitance methods, should give evidence of such high defect densities. Positive ϕ_{gb} (donors) is detrimental to V_{oc}. For positive ϕ_{gb}, J_{sc} decreases, has a minimum near $\phi_{gb} \sim$ 0.15 eV, and increases up to 10% for higher values. For $\phi_{gb} > 0.4$ eV, practically all electron-hole pairs generated in the bulk are collected and the internal quantum efficiency is very near unity for all photons with energy $E_g^{CIGS} < E_{photon} < E_g^{CdS}$. The net effect on η is at best a compensation for the lower V_{oc}. Even for smaller values of $S_{gb} = 10^4$ cm/s, $\phi_{gb} > 0$ appears detrimental to device performance, and η is significanly below that of GB-free devices.

5.4.2 Discussion of hole-repulsive band-bending

Grain-boundary recombination is calculated by the expression (Sect. 3.1.3) [48]:

$$R_{gb} = \frac{np - n_i^2}{(n + n_1)/S_p + (p + p_1)/S_n}. \tag{5.16}$$

Reproduced with permission of the copyright owner. Further reproduction prohibited without permission.

The recombination centers are assumed mid-gap and, therefore, $n_1 \simeq p_1 \simeq 10^9$ cm^{-3}; for standard AM1.5 illumination the generated steady state concentration $n \sim 10^{11}$ cm^{-3}. Hence, for the situation depicted in Fig. 5.18(a) and (b): n_i, $p_i \ll n \ll p$, and Eq. 5.16 simplifies to

$$R_{gb} \simeq \Delta n S_{gb}. \tag{5.17}$$

The carrier distribution throughout the 2D model as well as the carrier densities and recombination distribution at the GB for $\phi_{gb} = 0.2$ eV is shown in Fig. 5.21. The positively charged GB attracts electrons and repels holes; the bulk part of the GB ($z > 0.5\mu$m) is shifted toward the $n \sim p$ condition. This increases recombination at zero bias as it has to be expected from Eq. 5.17. The junction width at the GB increases and in forward bias the recombination peak significantly broadens (compare Fig. 5.21[b] to Fig. 5.7[b] on p. 86).

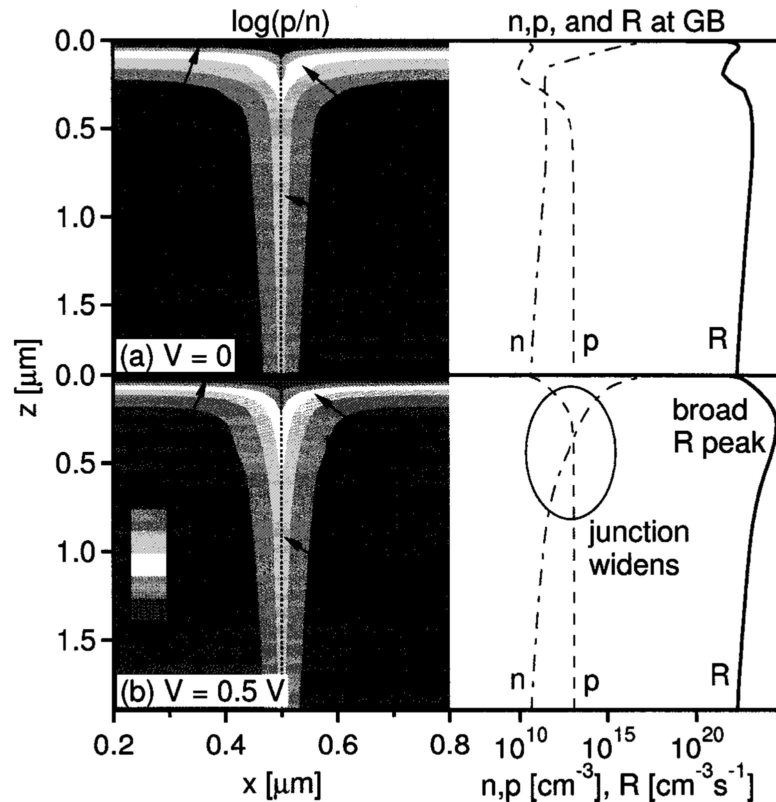

Figure 5.21: Small hole repulsive band-bending, $S_{gb} = 10^5$ cm/s. Relative carrier concentration in the 2D model (left) and n, p, and recombination R at the GB (right) under one sun illumination at (a) $V = 0$ and (b) $V = 0.5$ V (slightly below V_{oc}). At zero bias, recombination in the GB increases, and under forward bias the recombination peak significantly broadens.

Reproduced with permission of the copyright owner. Further reproduction prohibited without permission.

The area under the R-curve is proportional to the GB forward-current contribution and, hence, in the presence of small ϕ_{gb}, V_{oc} is substantially lowered.

For higher $\phi_{gb} = 0.6$ eV, the GB inverts, $n > p$ (Fig. 5.22[a]), and the p-n junction extends from the CdS/CIGS interface along the grain surface deep into the absorber layer. Recombination at the GB is strongly reduced due to a lack of holes. However, in forward bias (Fig. 5.22[b]), the band-bending reduces and recombination increases; the GB is shifted toward the condition $n \sim p$ again and the entire GB becomes a high recombination region. High forward currents flow and V_{oc} is reduced.

The reduction of the band-bending is caused by the discharging (re-population) of the assumed donor levels. This occurs once the electron quasi-Fermi level approaches the defect level (the material enriches in electrons by injection). Based on this consideration, an

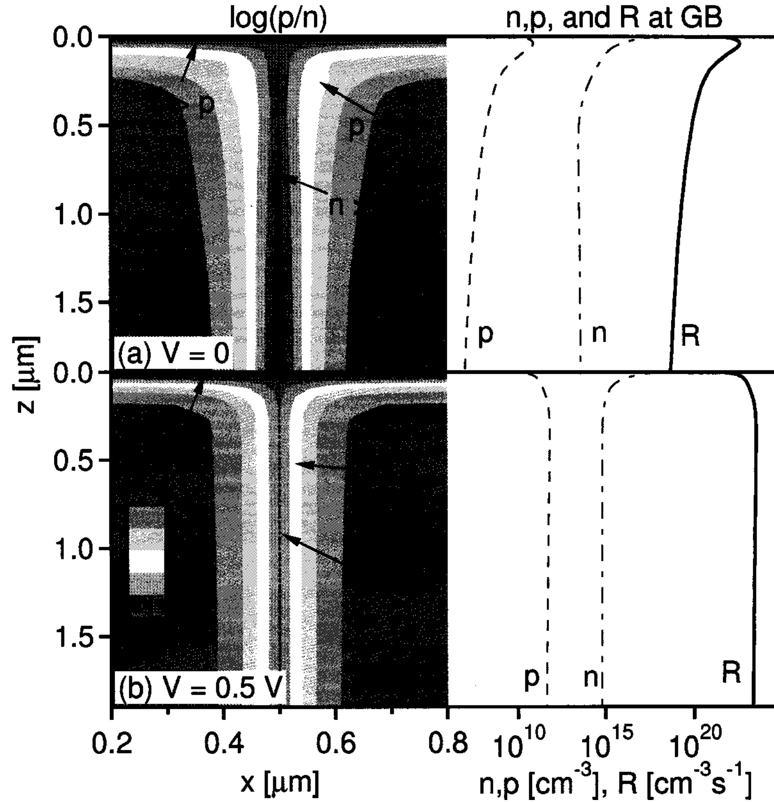

Figure 5.22: Large hole repulsive band-bending, $S_{gb} = 10^5$ cm/s. Relative carrier concentration in the 2D model (left) and n, p, and recombination R at the GB (right) under one sun illumination at (a) $V = 0$ and (b) $V = 0.5$ V (slightly below V_{oc}). The GB is inverted, however, under forward bias some of the inversion is recovered. Recombination is high in the entire GB.

Reproduced with permission of the copyright owner. Further reproduction prohibited without permission.

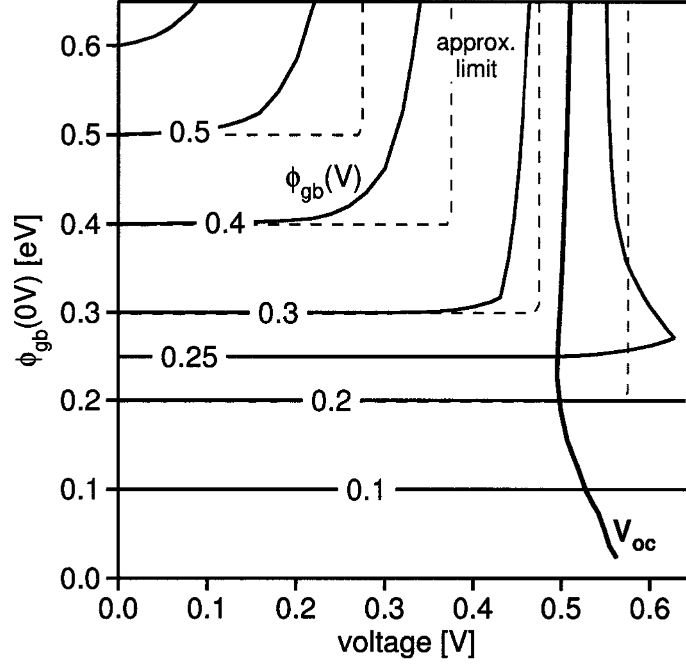

Figure 5.23: Band-bending in the absorber at $z = 1\ \mu$m under forward bias. The discharge of GB states reduces larger values of ϕ_{gb} under forward bias. The V_{oc} line is shown for reference.

estimate can be given when this change occurs and the band-bending is roughly limited to values less than

$$E_g - \phi_{fp} - 0.2\ eV - qV. \tag{5.18}$$

ϕ_{fp} is the distance of the hole quasi-Fermi level from the valence-band maximum ($E_{fp} - E_V \sim 0.18$ eV) and V the applied voltage. The value of 0.2 eV is the location of the donor level with respect to the conduction-band maximum. The actual band-bending as a function of voltage (result of the simulation) as well as the approximation expressed in Eq. 5.18 is shown in Fig. 5.23. The agreement is quite good and, therefore, Eq. 5.18 also predicts that deeper donor levels allow for less GB potential under otherwise similar conditions. Furthermore, the zero bias GB potential is limited to values of $E_g - \phi_{fp} - (E_C - E_T) = E_T - E_{fp}$, the distance between the donor level and the hole quasi-Fermi level.

5.4.3 Discussion of electron-repulsive band-bending

Since recombination in the quasi-neutral region depends only on the minority carrier concentration, $R = \Delta n S_{gb}$, repulsion of electrons reduces recombination. The additional negative

Reproduced with permission of the copyright owner. Further reproduction prohibited without permission.

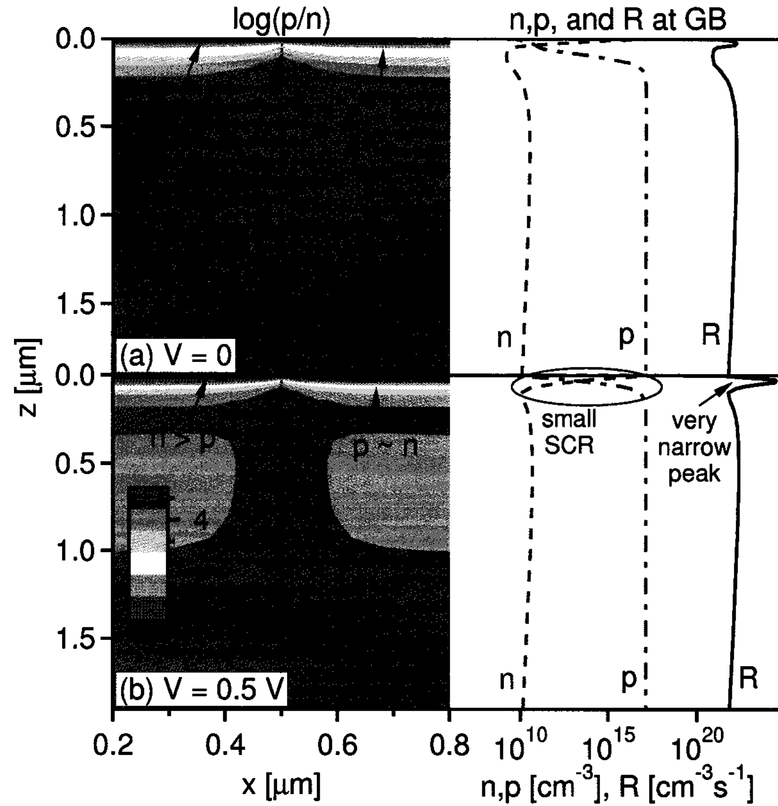

Figure 5.24: Small electron repulsive band bending, $S_{gb} = 10^5$ cm/s. Relative carrier concentration in the 2D model (left) and n, p, and recombination R at the GB (right) under one sun illumination at (a) $V = 0$ and (b) $V = 0.5$ V (slightly below V_{oc}). The depletion width is narrowed as is the high-recombination peak at the GB.

charge at grain boundaries reduces the *p-n* junction width at the GB and leads to reduced SCR recombination, which is apparent from the narrower recombination peak under forward bias (Fig. 5.24[b]).

5.4.4 Analytical model

The analytical solutions described in Sect. 5.3.2 allowed to predict GB recombination in the quasi-neutral region (and J_{sc}), but did not incorporate GB potentials. GB recombination in the presence of ϕ_{gb} and S_{gb} can be considered, if an approximate expression for the effective recombination velocity, $S(\phi)$, is determined.

Assuming constant quasi-Fermi levels across the GB, the carrier concentrations at the boundary can be estimated as $p(\phi) \simeq p^0 e^{-\phi_{gb}/kT}$ and $n(\phi) \simeq n^0 e^{+\phi_{gb}/kT}$. With this, Eq. 5.16 can be rewritten and the effective surface recombination velocity $S(\phi)$ defined (shown in

Reproduced with permission of the copyright owner. Further reproduction prohibited without permission.

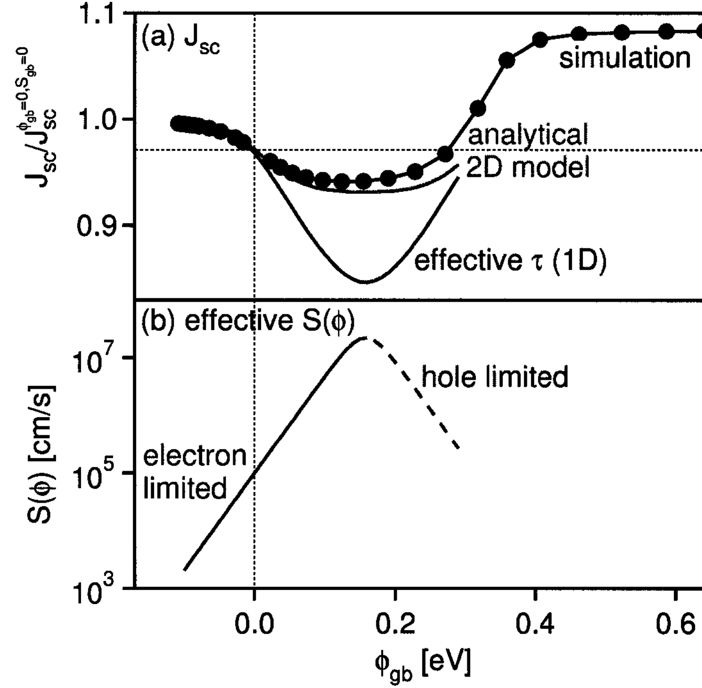

Figure 5.25: Effect of charge-induced band-bending on current. (a) Short-circuit current density (normalized to the GB-free case) at zero bias. (b) Effective GB recombination velocity S_{eff}. For $\phi_{gb} > 0.2$ eV the recombination is limited by the suppressed hole concentration.

Fig. 5.25[b]):

$$R_{gb}(\phi) = \frac{\Delta n^0 S_n^0}{\left(n^0 S_n^0 / p^0 S_p^0\right) e^{\phi_{gb}/kT} + e^{-\phi_{gb}/kT}} = \Delta n^0 S(\phi) \tag{5.19}$$

Moderate GB recombination velocity, S_{gb} ($= 10^5$ cm/s), in combination with small ϕ_{gb} results in an *effective* GB recombination the order of 10^7 cm/s. For small ϕ_{gb}, the effective $S(\phi)$ follows the enhancement factor $e^{q|\phi_{gb}|/kT}$ discussed by Green [132]. Combining $S(\phi)$ with the two-dimensional analytical solution (2D model described in Sect. 5.3.4) results in a reasonable fit to the numerical result in the range of -0.1 to 0.3 eV shown in Fig. 5.25(a). The same approach with the "effective lifetime" model (also presented in Sect. 5.3.4) strongly overestimates the recombination due to the neglected carrier depletion effects that have been discussed earlier. The recombination maximizes when the quasi-Fermi levels are approximately equal distances from the band edges, or more accurately when $n \sim p$, and this criteria is fulfilled significantly before the majority quasi-Fermi level is located at the middle of the gap.

Reproduced with permission of the copyright owner. Further reproduction prohibited without permission.

For larger band-bending, the strong electric field attracts practically all electrons to the GB, but at zero bias, the GB is strongly inverted and no recombination occurs due to the lack of holes. Under these conditions, the collection efficiency (J_{sc}) improves beyond that of GB-free devices. This is further illustrated in Fig. 5.26. Practically all electrons generated outside the main-junction SCR are flowing toward the GB. There, electrons are channeled and conducted to the main junction. Holes are repelled from the GB and hole conduction occurs in the neutral region between GBs. Most of the generation occurs in the SCR and the enhancement by GB collection is therefore limited to roughly 15% (Fig. 5.25); even very deep in the device, $z > 1$ μm, the GB collection still occurs, however, the additional current contribution is insignificant for device performance.

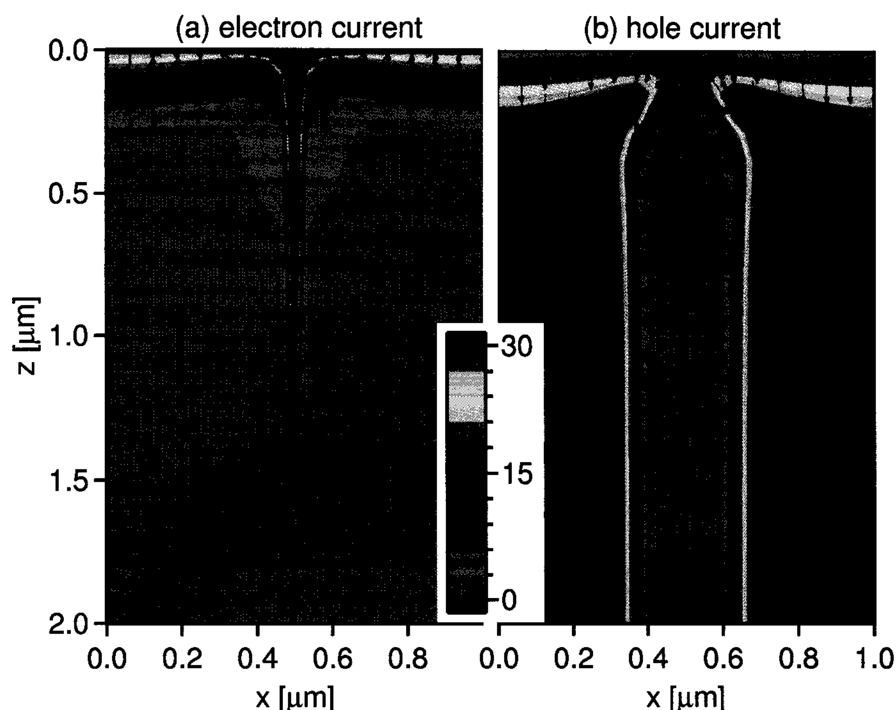

Figure 5.26: Electron and hole current flows with $\phi_{gb} = 0.4$ eV. Similar for higher values of ϕ_{gb}. Contour plot shows (a) electron and (b) hole current density in (mA/cm^2); arrows indicate carrier transport direction (unit vectors of carrier velocity). Short-circuit conditions of one-sun illumination and zero voltage bias.

Reproduced with permission of the copyright owner. Further reproduction prohibited without permission.

5.4.5 Summary

Several surface sensitive experiments have determined band-bending at GBs and this section has discussed the implication of such GB potentials on device performance. It is found that hole-majority repulsive potentials are most likely reducing the device efficiency, due to increased GB recombination in the bulk as well as in the space-charge region. A full account of these additional losses was given by the analysis of the recombination processes involved. For large values of ϕ_{gb}, an "ideal" carrier collection is established, however, considering the losses in V_{oc}, no net benefit is achieved.

Electron-repulsive potentials are predicted to increase device efficiency, but they are unlikely to be able to completely passivate active grain boundaries. Such potentials have only been observed for Cu-rich grown $CuGaSe_2$ films and the resulting solar cell performance was poor due to CuSe segregation [147].

Simulation of photoluminescence, near-field scanning microscopy, and electron beam induced current experiments were performed in a collaborative effort with the National Renewable Energy Laboratory [122]. These results showed that hole-repulsive band-bending leads to fast charge separation, very short observed PL lifetimes, and overly long EBIC diffusion lengths, all inconsistent with experimental results and in agreement with the above conclusion that $\phi_{gb} \gg 0$ is an unlikely case to be present in highly-efficient CIGS solar cells.

5.5 Band-discontinuities at grain boundaries

Free surfaces or $Cu(In,Ga)Se_2$ solar cells have been reported to exhibit a Cu-poor composition, and experimentally this Cu-depletion is observed by an enlarged band-gap due to a down-shift of the valence-band maximum [50, 155]. Recent studies have shown that interior surfaces at GBs can be similarly depleted [149] and first-principles calculations of GBs have predicted a suppression of the valence-band edge by 0.2–0.4 eV [148]. It should be noted, however, that these calculations assumed a surface reconstruction pattern that is limited to the first unit cell of the lattice and the resulting widths over which the valence-band edge is suppressed is also very small. Whether and how this links to the experimentally observed depletion that exceeds tens of nanometers in thickness is unclear.

Reproduced with permission of the copyright owner. Further reproduction prohibited without permission.

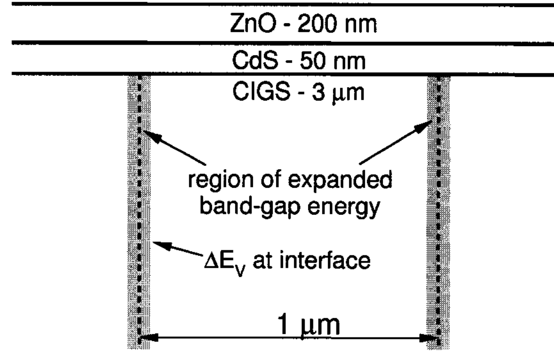

Figure 5.27: Schematic of the valence-band offset model. A distinct region surrounding the GB with enlarged E_g is defined.

The effects of Cu-depletion at GBs is investigated with numerical simulations. Since a continuous expansion of the band-gap cannot be realized with the computer model available, a discrete valence-band offset, ΔE_V, between the grain interior and the grain boundary is used as indicated by the gray area in the schematic in Fig. 5.27.

Case studies of ΔE_V = 0.2 eV and 0.4 eV

The following models are investigated:

1. ΔE_V is fixed at 0.2 eV or 0.4 eV, with $\phi_{gb} = 0$, and S_{gb} varies.

2. GB recombination velocity $S_{gb} = 10^5$ cm/s or 10^6 cm/s and ΔE_V varies.

3. Combinations of GB potentials and valence-band offsets (ϕ_{gb} and ΔE_V); this is calculated for $S_{gb} = 10^5$ cm/s and 10^7 cm/s.

The input (ΔE_V, defects) and output (ϕ_{gb}, η) parameters for representative cases are listed in Table 5.4. The resulting bands and carrier concentrations are shown in Fig. 5.28.

Table 5.4: Input parameters and resulting device efficiency with $S_{gb} = 10^5$ cm/s for ΔE_V = 0.2 eV, +0.4 eV, and $\phi_{gb} = \Delta E_V = 0.2$ eV models; (a) shown for reference.

Fig. 5.28	ΔE_V (eV)	defect	N_{gb} (cm^{-2})	ϕ_{gb} (eV)	η at $S_{gb} = 10^5$ cm/s (%)
(a)	0	-	0	0	13.8
(b)	0.2	-	0	0	16.2
(c)	0.4	-	0	0	17.3
(d)	0.2	donor	4.5×10^{11}	0.2	16.7

Reproduced with permission of the copyright owner. Further reproduction prohibited without permission.

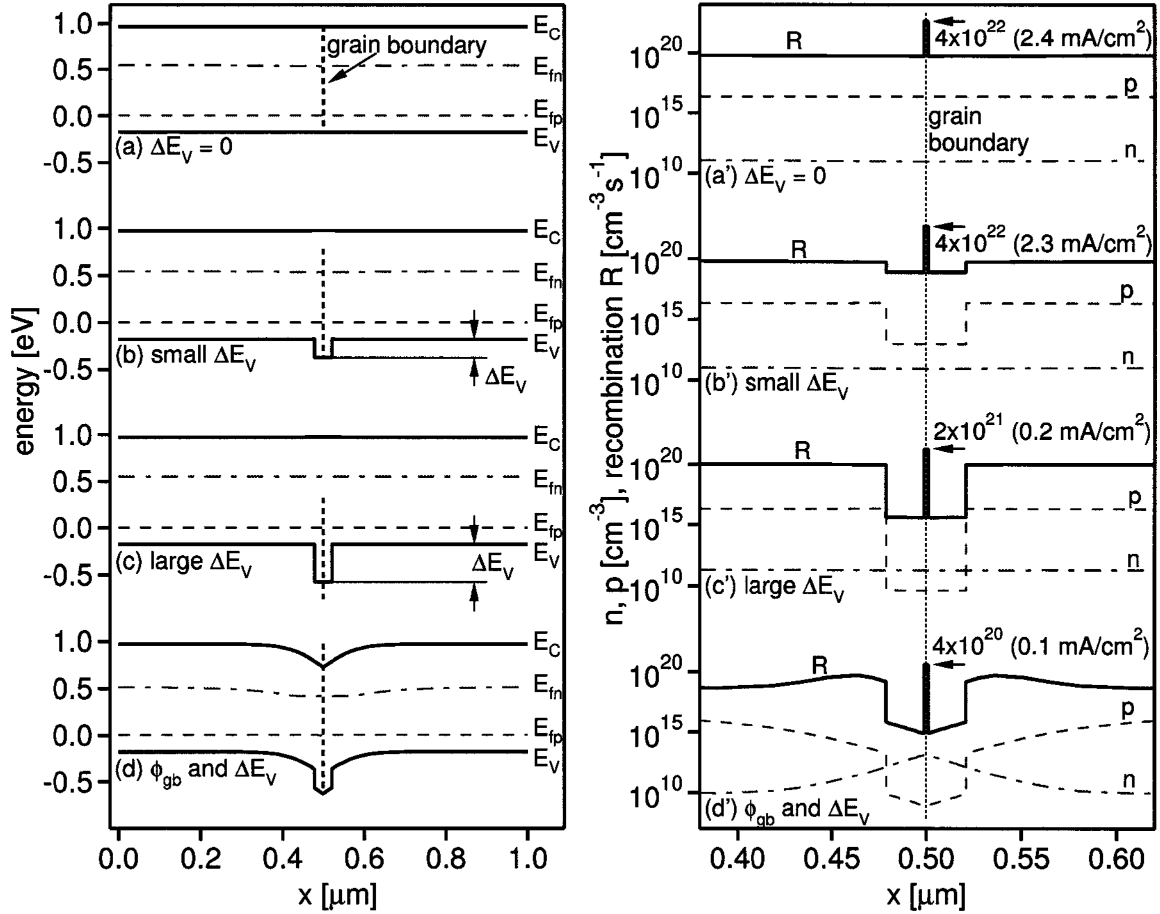

Figure 5.28: Band structure parallel to the main junction at $z = 1\ \mu$m. All cases for columnar GBs at zero external bias under 1 sun illumination: (a) $\Delta E_V = \phi_{gb} = 0$, (b) small ΔE_V, (c) large ΔE_V, and (d) combination of small ϕ_{gb} and ΔE_V. Figures (a')–(d') show the corresponding carrier concentrations and recombination rates (Note the expanded horizontal scale). The sheet density of recombination (cm^{-2}s^{-1}) is found by multiplying R at the GB by the GB width (2 nm). Corresponding integrated current losses are shown in parentheses.

Starting from a CIGS model with columnar GBs (Fig. 5.28[a]), an expansion of the band-gap at the grain surface is included. The doping in this 20-nm thin layer is chosen to be lower than in the bulk, which establishes a flat conduction band and prevents the formation of an electron barrier. The optical absorption is adjusted to the local band gap in this layer as well. However, since this layer is very thin compared to the overall grain size, the effects of reduced absorption are very small. The resulting band structure is shown in Fig. 5.28(b) and (c) for $\Delta E_V = 0.2$ eV and 0.4 eV, respectively. An arbitrary combination of ϕ_{gb} and ΔE_V is also considered, and its band diagram is shown in Fig. 5.28(d).

Reproduced with permission of the copyright owner. Further reproduction prohibited without permission.

A shift in the valence-band energy (Fig. 5.28[b] and [c]) suppresses the hole concentration and leaves the electron concentration unaltered (Fig. 5.28[b'] and [c']). If this shift is sufficiently large, 5.28(c'), holes become the recombination limiting carrier, $p < n$, and GB recombination is significantly reduced with further increases in ΔE_V. Small ΔE_V in combination with small ϕ_{gb} appear to have a similar effect for zero bias GB recombination in the quasi-neutral region (Fig. 5.28 [d']). The current densities in parentheses are the recombination losses integrated over the z direction (perpendicular to the graph).

An important difference between charged (ϕ_{gb}) and charge-free (ΔE_V) models is that although both models lead to hole repulsion, only ϕ_{gb} models attract electron carriers toward the GB. This can lead to enhanced recombination, but also, for $\phi_{gb} > 0.3$ eV, to beneficial "GB collection paths" and increases in J_{sc}. ΔE_V models achieve J_{sc}'s that do not exceed those achieved with GB-free models. Similarly, the comparison between Fig. 5.28(c) and (d): In both cases the valence band is suppressed by 0.4 eV which leads negligible bulk recombination, but only situation 5.28(d) has the possibility of improved collection.

5.5.1 Valence-band offsets

Initially, the conduction-band minimum was left unchanged. J-V results calculated for the entire range of S_{gb} (Fig. 5.29) indicate that small values of ΔE_V allow partial recovery of V_{oc} and FF, but do not significantly affect J_{sc}. Large values of ΔE_V screen the GB in the bulk, and high values of both J_{sc} and V_{oc} are achieved. Substantial improvements are possible with ΔE_V in the presence of active GBs (high S_{gb}) and for $\Delta E_V = 0.4$ eV the performance is equal to the performance of a GB-free device, independent of S_{gb}.

Similar conclusions can be found from calculations of the J-V performance as a function of the parameter ΔE_V for $S_{gb} = 10^5$ cm/s (Fig. 5.30). It is apparent, that ΔE_V strongly affects V_{oc}, and that in the limit of large ΔE_V, V_{oc} identical to GB-free models is achieved. J_{sc} improves once ΔE_V exceeds 0.3 eV and above this value, η is very close to the GB-free baseline. With higher $S_{gb} = 10^6$ cm/s, the losses are greater, but the passivation works equally well, and for ΔE_V above 0.3 eV, GB-free performance is very nearly achieved.

Reproduced with permission of the copyright owner. Further reproduction prohibited without permission.

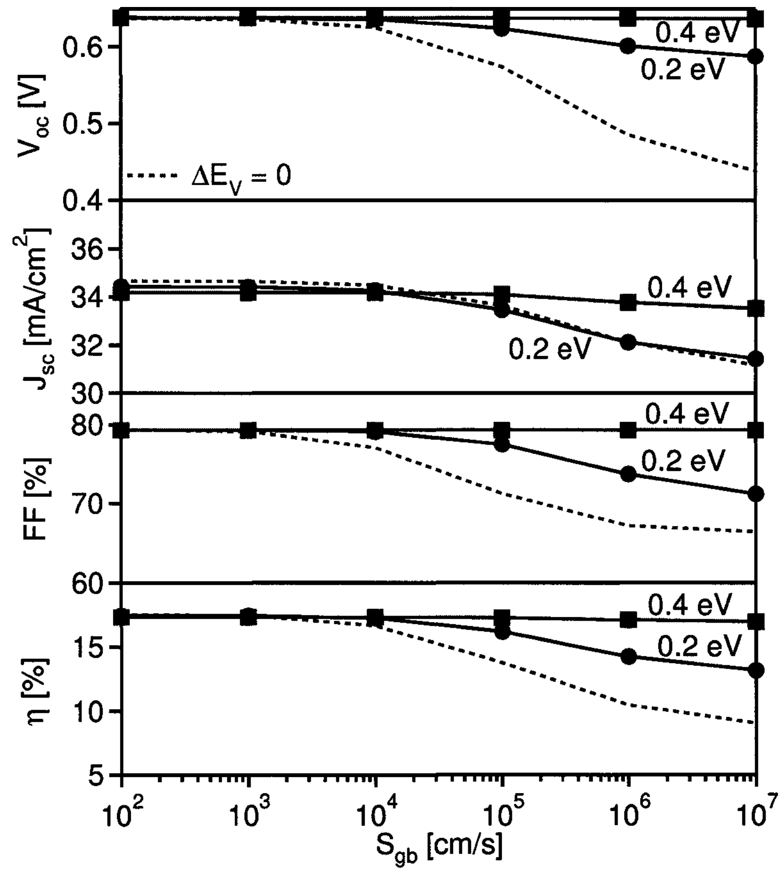

Figure 5.29: *J-V* parameters V_{oc}, J_{sc}, FF, and η for $\Delta E_V = 0.2$ and 0.4 eV. Larger values give identical results to $\Delta E_V = 0.4$.

Reproduced with permission of the copyright owner. Further reproduction prohibited without permission.

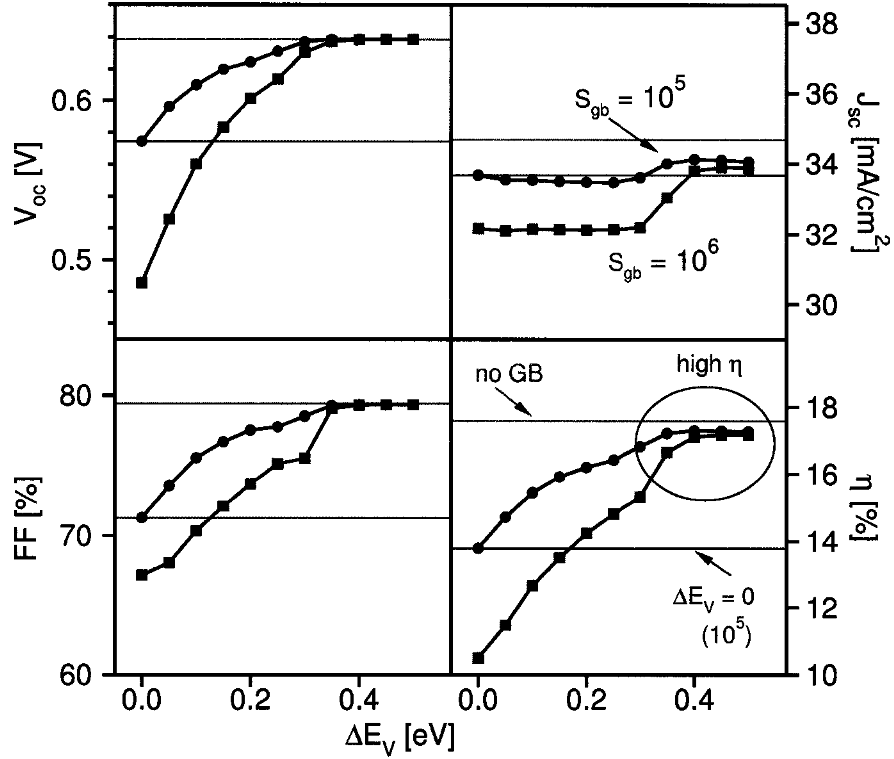

Figure 5.30: *J-V* parameters V_{oc}, J_{sc}, FF, and η for $S_{gb} = 10^5$ cm/s and 10^6 cm/s.

In contrast to the charged grain boundaries (Sect. 5.4.1), however, the ideal collection achieved for large values of ϕ_{gb} (Fig. 5.20 on p. 104) is not achieved by incorporating the valence-band offset.

Discussion

Valence-band offsets suppress holes from the GB, but the electron concentration is unaffected, Fig. 5.28(b, c). With $\Delta E_V > 0.3$ eV, the GB is effectively screened against bulk recombination, because insufficient holes are present (Fig. 5.28[d] and 5.31[a]). In this situation, holes are minority carriers at the GB and their concentration controls the recombination process. For the given model ($m_h/m_0 = 0.8$, $p = 2\times10^{16}$ cm^{-3}, $n_{one-sun} \sim 10^{11}$ cm^{-3}), fully effective screening occurs when ΔE_V exceeds 0.3 eV. If the GB recombination velocity is very high (comparable to the thermal velocity), the thermionic emission across the valence-band offset can become an additional limiting process.

Recombination remains low under forward bias and no significant SCR peak is observed

Reproduced with permission of the copyright owner. Further reproduction prohibited without permission.

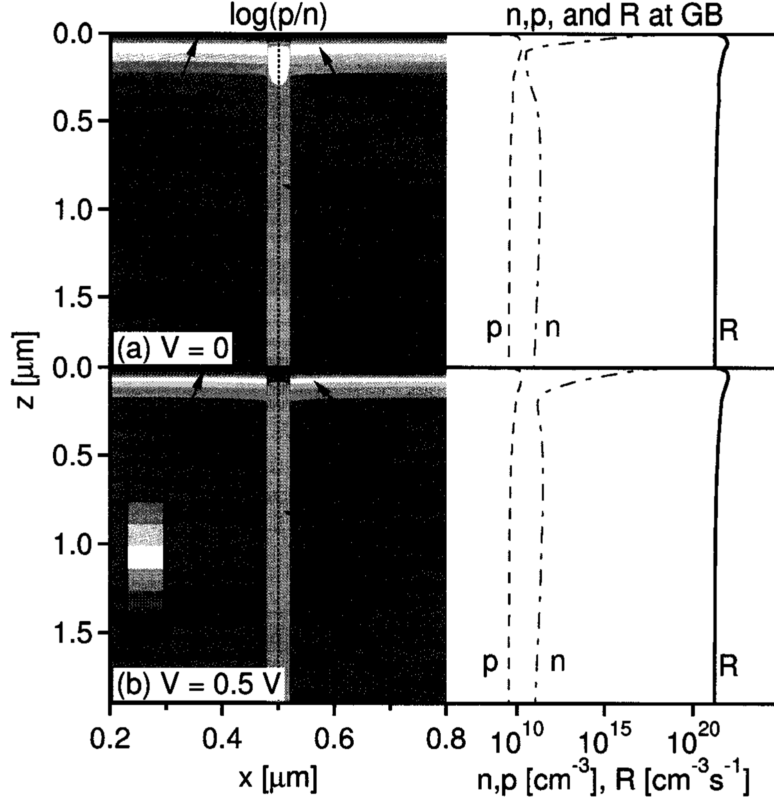

Figure 5.31: Large valence-band offset (0.4 eV), $S_{gb} = 10^5$ cm/s. Relative carrier concentration in the 2D model (left) and n, p, and recombination R at the GB (right) under one-sun illumination at (a) $V = 0$ and (b) $V = 0.5$ V (slightly below V_{oc})

at either zero or positive bias (Fig. 5.31[b]). Recombination of electrically injected carriers is affected by even small values of ΔE_V, because the band gap expands locally at the grain boundary and an increased band gap leads to reduced SRH recombination. This improves both V_{oc} and FF. Under forward bias $np \gg n_i^2$, and the electrically injected carrier density exceeds that which is optically generated. Under these conditions

$$np \simeq N_C N_V e^{-E_g/kT} e^{qV/kT}. \tag{5.20}$$

The dominant recombination occurs in the SCR where $n \sim p$. The band gap at the GB expands with increasing valence-band offset ($E_g^{GB} = E_g^{bulk} + \Delta E_V$) and, therefore, Eq. 5.16 can be rewritten for V_{oc}-relevant recombination:

$$R_{gb}(\Delta E_V) = R_{gb}(0) e^{\left(\frac{-\Delta E_V}{2kT}\right)} \tag{5.21}$$

Reproduced with permission of the copyright owner. Further reproduction prohibited without permission.

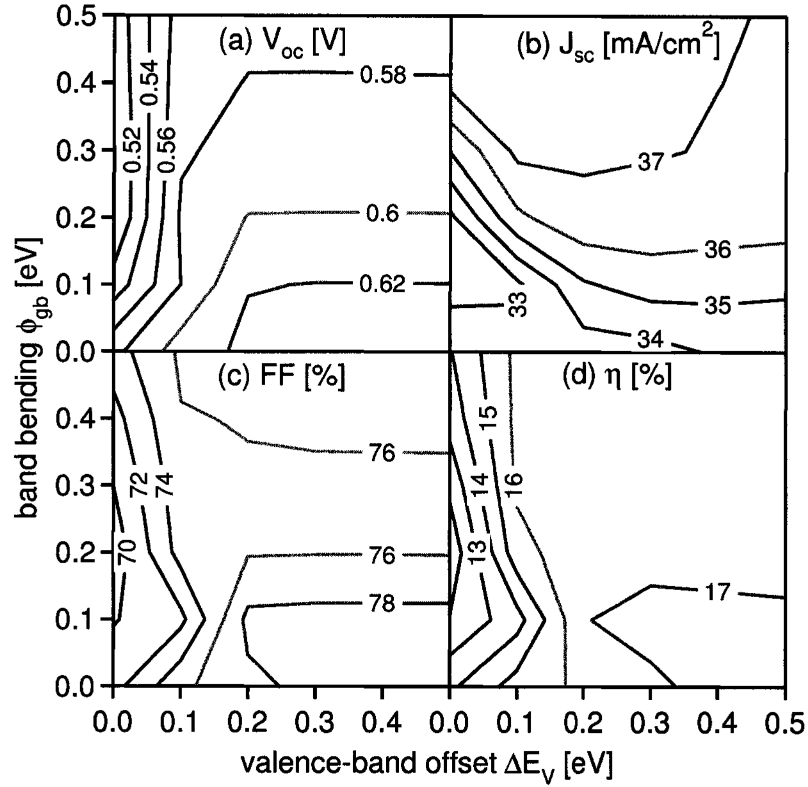

Figure 5.32: Valence-band offset ΔE_V and band-bending ϕ_{gb}. $S_{gb} = 10^5$ cm/s.

According to Eq. 5.21, increasing the band gap toward the grain surface by 0.3 eV lowers the effective recombination velocity in the SCR to less than 1% of its original value. A moderate quality GB ($S_{gb} = 10^5$ cm/s) would therefore be effectively passivated (effective $S_{gb} < 10^3$ cm/s) in terms of SCR recombination.

5.5.2 Combination of valence-band offsets and charged grain boundaries

The existence of the valence-band down-shift does not exclude the possibility of charge-induced band-bending, as well. The current-voltage parameters corresponding to models that incorporate hole-repulsive band-bending and valence-band offsets are shown in a contour-plot format in Fig. 5.32. These results were calculated for $S_{gb} = 10^5$ cm/s.

Nearly independent of the band-bending, high solar-cell efficiency is only possible once ΔE_V exceeds 0.2 eV, which is sufficient to suppress most of the forward current recombination and, hence, allow a high open-circuit voltage. The short-circuit current density is high for all combinations that have $\Delta E_V + \phi_{gb} > 0.3$ eV (downward 45° lines in Fig. 5.32[b]).

Reproduced with permission of the copyright owner. Further reproduction prohibited without permission.

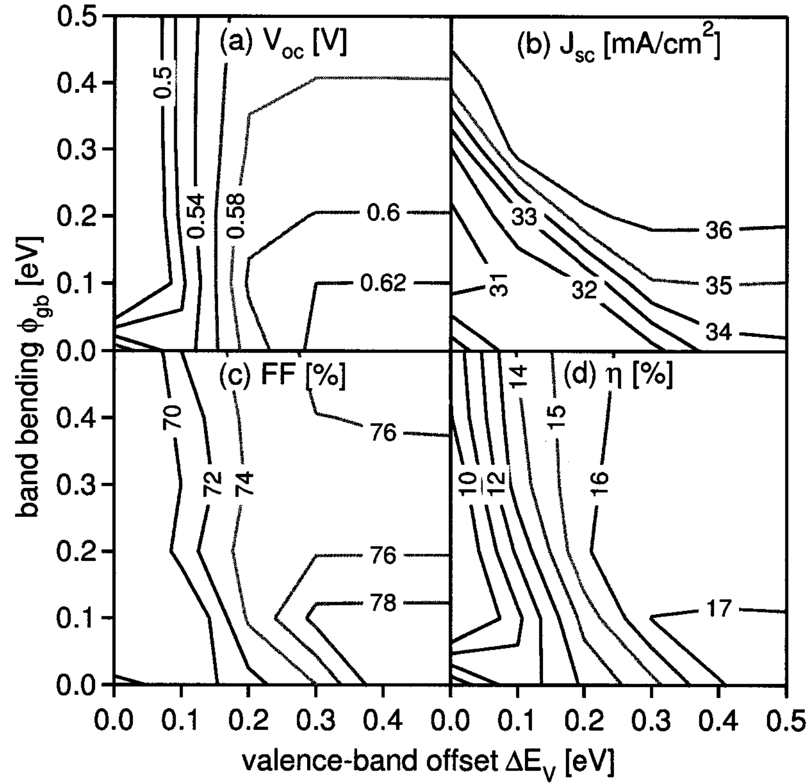

Figure 5.33: Valence-band offset ΔE_V and band-bending ϕ_{gb}. $S_{gb} = 10^7$ cm/s.

For the purpose of passivating against bulk recombination, both mechanisms are similarly useful at zero bias. Higher values of ϕ_{gb} show their beneficial effect on carrier collection, yet, even in the presence of large valence-band offsets, lead to some reduction in V_{oc}.

For a last comparison, the trade-off between ΔE_V and ϕ_{gb} is evaluated for cells of very poor quality from the GB perspective ($S_{gb} = 10^7$ cm/s). Figure 5.33 shows the J-V results for these cases. The highest achieved efficiency is over 17% when ΔE_V is above 0.3 eV. Large band-bending again results in better current collection (higher J_{sc} for $\phi_{gb} > 0.2$ eV), but V_{oc} is lowered by its presence. There is a narrow region in the parameter space around $\Delta E_V = 0.25$ eV in which additional small ϕ_{gb} has a beneficial effect on device performance. This situation is easily interpreted: the ΔE_V results in SCR passivation and high V_{oc}, whereas the additional small ϕ_{gb} helps to invert the GBs in the quasi-neutral region and, hence, to increase J_{sc}.

Based on Fig. 5.32 and 5.33 it is concluded that, for the models considered, high ΔE_V is the most effective means to passivate active GBs and attain high efficiencies, whereas

Reproduced with permission of the copyright owner. Further reproduction prohibited without permission.

modest ϕ_{gb} can also be present without significantly affecting device performance. ϕ_{gb} alone, however, limits the efficiency to below 14% and 10% for $S_{gb} = 10^5$ and 10^7 cm/s, respectively.

5.5.3 Summary

A number of arguments suggest that Cu-depletion that leads to a down-shift of the valence-band edge might be present at GB in Cu(In,Ga)Se_2 solar cells. In this section, it has been shown that such chemical induced hole repulsion would lead to an excellent passivation of GBs in the SCR as well as in the quasi-neutral bulk region. Although any magnitude of ΔE_V is beneficial, it must exceed 0.3 eV to provide fully effective passivation.

A combination of GB potentials and Cu-depletion may well be present at GBs. It has been shown here that with combinations of ϕ_{gb} and ΔE_V, the beneficial effect clearly lies with the valence-band shift. GB potentials, particularly in the absence of a passivating valence-band offset, are likely to be detrimental to the performance.

5.6 Short-comings of the GB models

Although this work used advanced numerical simulations, there are some limitations that have not been addressed. Some of these certainly affect the details of the simulations, but are not likely to alter the general results.

2D vs. 3D

The model is two-dimensional. In three dimensions, (a) the same value of S_{gb} will be more detrimental because there is a higher number of GBs/volume (this was partially discussed in Sect. 5.3.4); (b) the collection effect seen for large ϕ_{gb} may be enhanced, because the average distance carriers have to travel to the GB is reduced; and (c) the V_{oc}-loss introduced by positively charged defects will be even larger, because the junction widening and increase in forward current will be, at least to some degree, additive where two grain boundaries intersect.

Reproduced with permission of the copyright owner. Further reproduction prohibited without permission.

Geometry

A simplified geometry has been used. Real solar cells have many, maybe intersecting, grain boundaries and grain sizes vary from grain to grain. Therefore, it would be desirable to consider more complex structures, as well. The hole-blocking mechanism discussed above could have highly negative consequences for horizontal GBs, because the device operation depends on hole current flow perpendicular to the junction. Also, it is likely that GBs are not all identical and that GBs may be non-uniform from top to bottom of the film.

Parameter input

There are uncertainties associated with the input parameters. Some bulk parameters, e.g., bulk mobilities, are not accurately known and were used as "best guess" values. These uncertainties are not likely to have a significant effect within a reasonable parameter range. However, the underlying GB-free baseline corresponds to a highly efficient CIGS solar cells and results may be significantly different if lower efficiency solar cells are considered. For example, from the results presented, the possibility that large GB potentials are present in moderate quality solar cells can not be excluded. It is indeed possible that such lower-efficiency solar cells may benefit more in current collection then they suffer from additional losses in photovoltage.

With respect to particular GB models, one significant unknown in ϕ_{gb} models is the characteristic energy of the charged donor level. In all simulations that included positively charged GBs, the donor level has been assumed 0.2 eV below the conduction-band edge. As discussed in Sect. 5.4.2, the energetic depth of the defect level, $E_C - E_T$, places an upper bound on the achievable zero bias band bending; 0.2 eV was used, because it allows $\phi_{gb} =$ 0–0.6 eV to be established, while at the same time, it is not extremely shallow. The latter would appear somewhat inconsistent with theoretically predicted energy levels [29] and the limited n-type dopability of CIGS material [103]. The influence of this donor level location on device performance is shown in Fig. 5.34.

For small values of $N_{gb} = 4.5\text{x}10^{11}$ cm^{-3}, and hence, small values of resulting ϕ_{gb}, the GB potential as well as the resulting J-V performance is independent of the characteristic

Reproduced with permission of the copyright owner. Further reproduction prohibited without permission.

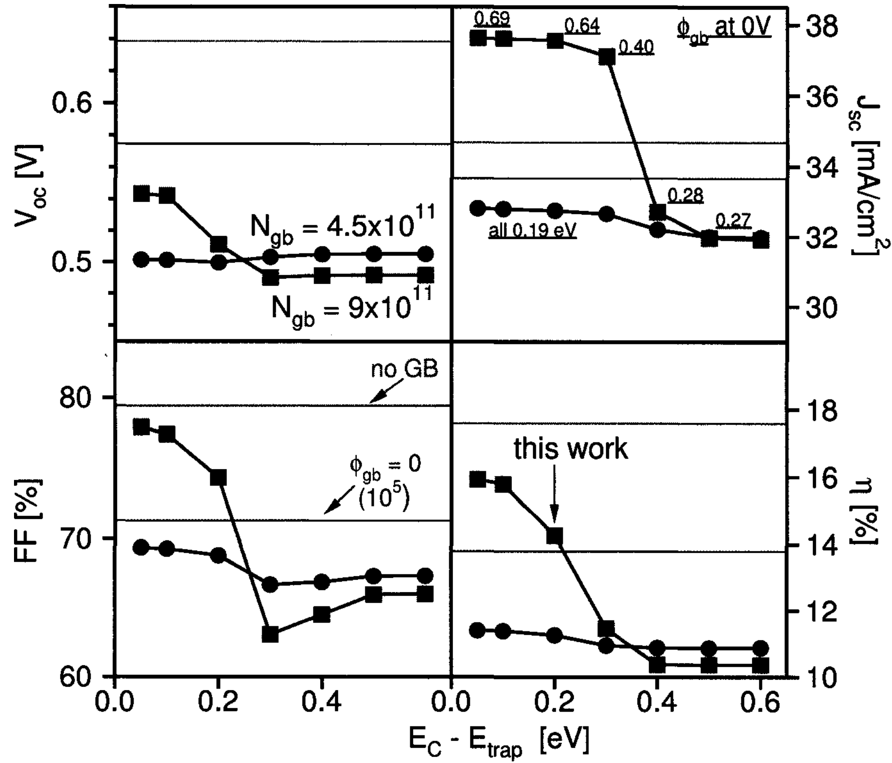

Figure 5.34: Device performance with variation of the donor characteristic energy $E_C - E_T$. $S_{gb} = 10^5$ cm/s. The defect densities shown corresponds to the two case studies, $\phi_{gb} = 0.2$ and 0.6 eV, discussed in Sect. 5.4

energy. High GB state density can only establish large ϕ_{gb} if the levels are reasonably shallow. The zero voltage values of ϕ_{gb} are given in the J_{sc} plot of Fig. 5.34. It should be noted, however, that very shallow levels in very high densities could lead to an overall increase in device performance (Fig. 5.34[d]) compared to unpassivated GBs. The requirements, however, are fairly strict: very high density of states, located very close to the conduction-band minimum. A similar configuration was used in Ref. [122] and was shown to be inconsistent with experimental results.

The Cu-depleted region, with expanded band-gap energy, in the ΔE_V models was assumed with a thickness of 20 nm. There is at least some experimental evidence that this Cu depletion extends several tens of nanometers or more into the bulk, because it was observed by micro-Auger electron spectroscopy measurements [149]. The modeling results are generally insensitive to the thickness of this layer, but for very thin layers, quantum effects might play an important role. The tunneling probability can be estimated by WKB

Reproduced with permission of the copyright owner. Further reproduction prohibited without permission.

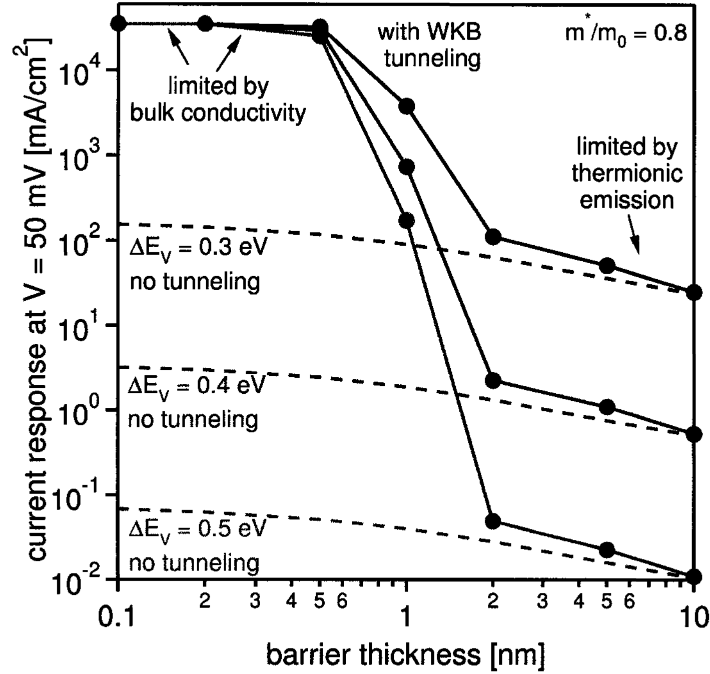

Figure 5.35: Tunneling through a rectangular barrier. For thick barriers transport is limited by the thermionic emission across the barrier (dashed lines indicated the response for thin barriers is tunneling is neglected). Including WKB approximations, current flows though the barrier once it thickness is less than 1 nm.

approximations. Figure 5.35 shows the transport through valence-band barriers with heights of 0.3–0.5 eV. Relatively independent of the barrier height, the transition between transport limited by bulk conductivity and that limited by tunneling through the barrier occurs around 2 nm. The experimental observation of Cu depletion at GBs [149] and free surfaces [50, 155] suggests that the Cu depletion region has substantial thickness, and hence, direct tunneling can be safely ignored.

5.7 Summary

Two-dimensional models were employed to study the effects of grain boundaries on CIGS solar cells. Neutral GBs were investigated in limits, perpendicular or parallel to the main junction, and the qualitative results agree well with previous work. Detailed simulations allow deduction of the exact quantitative impact of GB recombination on solar-cell performance. Columnar GBs that are present in all thin-films are found to be an efficiency limiting factor ($\eta < 17\%$) for an effective $S_{gb} \geqslant 10^4$ cm/s. Strong space-charge-region

Reproduced with permission of the copyright owner. Further reproduction prohibited without permission.

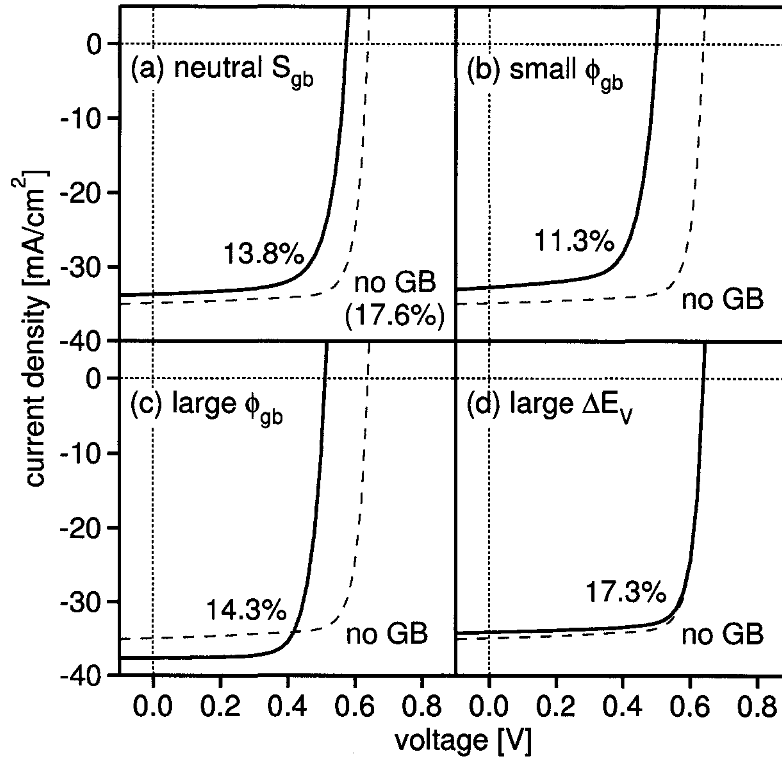

Figure 5.36: Typical current-voltage curves for (a) neutral GB recombination, (b) small hole-repelling band-bending, (c) large hole-repelling band-bending, and (d) large valence-band offsets. $S_{gb} = 10^5$ cm/s.

recombination leads to V_{oc} reductions, whereas GBs in the quasi-neutral region affect only carrier collection. Sections of GBs deeper than 1 μm were shown to not affect performance.

GB recombination is further strongly modified by electrostatic potentials at GBs, or by the Cu depletion observed for CIGS thin-films. Results summarizing the cases considered are shown in Fig. 5.36:

(a) Neutral grain-boundary recombination substantially reduces solar-cell efficiency.

(b) Charged defects that lead to weak hole repulsion at the GB cause additional losses in V_{oc} and J_{sc}.

(c) With large band-bending, a high collection efficiency is observed, yet, no net gain in efficiency is achieved due to the reduced voltage.

(d) Valence-band offsets can suppress grain-boundary recombination in the SCR and establish performance similar to GB-free devices.

Reproduced with permission of the copyright owner. Further reproduction prohibited without permission.

This picture is in disagreement with earlier work by Taretto et al. [140] who found that a shift in the valence-band energy led to only a slight increase in efficiency. This discrepancy can be at least partially explained by the two-dimensional model used in Ref. [140] that was limited to the CIGS absorber layer, neglected the blocking effect of the valence offset, and mimicked hole suppression up to 0.18 eV by a reduction in the hole capture-cross section.

The impact on CIGS solar-cell performance from a large spectrum of possible recombination velocities, charge-induced barriers, and valence-band offsets at or near a grain boundary have been evaluated. From the cases considered, there are specific options available to explain record efficiencies close to 20% for CIGS solar cells:

(a) GB recombination that is inherently very small ($\ll 10^4$ cm/s).

(b) Electron-barrier passivation, i.e., a very high acceptor density at the grain boundary.

(c) A valence-band offset (down-shift) greater than 0.3 eV.

(d) A combination of such a valence-band offset and modest hole-repulsive band-bending.

From the results presented, it is concluded that the valence-band offset included in options (c) and (d) is the factor most likely to minimize the impact of grain boundaries on high-efficiency CIGS solar cells.

Reproduced with permission of the copyright owner. Further reproduction prohibited without permission.

Chapter 6

Conclusions

Solar cells are an important developing market for a number of reasons, and it is time well spent to improve upon thin-film solar cells, often labeled as "second generation." As we, as individuals, society, or humanity, face the consequences of our current energy demands and turn toward alternatives, thin-film solar cells may well be the largest contributor in solving the energy problem.

The basics of semiconductor physics and thin-film technologies were reviewed in the introduction of this work. The mathematical complexity requires that the problem must in general be addressed numerically, and a number of software programs are available for this task that were briefly reviewed in Chapter 3. Baseline cases for ZnO/CdS/CIGS and SnO_2/CdS/CdTe solar cells were established following two guidelines: that the baselines be as general as possible, yet, accurate enough that they are representative of many, if not most, experimental devices with only minor additional modifications. Further, a high-to-low approach was taken, in that the baselines were intentionally aligned with highly-efficient experimental solar cells, assuming that additional detrimental elements will reflect accurately on particular devices.

The main results of this work, presented in Chapter 4 and 5, have been summarized at the end of each section and shall not be reiterated here. This final discussion is used to link these results to state-of-the-art of experimental devices and highlight where this work has substantially contributed to their understanding.

Reproduced with permission of the copyright owner. Further reproduction prohibited without permission.

ZnO/CdS/CI(G)S solar cells

The idea of thin-film solar cells goes almost as far back as the invention of solar cells. From the early days of solar-energy conversion, it was obvious that to substantially contribute to the energy requirement of our society, solar cells will be needed in large or huge scale applications. Many different material systems and combinations have been tested over the last five decades, but no other system has shown performance as high as ZnO/CdS/CIGS solar cells. The discussion of the interface properties in Section 4.2 has given some insight on part of the reason behind this inherent quality: the positive band-offset between CdS and low-Ga $Cu(In,Ga)Se_2$ inherently passivates against interface recombination. The results in Sect. 4.3 have shown that in the case of CdS/CIS or low-Ga CIGS, the same positive band offset can sometimes lead to observable non-superposition or current blockage. Only, in extreme cases, however, does this influence regular J-V performance. The most important results with respect to the CdS buffer layer, however, is found in the Sect. 4.2, where it is predicted that wider-band-gap $Cu(In,Ga)Se_2$ solar cells will lose this benefit of inherent passivation as Ga is added to replace In, and high device efficiencies will not be achievable even if all other obstacles related to these materials can be overcome.

$Cu(In,Ga)Se_2$ material

The study of grain boundaries reported in Chapter 5 gives the first basic understanding of how GB recombination, potentials, and possible Cu-depletion at GBs can affect device performance. This study establishes a connection between theoretically predicted properties, material studies, and observed device performance. These results challenge the claims by others that large GB potentials are beneficial to device performance and that GB potentials are the reason behind the superiority of $Cu(In,Ga)Se_2$ solar cells. Studies of the free absorber surface, without prior air-exposure, are necessary, and ideally new experiments need to be designed to determine the electronic properties in the bulk, i.e., potential variations at GBs beneath the surface.

Cu depletion has been experimentally observed at the free surface, and similar characteristics at GBs have been reported recently. This work has shown, that such depletion

Reproduced with permission of the copyright owner. Further reproduction prohibited without permission.

can be greatly beneficial to device performance. GBs are effectively passivated and in fact this can explain why Cu(In,Ga)Se_2 achieve efficiencies close to 20%, previously believed to be only accessible for high quality crystalline materials. One question that has not been addressed in this work, is the dependence of CIGS growth, and the subsequent enhancement in cell performance, on the presence of Na. From the device-model point of view, it is not known where this Na resides in the film, and whether it acts as a bulk defect or dopant, passivates GBs, or simply enhances the crystal growth. Theoretical studies have shown, however, that Na can affect grain-boundaries similarly to Cu-depletion in that it leads to a valence-band suppression. Further consideration of Na effects should be addressed once the exact influences of Na on the electronic structure are known.

Three-stage processing and its benefits

Efficiencies above 18% are exclusively achieved by the NREL three-stage process. It has often been suggested that the Ga/(Ga+In) grading, which is automatically introduced in this process, is the major contributor to the observed superiority. The study in Sect. 4.1 showed that only a modest increase in efficiency (~1%) can be attributed to the incorporation of Ga/(Ga+In) grading. Therefore, it is likely that the three-stage process has substantial other advantages, which have not been recognized so far. Applying the results of Chapter 5, it can be speculated that the thee-stage process enhances the depletion of Cu at the CdS/CIGS interface and at the grain boundaries close to the film surface. This characteristic is built into the process as the growth is finished with a Cu-poor phase. The bulk of the material may or may not be similarly deficient in Cu at GBs, but if it is, some additional GB potential could in fact be beneficial. This scenario is compatible with the small grain boundary potentials measured on air-exposed CIGS films, the observed Cu-depletion, and the resulting device performance.

Where does the technology go next?

The technology is facing several challenges:

1. Thinner absorber layers. Calculations with thin absorber layers (Sect. 4.1) show that

Reproduced with permission of the copyright owner. Further reproduction prohibited without permission.

substantial thinning of the absorber should be possible without major losses in device efficiency. These calculations and related experimental evidence, however, only serve as a first proof of concept, as the problems that are associated with thinning are in large part related to growth and material issues.

2. Alternative buffer and window layers. New materials are necessary for several reasons: (a) minimization of current losses by window and buffer absorption (replace CdS), (b) establishment of favorable band-offsets for wider-band-gap CIGS (Sect. 4.2), and (c) use as transparent *front and back* contacts in tandem devices.

3. High-Ga $Cu(In,Ga)Se_2$. These devices are investigated, because (a) high-voltage low-current solar cells lead to lower resistive losses in module integration, (b) based on the solar spectrum, a higher band-gap results in higher efficiencies as the trade-off between V_{oc} and J_{sc} is favorable up to band-gap energies around 1.4 eV (Sect. 4.2), and (c) a high band-gap CIGS or CGS solar cells is required as a top cell in tandem configurations.

4. Thin-film tandem cells. This very challenging topic has become a major field of research within the recently established High Performance Project of the US Department of Energy. This will require a stable and efficient top and bottom cell, both integrated mechanically or monolithically into one package. There are many milestones to take, besides points (2) and (3) in this list to achieve the very ambitious program goal of 25% device efficiency by 2010.

This work identified and quantified, both beneficial and detrimental mechanisms in $Cu(In,Ga)Se_2$ solar cells. The results give directions on how the existing problems can be overcome and how this highly-promising technology can reach its full potential.

Reproduced with permission of the copyright owner. Further reproduction prohibited without permission.

Appendix A

Tabulated spectral input for the CIGS baseline

Table A.1: AM1.5 illumination spectrum ($\Phi_{AM1.5}$) and absorption spectra (α) for ZnO, CdS, and 1.15 eV-CIGS layers.

λ (μm)	$\Phi_{Am1.5}$ (#/cm^{2}s)	α_{ZnO} (1/cm)	α_{CdS} (1/cm)	α_{CIGS} (1/cm)
0.30	8.93E+13	2.00E+04	2.70E+05	3.69E+05
0.32	6.13E+14	2.00E+04	2.20E+05	3.69E+05
0.34	1.46E+15	2.00E+04	1.80E+05	3.69E+05
0.36	1.99E+15	2.00E+04	1.50E+05	3.69E+05
0.38	2.69E+15	2.00E+04	1.30E+05	3.69E+05
0.40	3.94E+15	2.00E+03	1.20E+05	3.64E+05
0.42	4.85E+15	2.00E+02	1.05E+05	3.30E+05
0.44	5.76E+15	6.00E+01	9.80E+04	2.67E+05
0.46	7.29E+15	1.00E+00	8.50E+04	2.14E+05
0.48	7.69E+15		7.00E+04	1.83E+05
0.50	7.82E+15		4.30E+04	1.58E+05
0.52	8.01E+15		1.60E+04	1.41E+05
0.54	8.46E+15		1.00E+02	1.28E+05
0.56	8.62E+15		1.00E+00	1.18E+05
0.58	8.44E+15			1.08E+05
0.60	8.69E+15			1.01E+05
0.62	9.09E+15			9.53E+04

continued on next page

Reproduced with permission of the copyright owner. Further reproduction prohibited without permission.

Table A.1: *continued*

λ (μm)	$\Phi_{Am1.5}$ (#/cm^{2}s)	α_{ZnO} (1/cm)	α_{CdS} (1/cm)	α_{CIGS} (1/cm)
0.64	9.18E+15			8.77E+04
0.66	9.32E+15			8.31E+04
0.68	8.60E+15			7.86E+04
0.70	8.61E+15			7.35E+04
0.72	7.40E+15			6.87E+04
0.74	9.03E+15			6.55E+04
0.76	7.36E+15			6.23E+04
0.78	8.88E+15			5.93E+04
0.80	8.72E+15			5.65E+04
0.82	6.75E+15			5.30E+04
0.84	8.13E+15			4.94E+04
0.86	8.49E+15			4.60E+04
0.88	8.28E+15			4.11E+04
0.90	7.12E+15			3.72E+04
0.92	6.28E+15			3.55E+04
0.94	2.11E+15			3.32E+04
0.96	4.00E+15			3.09E+04
0.98	6.04E+15			2.84E+04
1.00	7.30E+15			2.52E+04
1.02	7.46E+15			2.11E+04
1.04	7.23E+15			1.67E+04
1.06	7.00E+15			1.24E+04
1.08	6.82E+15			7.00E+03
1.10	4.56E+15			2.95E+03
1.12	6.28E+14			9.44E+02
1.14	3.65E+15			3.02E+02
1.16	3.98E+15			9.66E+01
1.18	5.46E+15			3.09E+01
1.20	5.22E+15			9.88E+00
1.22	5.50E+15			3.16E+00
1.24	5.98E+15			1.00E+00

Reproduced with permission of the copyright owner. Further reproduction prohibited without permission.

Appendix B

Tabulated spectral input for the CdTe baseline

Table B.1: AM1.5 illumination spectrum ($\Phi_{AM1.5}$) and absorption spectra (α) for SnO_2, CdS, and CdTe layers.

λ (μm)	$\Phi_{Am1.5}$ (#/cm^{2}s)	α_{SnO_2} (1/cm)	α_{CdS} (1/cm)	α_{CdTe} (1/cm)
0.30	8.93E+13	7.89E+04	2.70E+05	3.50E+05
0.32	6.13E+14	5.08E+04	2.20E+05	3.10E+05
0.34	1.46E+15	1.71E+04	1.80E+05	2.80E+05
0.36	1.99E+15	2.00E+03	1.50E+05	2.50E+05
0.38	2.69E+15	1.00E+02	1.30E+05	2.10E+05
0.40	3.94E+15	1.00E+00	1.20E+05	1.80E+05
0.42	4.85E+15		1.05E+05	1.60E+05
0.44	5.76E+15		9.80E+04	1.40E+05
0.46	7.29E+15		8.50E+04	1.20E+05
0.48	7.69E+15		7.00E+04	1.00E+05
0.50	7.82E+15		4.30E+04	9.00E+04
0.52	8.01E+15		1.60E+04	8.00E+04
0.54	8.46E+15		1.00E+02	7.00E+04
0.56	8.62E+15		1.00E+00	6.40E+04
0.58	8.44E+15			5.80E+04
0.60	8.69E+15			5.30E+04
0.62	9.09E+15			4.90E+04

continued on next page

Reproduced with permission of the copyright owner. Further reproduction prohibited without permission.

Table B.1: *continued*

λ (μm)	$\Phi_{Am1.5}$ (#/cm^{2}s)	α_{SnO_2} (1/cm)	α_{CdS} (1/cm)	α_{CdTe} (1/cm)
0.64	9.18E+15			4.50E+04
0.66	9.32E+15			4.10E+04
0.68	8.60E+15			3.80E+04
0.70	8.61E+15			3.60E+04
0.72	7.40E+15			3.30E+04
0.74	9.03E+15			3.10E+04
0.76	7.36E+15			2.90E+04
0.78	8.88E+15			2.50E+04
0.80	8.72E+15			1.50E+04
0.82	6.75E+15			6.00E+03
0.84	8.13E+15			8.00E+02
0.86	8.49E+15			1.00E+00

Reproduced with permission of the copyright owner. Further reproduction prohibited without permission.

List of Publications

- A. O. Pudov, **M. Gloeckler**, S. H. Demtsu, J. R. Sites, K. L. Barth, R. A. Enzenroth, and W. S. Sampath, *Effect of back-contact copper concentration on CdTe cell operation*, in Proc. 29th IEEE Photovoltaic Specialist Conf., 760 (2002).

- **M. Gloeckler**, C. R. Jenkins, and J. R. Sites, *Explanation of light/dark superposition failure in CIGS solar cells*, Mat. Res. Soc. Symp. Proc. 763, 231 (2003).

- C. Jenkins, A. Pudov, **M. Gloeckler**, S. Demtsu, T. Nagle, A. L. Fahrenbruch, and J. R. Sites, *CdTe back contact: response to copper addition and out diffusion*, in Proc. NCPV and Solar Program Review Meeting, 900 (2003).

- **M. Gloeckler**, A. L. Fahrenbruch, and J. R. Sites, *Numerical modeling of CIGS and CdTe solar cells: setting the baseline*, in Proc. 3rd World Conf. Photovoltaic Energy Conversion, 491 (2003).

- **M. Gloeckler** and J. R. Sites, *Apparent quantum efficiency of CdTe solar cells*, J. Appl. Phys. 95, 4438 (2004).

- **M. Gloeckler** and J. R. Sites, *Quantum efficiency of CdTe solar cells in forward bias*, in Proc. 19th European Photovoltaic Sol. Energy Conf. (2004).

- C. R. Corwine, A. O. Pudov, **M. Gloeckler**, S. H. Demtsu, and J. R. Sites, *Copper inclusion and migration from the back contact in CdTe solar cells*, Sol. Energy Mat. Sol. Cells 82, 481 (2004).

- **M. Gloeckler** and J. R. Sites, *Efficiency limitations for wide-band-gap chalcopyrite solar cells*, Thin Solid Films 480–481, 241 (2005)

- J. R. Sites and **M. Gloeckler**, *CdTe and CIGS simulations: when are they helpful?*, in Proc. NCPV and Solar Program Review Meeting (2004).

- **M. Gloeckler** and J. R. Sites, *Band-gap grading of CIGS solar cells*, in press, J. Phys. Chem. Solids (2005).

- T. Schulmeyer, **M. Gloeckler**, R. Kniese, W. Witte, M. Powalla, and A. Klein, *Capacitance spectroscopy of $Cu(In,Ga)Se_2$ solar cells*, in Proc. 20th European Photovoltaic Sol. Energy Conf. (2005).

Reproduced with permission of the copyright owner. Further reproduction prohibited without permission.

- **M. Gloeckler**, W. K. Metzger, and J. R. Sites, *Simulation of polycrystalline $Cu(In,Ga)Se_2$ solar cells in two dimensions*, Mat. Res. Soc. Symp. Proc. 865 (2005).

- W. K. Metzger, **M. Gloeckler**, and R. K. Ahrenkiel, *Two-dimensional and multi-dimensional modeling of polycrystalline $Cu(In,Ga)Se_2$ solar cells*, Mat. Res. Soc. Symp. Proc. 865 (2005).

- A. Kanevce, **M. Gloeckler**, A. Pudov, and J. R. Sites, *Conduction-band-offset rule governing J-V distortion in CdS/CI(G)S solar cells*, Mat. Res. Soc. Symp. Proc. 865 (2005).

- **M. Gloeckler**, W. K. Metzger, and J. R. Sites, *Grain-boundary recombination in $Cu(In,Ga)Se_2$ solar cells*, submitted to J. Appl. Phys. (2005).

- W. K. Metzger and **M. Gloeckler**, *The impact of charged grain boundaries on thin-film solar cells and characterization*, to be published.

Reproduced with permission of the copyright owner. Further reproduction prohibited without permission.

Bibliography

[1] *Random House Unabridged Dictionary, Copyright © 1997, by Random House, Inc., on Infoplease*, URL www.infoplease.com.

[2] Solarbuzz, *Marketbuzz 2005: Annual world solar photovoltaic (PV) market report*, URL http://www.solarbuzz.com/Marketbuzz2005-intro.htm.

[3] T. Surek, in *Proc. 3rd World Conf. Photovoltaic Energy Conversion* (2003), p. 8PL–E3–01.

[4] M. A. Green, in *Proc. 3rd World Conf. Photovoltaic Energy Conversion* (2003), p. OPL–02.

[5] Bundesministerium für Umwelt, Naturschutz und Reaktorsicherheit, *Gesetz zur Neuregelung des Rechts der Erneuerbaren Energien im Strombereich*, URL http://www.bmu.de/erneuerbare/energien/doc/5982.php.

[6] National Renewable Energy Laboratory, *What is the energy payback for PV?*, URL http://www.nrel.gov/docs/fy04osti/35489.pdf.

[7] National Renewable Energy Laboratory, *Will we have enough materials for energy-significant PV production?*, URL http://www.nrel.gov/docs/fy04osti/35098.pdf.

[8] K. Zweibel, H. Ullal, and B. von Roedern, *Finally: Thin-film PV!*, PHOTON International pp. 48–54 (October 2004).

[9] K. Zweibel, H. Ullal, and B. von Roedern, *Thin films in detail*, PHOTON International pp. 46–52 (November 2004).

[10] K. Zweibel, *Thin Film Solar Cells: Fabrication, Characterization and Applications* (John Wiley & Sons, J. Poortmans and V. Archipov (Ed.), to be published), chap. The terawatt challenge for thin-film PV.

[11] United Nations Development Programme, United Nations Department of Economic and Social Affairs, and World Energy Council, Tech. Rep. (2000), URL http://www.undp.org/seed/eap/activities/wea/.

[12] M. I. Hoffert, K. Caldeira, G. Benford, D. R. Criswell, C. Green, H. Herzog, A. K. Jain, H. S. Kheshgi, K. S. Lackner, J. S. Lewis, et al., Science **298**, 981 (2002).

[13] N. S. Lewis, *Global Energy Perspective*, URL http://www.its.caltech.edu/~mmrc/nsl/energy.html.

Reproduced with permission of the copyright owner. Further reproduction prohibited without permission.

[14] D. Stipp, FORTUNE magazine **149** (2004), URL `http://nreldev.nrel.gov/ncpv/thin_film/docs/climate_collapse_fortune_feb_2004.doc`.

[15] S. M. Sze, *Physics of Semiconductor Devices* (John Wiley & Sons, 1981), 2nd ed.

[16] M. A. Green, *Solar Cells* (Prentice Hall, Englewood Cliff, NJ, 1982).

[17] A. L. Fahrenbruch and R. H. Bube, *Fundamentals of Solar Cells* (Academic Press, Inc., New York, 1983).

[18] A. Luque and S. Hegedus, eds., *Handbook of Photovoltaic Energy Conversion and Engineering* (John Wiley & Sons Ltd, Chichester, West Sussex, England, 2003).

[19] X. Wu, J. C. Keane, R. G. Dhere, C. DeHart, D. S. Albin, A. Duda, T. A. Gessert, S. Asher, D. H. Levi, and P. Sheldon, in *Proc. 17th European Photovoltaic Sol. Energy Conf.* (2001), pp. 995–1000.

[20] W. N. Shafarman and L. Stolt, *Handbook of Photovoltaic Science and Engineering* (Wiley Chichester, 2003), chap. Cu(In,Ga)Se_2 Solar Cells, pp. 567–616.

[21] L. J. Simpson, J. S. Britt, S. Wiedeman, M. E. Beck, B. S. Joshi, T. L. Vincent, J. P. Delplanque, R. J. Kee, N. B. Gomez, K. M. Williams, et al., in *Proc. NCPV and Solar Program Review Meeting* (2003), p. 604.

[22] G. Jensen, J. Schaefer, G. M. Hanket, E. Eser, and S. Wiedeman, in *Proc. NCPV and Solar Program Review Meeting* (2003), p. 877.

[23] R. Birkmire, E. Eser, S. Fields, and W. Shafarman, Prog. Photovoltaics **13**, 141 (2005).

[24] M. S. Keshner and R. Arya, Tech. Rep., National Renewable Energy Laboratory, http://www.nrel.gov/docs/fy05osti/36846.pdf (2004).

[25] K. Ramanathan, M. A. Contreras, C. L. Perkins, S. Asher, F. S. Hasoon, J. Keane, D. Young, M. Romero, W. Metzger, R. Noufi, et al., Prog. Photovoltaics **11**, 225 (2003).

[26] K. Ramanathan, G. Teeter, J. C. Keane, and R. Noufi, Thin Solid Films **480-481**, 499 (2005).

[27] M. A. Contreras, K. Ramanathan, J. AbuShama, F. Hasoon, D. L. Young, B. Egaas, and R. Noufi, Prog. Photovoltaics **13**, 209 (2005).

[28] U. Rau and H. W. Schock, Appl. Phys. A **69**, 131 (1999).

[29] S. B. Zhang, S.-H. Wei, A. Zunger, and H. Katayama-Yoshida, Phys. Rev. B **57**, 9642 (1998).

[30] D. Rudmann, A. F. da Cunha, M. Kaelin, F. Kurdesau, H. Zogg, and A. N. Tiwari, Appl. Phys. Lett. **84**, 1129 (2004).

[31] C. R. Corwine, A. O. Pudov, M. Gloeckler, S. H. Demtsu, and J. R. Sites, Sol. Energy Mat. Sol. Cells **82**, 481 (2004).

Reproduced with permission of the copyright owner. Further reproduction prohibited without permission.

[32] A. Pudov, Ph.D. thesis, Colorado State University (2005).

[33] A. Romeo, M. Terheggen, D. Abou-Ras, D. L. Bätzner, F.-J. Haug, M. Kälin, D. Rudmann, and A. N. Tiwari, Prog. Photovoltaics **12**, 93 (2004).

[34] K. L. Chopra, P. D. Paulson, and V. Dutta, Prog. Photovoltaics **12**, 69 (2004).

[35] J. R. Sites, H. Tavakolian, and R. A. Sasala, Solar Cells **29**, 39 (1990).

[36] M. Gloeckler and J. R. Sites, J. Appl. Phys. **95**, 4438 (2004).

[37] J. T. Heath, J. D. Cohen, and W. N. Shafarman, J. Appl. Phys. **95**, 1000 (2004).

[38] M. Burgelman, P. Nollet, and S. Degrave, Thin Solid Films **361-362**, 527 (2000).

[39] K. Emery, *Handbook of Photovoltaic Science and Engineering* (Wiley Chichester, A. Luque and S. Hegedus (Ed.), 2003), pp. 702–711 (Based on R. Bird, R. Hulstrom, and C. Riordan, Solar Cells 14, 193 [1985]).

[40] P. K. Johnson, Ph.D. thesis, Colorado State University (2003).

[41] S. S. Hegedus and W. N. Shafarman, Prog. Photovoltaics **12**, 155 (2004).

[42] J. R. Sites and P. H. Mauk, Solar Cells **27**, 411 (1989).

[43] *Personal correspondence with K. Ramanthan, M. Contreras, D. Albin, J. AbuShama, and S. Shaheen at the National Renewabel Energy Laboratory; J. Phillips; Gregory Parsons at NC State; available to others upon request.*

[44] M. Gloeckler and J. R. Sites, in *Proc. 19th European Photovoltaic Sol. Energy Conf.* (2004).

[45] W. Shockley and W. T. Read, Physical Review **87**, 835 (1952).

[46] R. N. Hall, Phys. Rev. **87**, 387 (1952).

[47] R. C. Neville, *Solar Energy Conversion: the solar cell* (Elsevier, New York, 1995).

[48] *ISE Integrated Systems Engineering Release 9.5 - Part 15: DESSIS*, ISE Integrated Systems Engineering AG, Zurich, Switzerland (2004).

[49] *A manual for AMPS-1D for Windows '95/NT*, Pennsylvania State University (1997).

[50] D. Schmid, M. Ruckh, and H. W. Schock, Sol. Energy Mat. Sol. Cells **41-42**, 281 (1996).

[51] T. Schulmeyer, R. Hunger, A. Klein, W. Jaegermann, and S. Niki, Appl. Phys. Lett. **84**, 3067 (2004).

[52] S.-H. Wei and A. Zunger, Appl. Phys. Lett. **63**, 2549 (1993).

[53] F. Säuberlich and A. Klein, Mat. Res. Soc. Symp. Proc. **763**, 471 (2003).

[54] S.-H. Wei and A. Zunger, Appl. Phys. Lett. **72**, 2011 (1998).

Reproduced with permission of the copyright owner. Further reproduction prohibited without permission.

[55] D. K. Schroder, *Semiconductor Material and Device Characterization* (John Wiley & Sons, Inc., New York, 1998).

[56] S. J. Fonash, *Solar Cell Device Physics* (Academic Press, New York, 1981).

[57] J. Lee, J. D. Cohen, and W. N. Shafarman, Thin Solid Films **480-481**, 336 (2005).

[58] *unpublished, contact: David Albin, National Renewable Energy Laboratory, Golden, CO.*

[59] P. D. Paulson, R. W. Birkmire, and W. N. Shafarman, J. Appl. Phys. **94**, 879 (2003).

[60] M. Gloeckler, Ph.D. thesis, Colorado State University (2002).

[61] D. W. Niles, D. Rioux, and H. Höchst, J. Appl. Phys. **4586-4590** (1993).

[62] S.-H. Wei, S. B. Zhang, and A. Zunger, J. Appl. Phys. **87**, 1304 (2000).

[63] J. Fritsche, T. Schulmeyer, D. Kraft, A. Thißen, A. Klein, and W. Jaegermann, Appl. Phys. Lett. **81**, 2297 (2002).

[64] G. Stollwerck and J. R. Sites, in *Proc. 13th European Photovoltaic Sol. Energy Conf.* (1995), pp. 2020–2022.

[65] A. Niemegeers and M. Burgelman, J. Appl. Phys. **81**, 2881 (1997).

[66] C. Neumann, A. Nöthe, and N. O. Lipari, Phys. Rev. B **37**, 922 (1988).

[67] L. S. Dang, G. Neu, and R. Romestain, Solid State Comm. **44**, 1187 (1982).

[68] O. Madelung, ed., *Semiconductors: Others Than Group IV Elements and III-V Compounds (Data in Science and Technology)* (Springer Verlag, 1992).

[69] M. Gloeckler, A. L. Fahrenbruch, and J. R. Sites, in *Proc. 3rd World Conf. Photovoltaic Energy Conversion* (2003), pp. 491–494.

[70] M. Burgelman, J. Verschraegen, S. Degrave, and P. Nollet, Prog. Photovoltaics **12**, 143 (2004).

[71] S. Degrave, M. Burgelman, and P. Nollet, in *Proc. 3rd World Conf. Photovoltaic Energy Conversion* (2003), pp. 2P–D3–50.

[72] S.-H. Wei, S. B. Zhang, and A. Zunger, Appl. Phys. Lett. **72**, 3199 (1998).

[73] O. Lundberg, Ph.D. thesis, Uppsala University (2003).

[74] M. A. Contreras, B. Egaas, K. Ramanathan, J. Hiltner, A. Swartzlander, F. Hasoon, and R. Noufi, Prog. Photovoltaics **7**, 311 (1999).

[75] M. Topič, F. Smole, and J. Furlan, J. Appl. Phys. **79**, 8537 (1996).

[76] A. Dhingra and A. Rothwarf, IEEE Trans. Elect. Devices **43**, 613 (1996).

Reproduced with permission of the copyright owner. Further reproduction prohibited without permission.

[77] J. L. Gray and Y. J. Lee, in *Proc. 1st World Conf. Photovoltaic Energy Conversion* (1994), pp. 123–126.

[78] J. Song, S. S. Li, C. H. Huang, O. D. Crisalle, and T. J. Anderson, Solid-State Electronics **48**, 73 (2004).

[79] T. Dullweber, G. Hanna, W. Shams-Kolahi, A. Schwartzlander, M. A. Contreras, R. Noufi, and H. W. Schock, Thin Solid Films **361-362**, 478 (2000).

[80] A. M. Gabor, J. R. Tuttle, M. H. Bode, A. Franz, A. L. Tennant, M. A. Contreras, R. Noufi, D. G. Jensen, and A. M. Hermann, Sol. Energy Mat. Sol. Cells **41-42**, 247 (1996).

[81] T. Dullweber, O. Lundberg, J. Malmström, M. Bodegård, L. Stolt, U. Rau, H. W. Schock, and J. H. Werner, Thin Solid Films **387**, 11 (2001).

[82] T. Dullweber, Ph.D. thesis, Universität Stuttgart (2002).

[83] M. A. Contreras, J. Tuttle, A. Gabor, A. Tennant, K. Ramanathan, S. Asher, A. Franz, J. Keane, L. Wang, and R. Noufi, Sol. Energy Mat. Sol. Cells **41-42**, 231 (1996).

[84] M. Bodegård, O. Lundberg, J. Malmström, and L. Stolt, in *Proc. 28th IEEE Photovoltaic Specialist Conf.* (2000), pp. 450–453.

[85] O. Lundberg, M. Edoff, and L. Stolt, Thin Solid Films **480-481**, 520 (2005).

[86] T. Dullweber, U. Rau, M. A. Contreras, R. Noufi, and H.-W. Schock, IEEE Trans. Elect. Devices **47**, 2249 (2000).

[87] O. Lundberg, M. Bodegård, J. Malmström, and L. Stolt, Prog. Photovoltaics **11**, 77 (2003).

[88] X. Liu and J. R. Sites, in *Proc. AIP Conf.* (1996), pp. 444–452.

[89] R. Scheer, Trends in Vac. Science & Technology **2**, 77 (1997).

[90] G. B. Turner, R. J. Schwartz, and J. L. Gray, in *Proc. 20th IEEE Photovoltaic Specialist Conf.* (1988), p. 1457.

[91] T. Minemoto, T. Matsui, H. Takakura, Y. Hamakawa, T. Negami, Y. Hashimoto, T. Uenoyama, and M. Kitagawa, Sol. Energy Mat. Sol. Cells **67**, 83 (2001).

[92] W. N. Shafarman, R. Klenk, and B. E. McCandless, J. Appl. Phys. **79**, 7324 (1996).

[93] H. W. Schock, U. Rau, T. Dullweber, G. Hanna, M. Balboul, T. Margorian-Friedlmeier, A. Jasenek, I. Kötschau, H. Kerber, and H. Wiesner, in *Proc. 16th European Photovoltaic Sol. Energy Conf.* (2000), pp. 304–308.

[94] J. Malmström, J. Wennerberg, M. Bodegård, and L. Stolt, in *Proc. 17th European Photovoltaic Sol. Energy Conf.* (2001), pp. 1265–1268.

Reproduced with permission of the copyright owner. Further reproduction prohibited without permission.

[95] T. Minemoto, Y. Hashimoto, W. Shams-Kolahi, T. Satoh, T. Negami, H. Takakura, and Y. Hamakawa, Sol. Energy Mat. Sol. Cells **75**, 121 (2003).

[96] M. Turcu and U. Rau, J. Phys. Chem. Solids **64**, 1591 (2003).

[97] A. O. Pudov, F. S. Hasoon, H. Al-Thani, and J. R. Sites (unpublished).

[98] M. A. Contreras, T. Nakada, M. Hongo, A. O. Pudov, and J. R. Sites, in *Proc. 3rd World Conf. Photovoltaic Energy Conversion* (2003), pp. 570–573.

[99] J. A. M. AbuShama, S. Johnston, T. Moriarty, G. Teeter, K. Ramanathan, and R. Noufi, Prog. Photovoltaics **12**, 39 (2004).

[100] D. L. Young, J. Keane, A. Duda, J. A. M. AbuShama, C. L. Perkins, M. Romero, and R. Noufi, Prog. Photovoltaics **11**, 535 (2003).

[101] A. Niemegeers, M. Burgelman, and A. DeVos, Appl. Phys. Lett. **67**, 843 (1995).

[102] D. Cahen and R. Noufi, Appl. Phys. Lett. **54**, 558 (1989).

[103] Y. J. Zhao, C. Persson, S. Lany, and A. Zunger, Appl. Phys. Lett. **85**, 5860 (2004).

[104] A. O. Pudov, A. Kanevce, H. A. Al-Thani, J. R. Sites, and F. S. Hasoon, J. Appl. Phys. **97**, 064901 (2005).

[105] S. S. Hegedus, Prog. Photovoltaics **5**, 151 (1997).

[106] J. Hou and S. J. Fonash, in *Proc. 25th IEEE Photovoltaic Specialist Conf.* (1996), pp. 961–964.

[107] I. L. Eisgruber, J. E. Granata, J. R. Sites, J. Hou, and J. Kessler, Sol. Energy Mat. Sol. Cells **53**, 367 (1998).

[108] M. Topič, F. Smole, J. Furlan, and M. A. Contreras, in *Proc. 14th European Photovoltaic Sol. Energy Conf.* (1997), p. 2139.

[109] A. O. Pudov, J. R. Sites, M. A. Contreras, T. Nakada, and H.-W. Schock, Thin Solid Films, in press (2005).

[110] A. Kanevce, M. Gloeckler, A. Pudov, and J. R. Sites, Mat. Res. Soc. Symp. Proc. **865** (2005).

[111] M. Igalson, A. Kubiaczyk, and P. Zabierowski, Mat. Res. Soc. Symp. Proc. **688**, H9.2.1 (2001).

[112] H. G. Grimmeiss and N. Kullendorff, J. Appl. Phys. **52**, 3405 (1981).

[113] J. W. Orton, B. J. Goldsmith, J. A. Chapman, and M. J. Powell, J. Appl. Phys. **53**, 1602 (1982).

[114] M. Gloeckler, C. R. Jenkins, and J. R. Sites, Mat. Res. Soc. Symp. Proc. **763**, 231 (2003).

Reproduced with permission of the copyright owner. Further reproduction prohibited without permission.

[115] G. Agostinelli, E. D. Dunlop, D. L. Bätzner, A. N. Tiwari, P. Nollet, M. Burgelman, and M. Köntges, in *Proc. 3rd World Conf. Photovoltaic Energy Conversion* (2003), pp. 2O–C10–03.

[116] D. L. Bätzner, G. Agostinelli, A. Romeo, H. Zogg, and A. N. Tiwari, Mat. Res. Soc. Symp. Proc. **668**, H5.17.1 (2001).

[117] S. Hegedus, D. Ryan, K. Dobson, B. McCandless, and D. Desai, Mat. Res. Soc. Symp. Proc. **763**, 447 (2003).

[118] M. Köntges, R. Reineke-Koch, P. Nollet, J. Beier, R. Schäffler, and J. Parisi, Thin Solid Films **403-404**, 280 (2002).

[119] T. J. Coutts, J. S. Ward, D. L. Young, K. A. Emery, T. A. Gessert, and R. Noufi, Prog. Photovoltaics **11**, 359 (2003).

[120] C. R. M. Grovenor, J. Phys. C: Solid State Phys. **18**, 4079 (1985).

[121] M. A. Green, K. Emery, D. L. King, S. Igari, and W. Warta, Prog. Photovoltaics **11**, 347 (2003).

[122] W. K. Metzger and M. Gloeckler, to be published (2005).

[123] J. Y. W. Seto, J. Appl. Phys. **46**, 5247 (1975).

[124] H. C. Card and E. S. Yang, IEEE Trans. Elect. Devices **24**, 397 (1977).

[125] A. K. Ghosh, C. Fishman, and T. Feng, J. Appl. Phys. **51**, 446 (1979).

[126] N. C. Halder and T. R. Williams, Solar Cells **8**, 201 (1983).

[127] S. Banerjee and H. Saha, Solar Cells **28**, 77 (1990).

[128] J. Dugas and J. Oualid, Solar Cells **20**, 167 (1987).

[129] S. Elnahwy and N. Adeeb, J. Appl. Phys. **64**, 5214 (1988).

[130] N. C. Halder and T. R. Williams, Solar Cells **85**, 225 (1983).

[131] M. A. Green, Solid-State Electronics **21**, 1139 (1978).

[132] M. A. Green, J. Appl. Phys. **80**, 1515 (1996).

[133] S. A. Edmiston, G. Heiser, A. B. Sproul, and M. A. Green, J. Appl. Phys. **80**, 6783 (1996).

[134] K. Kurobe, Y. Ishikawa, Y. Yamamoto, T. Fuyuki, and H. Matsunami, Sol. Energy Mat. Sol. Cells **65**, 201 (2001).

[135] T. Matsui, T. Yamazaki, A. Nagatani, K. Kino, H. Takatura, and Y. Hamakawa, Sol. Energy Mat. Sol. Cells **65**, 87 (2001).

[136] T. Fujisaki, A. Yamada, and M. Konagai, Sol. Energy Mat. Sol. Cells **74**, 331 (2002).

Reproduced with permission of the copyright owner. Further reproduction prohibited without permission.

[137] H. Takakura and Y. Hamakawa, Sol. Energy Mat. Sol. Cells **74**, 479 (2002).

[138] A. Zerga, E. Christoffel, and A. Slaoui, in *Proc. 3rd World Conf. Photovoltaic Energy Conversion* (2003), pp. 1053–1056.

[139] Y. Ishikawa, Y. Yamamoto, T. Hatayama, Y. Uraoka, and T. Fuyuki, Jpn. J. Appl. Phys **40**, 6783 (2001).

[140] K. Taretto, U. Rau, and J. H. Werner, 480-481 pp. 447–451 (2005).

[141] C.-S. Jiang, R. Noufi, J. A. AbuShama, K. Ramanathan, H. R. Moutinho, J. Pankow, and M. M. Al-Jassim, Appl. Phys. Lett. **84**, 3477 (2004).

[142] C.-S. Jiang, R. Noufi, K. Ramanathan, H. R. Moutinho, and M. M. Al-Jassim, J. Appl. Phys. **97**, 053701 (2005).

[143] C.-S. Jiang, R. Noufi, K. Ramanathan, J. A. AbuShama, H. R. Moutinho, and M. M. Al-Jassim, Appl. Phys. Lett. **85**, 2625 (2004).

[144] S. Schuler, S. Nishiwaki, J. Beckman, N. Rega, S. Brehme, S. Siebentritt, and M. C. Lux-Steiner, in *Proc. 29th IEEE Photovoltaic Specialist Conf.* (2002), pp. 504–507.

[145] S. Sadewasser, T. Glatzel, S. Schuler, S. Nishiwaki, R. Kaigawa, and M. C. Lux-Steiner, Thin Solid Films **431-432**, 257 (2003).

[146] D. Fuertes Marrón, S. Sadewasser, A. Meeder, T. Glatzel, and M. C. Lux-Steiner, Phys. Rev. B **71**, 033306 (2005).

[147] D. Fuertes Marrón, T. Glatzel, A. Meeder, T. Schedel-Niedrig, S. Sadewasser, and M. C. Lux-Steiner, Appl. Phys. Lett. **85**, 3755 (2004).

[148] C. Persson and A. Zunger, Phys. Rev. Let. **91**, 266401 (2003).

[149] M. Hetzer, Y. M. Strzhemechny, M. Gao, L. J. Brillson, M. A. Contreras, C. Persson, and A. Zunger, Appl. Phys. Lett. **86**, 162105 (2005).

[150] V. G. Karpov, A. D. Compaan, and D. Shvydka, in *Proc. 29th IEEE Photovoltaic Specialist Conf.* (UT, 2002), pp. 708–711.

[151] S. D. Feldman, L. Mansfield, T. R. Ohno, V. Kaydanov, J. D. Beach, and T. Nagle, in *Proc. 31st IEEE Photovoltaic Specialist Conf.* (2005).

[152] J. F. Hiltner and J. R. Sites, in *Proc. 16th European Photovoltaic Sol. Energy Conf.* (2000), p. 650.

[153] J. R. Sites, Sol. Energy Mat. Sol. Cells **75**, 243 (2003).

[154] W. Mönch, *Semiconductor Surfaces and Interfaces* (Springer Berlin, 2001).

[155] D. Schmid, M. Ruckh, F. Grunwald, and H. W. Schock, J. Appl. Phys. pp. 2902–2909 (1993).

Reproduced with permission of the copyright owner. Further reproduction prohibited without permission.